ABSTRACT

Title of Dissertation:       STUDY OF LONGITUDINAL DYNAMICS IN
SPACE-CHARGE DOMINATED BEAMS

Kai Tian, Doctor of Philosophy, 2008

Dissertation Directed By:     Professor Patrick G. O'Shea
Professor Rami A. Kishek
Department of Electrical and Computer Engineering

Modern accelerator applications, such as heavy ion fusion drivers, pulsed neutron sources, electron injectors for high-energy linear colliders, and X-ray Free Electron Lasers, demand beams with high intensity, low emittance and small energy spread. At low (non-relativistic) energies, the "electrostatic", collective interactions from space-charge forces existing in such intense beams play the dominant role; we characterize these beams as space-charge dominated beams. This dissertation presents numerous new findings on the longitudinal dynamics of a space-charge dominated beam, particularly on the propagation of density perturbations. In order to fully understand the complex physics of longitudinal space-charge waves, we combine the results of theory, computer simulation, and experiment.

In the Long Solenoid Experimental system (LSE), with numerous diagnostic tools and techniques, we have, for the first time, experimentally measured the detailed energy profiles of longitudinal space-charge waves at different locations, both near

the beam source and at the end of the transport system. Along with the current profiles, we have a complete set of experimental data for the propagation of space-charge waves. We compare these measured results to a 1-D theory and find better agreement for beams with perturbations in the linear regime, where the perturbation strength is less than 10%, than those with nonlinear perturbations. Using fast imaging techniques that we newly developed, we have, for the first time, obtained the progressive time-resolved images of longitudinal slices of a space-charge dominated beam. These images not only provide us time-resolved transverse density distribution of the beam, but also enable us to take time-resolved transverse phase space measurement using computerized tomography. By combining this information with the longitudinal energy measurement, we have, for the first time, experimentally constructed the full 6-D phase space.

Part of the results from the 6-D phase space measurement has been used as initial conditions in computer simulations in order to explore the cause of discrepancies we have observed earlier between the experimental and theoretical models. After extensive simulation studies, we find that the beam loss inside the perturbation due to mismatch or misalignment is an important factor that needs to be included in the models for better reliability.

STUDY OF LONGITUDINAL DYNAMICS IN SPACE-CHARGE DOMINATED
BEAMS


By


Kai Tian



Dissertation submitted to the Faculty of the Graduate School of the
University of Maryland, College Park, in partial fulfillment
of the requirements for the degree of
Doctor of Philosophy
2008




Advisory Committee:
        Professor Patrick G. O'Shea, Chair / Advisor
        Professor Rami A. Kishek/ Co-Advisor
        Professor Emeritus Martin Reiser
        Professor Victor L. Granatstein
        Professor Richard F. Ellis

# Dedication

To my wife Qiushi Lu, and my parents, Benfu Tian and Ruijie Sun.

# Acknowledgements

I am grateful to many people who provided assistance to me during my time at University of Maryland. First and foremost, I would like to thank my advisor, Professor Patrick G. O'Shea, who guided me to achieve the successful completion of my thesis. I have benefited a lot from his professional advice as well as his enthusiasm and encouragement in my research. My co-advisor, Dr. Rami A. Kishek, has been providing direct assistance and useful discussion in my research. I am also indebted for his efforts in revising the first version of this dissertation. The thesis would not have been possible without the constructive criticism of my work from Professor Martin Reiser, who is the senior authority in our field.

Following, I would like to thank Dr. Irving Haber for his support on computer simulations and helpful advice in experiment. Dr. Haber has been keeping reminding me to work hard toward my Ph.D. degree, which spurred me on to quickly make progress in my research. I am indebted to Dr. Yupeng Cui and Dr. Yun Zou, my former colleagues, for their help in the early experimental work during my first year at Maryland. They provided me a very good start point of the research. I wish to thank Dr. David Sutter for his help in rebuilding the control electronics of the electron gun and his insightful advice in my future career. I am really influenced much by his enthusiasm in science. I am indebted to Dr. John Rodgers for his help in cleaning the noise of the beam signal. Without his expertise, many experimental data in this dissertation would not be possible. Dr. Donald Feldman and Dr. Ralph Fiorito helped me a lot in the fast imaging experiment. In particular, I am grateful to Dr. Mark Walter for his mechanical support, Bryan Quinn for his support on electrical

problems, Douglas Cohen for his professional work in machine shop, and Dr. Santiago Bernal for his valuable advice. In addition, I would like to thank my fellow graduate students Brian Beaudoin, Gang Bai, Chao Wu, Charles Jayakar Tobin, Christos Papadopoulos, Diktys Stratakis, Nathan Moody, and Michael Holloway for offering me help when I need it. I am indebted to Eric Montgomery for his advice in revising this thesis.

I would like to thank all the scientists who provided me insightful advice in both my research and career path during my attendance to conferences and visit to their laboratories. I also wish to thank Professor Granatstein and Professor Ellis for serving on my thesis exam committee.

I am also grateful to my friends who help me generously and make my life in USA much easier. Since they are numerous, I can not list all of their names here. But I would particularly thank Yupeng Cui, Yijie Huo, Hui Li, and Yingyu Miao.

Last but not least, I would like to thank my parents for their altruistic love and continuous support. I would also like to thank my wife, who has given a love I never expected and makes me feel that my life is full and complete.

# Table of Contents

# List of Tables

# List of Figures

# Chapter 1  Introduction

Many modern applications of intense particle beams require the transport of high quality beams over substantial distances. For most of these machines, near the source, the internal repulsion, or space-charge forces, is important in determining the beam characteristics. In a space-charge dominated beam, collective nonlinear space-charge forces can reduce the beam quality.

This collective behavior can be quite complex. One example is longitudinal space-charge waves that can be generated by a density perturbation or energy perturbation. Such perturbations can lead to instabilities that can disrupt the beam under certain circumstances. As an example, Coherent Synchrotron Radiation (CSR) can be generated from these perturbations and causes the growth of energy spread and emittance [1]. Today, as a result of growing interest in intense beam applications such as accelerator-driven high-energy-density physics (HEDP) [2], pulsed neutron sources [3], and x-ray free electron lasers [4], a detailed knowledge and understanding of space-charge waves has become increasingly important for the successful operation of such machines. In this dissertation, we present new findings on both the evolution of space-charge waves and the correlation between the longitudinal and transverse dynamics.

In Sec. 1.1 of this introductory chapter, we describe the general background and motivation of the research in longitudinal space-charge waves. A review of some recent work follows in Sec 1.2. Finally, we present the organization of this dissertation in Sec. 1.3.

## 1.1 Background and Motivation

A charged particle beam is a well confined group of particles moving along a straight or curved orbit, defined as the longitudinal direction, in which the energy associated with the longitudinal motion is much greater than that associated with the transverse motion. During the transport, beams are defocused by space-charge forces and by the emittance, which is a measure of the random thermal motion of particles inside the beam. Space-charge forces are collective effects due to the repulsive coulomb interaction between particles, and are therefore a function of the particle distribution and the boundary conditions. Transverse focusing elements such as solenoid or quadrupole lenses are generally used to compensate the defocusing effects from the emittance and space-charge forces. A beam is space-charge dominated when the space-charge forces exceed the outward forces from the emittance of the beam. In the terminology of plasmas physics, for a space-charge dominated beam, the Debye length $\lambda_D$ in the beam is significantly smaller than the beam radius. As a result, collective space-charge oscillations are not negligible.

There is a long history of research on the behavior of space-charge waves in the field of microwave generation, which can be traced back to the 1930s [5-9]. In these studies, the beam velocity is usually modulated by a longitudinal electric field in a gap. The waves in this case appear in pairs as fast and slow waves with almost equal amplitudes. The early theoretical analyses, carried out in frequency domain for simplicity, are more interested in high frequency perturbations for the goal of microwave generation. In contrast, in our beam the wavelength of the modulation is generally long compared to the beam pipe radius.

The theory developed for traveling-wave tubes was extended to longitudinal resistive instabilities of beams in particle accelerators in 1960s [10]. Since the early 1980s, due to emerging interest of heavy ion inertial fusion drivers, extensive theoretical and computational efforts have been conducted on the longitudinal instabilities of space-charge waves [11-15]. In 1997, simulation results published by Callahan etc. suggest that "the longitudinal instability must be taken into account in a driver design, but it is not the major factor it was once thought to be" [16].

With more research focused on high brightness light sources, the effects of longitudinal space-charge waves on beam quality have recently attracted much attention in the community of particle accelerators. For example, in a photo-injector, when a very high charge per bunch is desired, the nonlinear effects from the drive laser can introduce density modulations into the longitudinal current profile of the beam [17]. Since these density modulations are generated close to the source, where space-charge is important, energy modulations can result from the large space-charge potential energy in initial density perturbations. After the photo-injector, the beam is accelerated to higher energy and the space-charge force is no longer dominant. However, energy modulations created close to the source are frozen-in when the beam becomes relativistic. Further downstream, in the magnetic bends or bunchers, these energy modulations can excite Coherent Synchrotron Radiation (CSR), which can cause emittance growth [1], beam instability, and micro-bunching [18]. CSR tends to modulate the beam energy and increase the energy modulations leading to stronger CSR. Consequently, the beam quality can substantially degrade in this

process. Hence, in order to preserve high beam quality, it is very important to understand the longitudinal beam dynamics in the space-charge dominated beam.

In other applications, there is interest in modulated electron beams specifically for the purpose of generating coherent radiation. For instance, in order to generate terahertz radiation, the electron beam from the photocathode can be deliberately modulated in density by modulating the pulse shape of drive laser [19]. To achieve high quality light emission, the density modulations profiles need to be stable. However, experimental observations show that, when the space-charge effect is strong enough, transfer between density and energy modulations of space-charge waves partially wash out the modulation compared with the initial laser profile [20]. Thus, it is very important to understand and control the evolution of longitudinal space-charge waves.

## 1.2 Previous Studies of Space-charge Waves at University of Maryland

During the past two decades, the charged particle beams group at University of Maryland has initiated an experimental program to study longitudinal beam dynamics.

In early 1990s, J.G. Wang and D.X. Wang for the first time experimentally observed the evolution of space-charge waves by creating localized perturbations of beam current and velocity [21]. During the experiment, they also successfully generated a single localized space-charge wave, i.e., either a fast wave or a slow wave, instead of generating pairs of waves. The experimental results agree with analytical solutions derived from 1-D cold fluid equation under the assumption of linear perturbations. Later, they calculated the parametric dependence of the geometry

4

factor *g*, which measures the ratio between the longitudinal self electric field and the derivative of the ling charge density [22]. The results showed that the g factor has the range $2\ln(b/a) \le g \le [1/2 + 2\ln(b/a)]$ . For a space-charge dominated beam, $g = 2\ln(b/a)$, and for an emittance-dominated beam, it is $g = 1/2 + 2\ln(b/a)$, with a beam of radius *a* propagating through a transport channel with pipe radius *b*. A discussion can be found in connection with Eqs. (6.69a) and (6.69b) of Ref. [23]. The group then performed further experimental investigation on the reflection and transmission of space-charge waves at the ends of bunched beams [24, 25]. The speeds of the reflected and transmitted waves were measured. Theoretical analysis led to a critical condition for the existence of the reflection in the experiment. However, the detailed reflection process at an eroded beam shoulder and the propagation of transmitted waves on the beam end were not well understood because of the complexity of the highly nonlinear forces at beam edge.

In the late 1990's, a series of experiments were performed to study the interaction between a resistive wall and localized single space-charge waves. As before, a grid voltage perturbation generated a localized perturbation to produce space-charge waves [26]. Consistent with the theoretical prediction, the experimental results for linear perturbations clearly demonstrated the growth of single slow waves due to the resistive-wall instability and the decay of single fast waves [27, 28]. Subsequently, Zou extended the measurement of the growth/decay rates of the fast and slow waves to the nonlinear regime and the fast wave was found to increase with the increase of the perturbation [29]. In order to confirm this unexpected observation, the resistive wall was replaced by a conducting tube and the other conditions kept the

same. In this case, no growth or decay was observed for the fast wave. There is yet no theoretical explaining for these nonlinear phenomena.

In all the experiments mentioned above, a perturbation was generated by modulating the pulse voltage of the gridded electron gun. In recent experimental work using the larger propagation path available on the University of Maryland Electron Ring (UMER) [30, 31], an ultraviolet laser was used to impinge on the photocathode in generating a more controllable perturbation. The current profiles were measured in different chambers along the ring and the evolution of the current modulation was observed. The experimental results were compared with simulation results and showed good agreement.

## 1.3 Goals and Approach

Though much progress had been made on the experimental study of longitudinal space-charge waves in the past, several unsolved problems and challenging topics remain. First, due to the lack of high resolution diagnostic tools, most previous studies focused on the evolution of current profiles of space-charge waves. There was no comparison of the shape of energy profiles between theory and experiment. A second problem was the unknown physics of nonlinear perturbations. In the linear regime, experimental results of space-charge waves can be verified by the 1-D linear theory. But there was no clear explanation for the unexpected experimental result in the nonlinear regime, where the theoretical model breaks down. A third issue with the previous studies is their neglect of the transverse distribution and its effect on the longitudinal dynamics.

Our goals here are to resolve these issues by means of more detailed measurements and self-consistent simulations. Since the initial conditions of the beam are critical to accurate simulation of the beam behavior, in order to adequately study the longitudinal space-charge waves, we need initial 6-D phase space characterization of both perturbed and unperturbed beams. However, the typical width of the perturbation is only about 10 ns, therefore it is challenging to measure the time resolved information on such a small time scale. In this dissertation, we for the first time measure the time-resolved full 6-D phase space of beams with longitudinal perturbations. The 6-D phase space mapping has provided us many details in the evolution of longitudinal space-charge waves and longitudinal-transverse correlations. More important, it is helpful for constructing a self consistent model for studying the complex physics of longitudinal dynamics by combining with computer simulation codes.

## 1.4 Organization of this thesis

In chapter 2, we describe some basic concepts of space-charge dominated beams and introduce the 1-D cold fluid model for longitudinal space-charge waves.

In chapter 3, we present some high resolution measurements of the energy profiles of space-charge waves. First, we describe the Long Solenoid Experimental system (LSE), where the measurements are carried out. It is followed by the experimental results covering both linear and nonlinear perturbations, which are compared with theoretical calculations and computer simulations [32]. For the first time, both the shape of the current and energy profiles of space-charge waves have been accurately measured and compared side by side.

In chapter 4, two fast imaging techniques are described in UMER and the LSE system respectively [33]. In UMER, the optical transition radiation (OTR) is used to produce the image of a longitudinal slice within the perturbation. In spite of the promptness of the OTR light, its intensity is too low for practical application to our beams. Nevertheless we were still able to observe the correlation between the transverse distribution and the longitudinal perturbation. As an alternative of the OTR, a fast phosphor screen, with 3 ns decay time, was tested and verified as a good diagnostic tool for our beam. Progressive time resolved images have been taken for a parabolic shaped beam as well as rectangular pulsed beams with and without perturbations. These 3 ns time resolved images are adequate to provide transverse information along the beam, especially inside the perturbations. In addition, the longitudinal energy profiles of these beams have also been measured.

In chapter 5, we describe WARP [34] simulations of the experimental results shown in chapter 4. By carrying out the simulation in lab frame with detailed initial condition of the beam such as beam current, velocity, and transverse size, the simulation results have been demonstrated to be close enough to the experimental results for the parabolic beam and 25mA perturbed rectangular beam. However, the discrepancy between the experimental and simulation results for the 40 mA perturbed mean indicates the complex behavior of nonlinear perturbations.

Finally, chapter 6 summarizes the new results of this study and explores some interesting topics which could be continued for future research.

# Chapter 2  Theoretical Background of Space-Charge Waves

To correctly understand and model the longitudinal dynamics of space-charge waves, one should carry out 3-D analysis with consideration of effects from transverse dynamics. Nevertheless, a 1-D cold fluid model is sufficiently accurate for beams satisfying the long wavelength limit, where the wavelength of the perturbation is much larger than the beam transverse radius. The model provides us a big picture of the nature of longitudinal waves and helps us understand the experimental results discussed in later chapters. In this chapter, after a brief review of some concepts of transverse beam physics in Sec. 2.1, we discuss the 1-D cold fluid model with application to space-charge waves in Sec. 2.2. Finally, Sec. 2.3 concludes with some general remarks.

## 2.1 Space-charge dominated beams and envelope equations

For a charged particle beam in acceleration or transport channels, it is convenient to separate the transverse beam dynamics from the longitudinal dynamics when the bunch is relatively long compared with the transverse size. Since this thesis addresses the correlation between transverse and longitudinal dynamics, it is useful to review the theory of transverse dynamics before proceeding to discuss the longitudinal physics in beams.

Generally, during the beam transport, there are two factors causing the expansion of the beam. One is space-charge, originating from the self forces of similarly charged particles inside the beam; the other is emittance, coming from the thermal motion of particles. External focusing elements are normally applied to confine the

beam from expansion. In this section, we describe basic concepts of transverse beam physics including transverse emittance, the Kapchinsky-Vladimirsky (K-V) distribution, and the envelope equation (see, for instance, section 5.3.2 in [23]).

Particles in a beam will have a random velocity component in all directions. Emittance is used to measure this random spread. For a beam with low emittance, the particles inside the beam tend to keep moving parallel to each other, while for a high emittance beam, it will be difficult to focus the beam into a small spot. The definition of the unnormalized effective emittance in x direction was first proposed by Lapostolle (see Eq. (5.206) and related discussion in [23]). It can be expressed as:

$$\varepsilon_x = 4\sqrt{\langle x^2 \rangle \langle x'^2 \rangle - \langle xx' \rangle^2} \,, \tag{2.1}$$

where the bracket denotes moments of the bracket quantity over the particle distribution, e.g. $\langle x^2 \rangle = \iint x^2 f(x, y, x', y') dx dy dx' dy'$, and $x'$ is the differentiation of $x$ with respect to the direction of travel. Similarly, one can also derive the definition for y and z emittances.

The K-V distribution, which is described in p. 341 of reference [23], assumes a perfectly uniform beam density all the time. It provides a simple model for theoretically analyzing beam behavior affected by all factors mentioned above. In this model, the space-charge force is linear and the beam phase space area remains constant. In reality, for the forces to be linear in the transverse direction, the condition for paraxial motion must be satisfied and the changes in the beam size must occur slowly so that the longitudinal forces are negligible. Under this condition, the beam envelope in an axisymmetric focusing transport channel is described by the equation

$$a'' + \kappa_0 a - \frac{K}{a} - \frac{\varepsilon^2}{a^3} = 0 \,, \tag{2.2}$$

where $a$ is the two times rms beam radius, $a''$ is the second differentiation respect to the axial distance, $\kappa_0$ is the external focusing strength, $\varepsilon$ is the transverse emittance, and $K$ is the generalized beam perveance defined by

$$K = \frac{I}{I_0} \frac{2}{(\beta\gamma)^3},$$ (2.3)

where $\beta$ and $\gamma$ are the relativistic velocity and energy factors, respectively. $I$ is the beam current and $I_0$ is the characteristic current given by

$$I_0 = \frac{4\pi\varepsilon_0 mc^3}{q},$$ (2.4)

where $\varepsilon_0$ is the vacuum permittivity, m is the particle mass, c is the speed of light, and q is the particle charge. For electrons, $I_0 \approx 17000A$. As discussed in Sec. 5.3.4 of Ref. [23], for a beam with a arbitrary transverse distribution, the K-V envelope equation is still valid by replacing the beam radius $a$ with two times rms beam width, and replacing the emittance with four times rms emittance.

In the envelope equation, $\kappa_0 a$ represents the inward force from the external focusing channel, while $\frac{K}{a}$ and $\frac{\varepsilon^2}{a^3}$ represent the outward forces from space-charge and emittance, respectively. If the condition $\frac{K}{a} > \frac{\varepsilon^2}{a^3}$ is satisfied, the beam is transversely space-charge dominated. By contrast, if the condition $\frac{K}{a} < \frac{\varepsilon^2}{a^3}$ is satisfied, the beam is emittance dominated.

Similarly, the longitudinal envelope equation can be expressed as the following equation (see p.425 in reference [23] for details):

11

$$z_m'' + \kappa_{z0}z_m - \frac{K_L}{z_m^2} - \frac{\varepsilon_{zz'}^2}{z_m^3} = 0, \qquad (2.5)$$

where $2z_m$ is the bunch length, $\kappa_{z0}z_m$ is the longitudinal focusing term, $\varepsilon_{zz'}$ is the unnormalized effective longitudinal emittance, and $K_L$ is the longitudinal generalized perveance defined as:

$$K_L = \frac{3}{2}\frac{gNr_c}{\beta_0^2\gamma_0^5}, \qquad (2.6)$$

where $g$ is the geometry parameter, which will be discussed in detail later, N is the number of particles in the bunch, and $r_c = q^2/4\pi\varepsilon_0 mc^2$ is the classical particle radius.

When $\frac{K_L}{z_m^2} > \frac{\varepsilon_{zz'}^2}{z_m^3}$, the beam is space-charge dominated longitudinally, otherwise it is emittance dominated in longitudinal direction.

For a long bunch beam, since the longitudinal energy spread is low, the condition of $\frac{K_L}{z_m^2} > \frac{\varepsilon_{zz'}^2}{z_m^3}$ is always satisfied. Thus it is always naturally space-charge dominated in longitudinal direction for a beam under the assumption of long bunch. Therefore, one may conclude that a beam can be space-charge dominated in longitudinal direction, but emittance dominated in transverse direction. We deal with long bunch beams with high transverse space-charge effects, so without any clarification, all beams in this dissertation are space-charge dominated in both transverse and longitudinal directions.

## 2.2 Theoretical calculation of longitudinal space-charge waves

In this section, we introduce the theory on the generation and propagation of longitudinal waves analytically. First, in Sec. 2.2.1, a one-dimension model for single particle, where the beam is assumed to be large enough transversely to neglect any boundary conditions, is used to derive the dispersion function of space-charge waves (see p.499 in reference [23] for details). In practical, this model is applicable to the perturbations with very high frequency or small characteristic length compared with the beam transverse size. The perturbation of our interest is under the long wavelength limit, where the boundary conditions can not be ignored. Therefore, in Sec. 2.2.2, we apply the 1-D cold fluid model to derive the evolution of the space-charge waves of an infinitely long cylindrical beam inside a conducting pipe (see p.502 in reference [23] for details).

### 2.2.1 Single particle beam dynamics with a sinusoidal density modulation

In this section, we assume that the beam is cold and has an infinitely large transverse size, and travel at a non-relativistic speed $v_0$. Since the beam can be treated as a non-neutral plasma, a local charge perturbation can generate plasma oscillation in the beam. These plasma oscillations will lead to plasma waves propagating along the beam. In following, we will derive the dispersion function, phase velocity, and group velocity of these plasma waves.

Now let's assume that at $t = t_0$ a pure sinusoidal velocity modulation is generated in the longitudinal direction with an amplitude $v_1$, and a frequency $\omega$. This can be achieved if the beam passes through a small acceleration gap in an rf cavity with the

13

resonant frequency ω. From basic theory in plasma physics, local charge perturbations in plasma can generate plasma oscillations with plasma frequency:

$$\omega_p = \left[ \frac{q^2 n_0}{\varepsilon_0 m \gamma_0^3} \right]^{1/2},$$ (2.7).

where q is the charge of the particle, $n_0$ is the charge density, $\varepsilon_0$ is the permittivity of the free space; $\gamma_0$ is the Lorentz factor; m is the rest mass of the particle. Therefore, if s(t) represents the particle displacement from the equilibrium position in the beam frame as a function of time t, the harmonic oscillation equation of s(t) is:

$$\frac{d^2 s}{dt^2} + \omega_p s = 0.$$ (2.8)

The initial conditions can be defined as:

$$\begin{cases} s(t_0) = 0 \\ \frac{ds}{dt}\Big|_{t=t_0} = v_1 \cos \omega t_0 \end{cases}$$ (2.9)

By solving Equations (2.8) and (2.9), one can obtain the solution of the harmonic oscillation equation:

$$s(t, t_0) = \frac{v_1}{2i\omega_p} e^{i(\omega - \omega_p)t_0} e^{i\omega_p t} - \frac{v_1}{2i\omega_p} e^{i(\omega + \omega_p)t_0} e^{-i\omega_p t}$$ (2.10)

If we use z to represent the traveling distance of the beam in lab frame, then we have the relationship of $z = v_0(t - t_0)$. Hence $t_0$ can be replaced by $(t - z/v_0)$ in Equation (2.10). The solution then can be rewritten as:

$$s(t, t_0) = \frac{v_1}{2i\omega_p} e^{i(\omega t - k_f z)} - \frac{v_1}{2i\omega_p} e^{i(\omega t + k_s z)} .$$ (2.11)

This solution represents two space-charge waves, one with wave number $k_f$ and the other with wave number $k_s$. The two wave numbers are given by:

14

$$k_f = \frac{\omega - \omega_p}{v_0},$$
$$k_s = \frac{\omega + \omega_p}{v_0}. \qquad (2.12)$$

The dispersion relation can be derived by rewriting Equation (2.12):

$$(\omega - kv_0)^2 = \omega_p^2. \qquad (2.13)$$

Thus, the phase velocity and group velocity in the lab frame can be shown as:

$$v_f = \frac{\omega}{k_f} = \frac{v_0}{1 - (\omega_p / \omega)},$$
$$v_s = \frac{\omega}{k_s} = \frac{v_0}{1 + (\omega_p / \omega)}, \qquad (2.14)$$
$$v_g = \frac{\partial \omega}{\partial k} = v_0. \qquad (2.15)$$

The wave phase velocity $v_f$ is greater than the beam velocity, and is called the fast wave. The wave phase velocity $v_s$ is smaller than the beam velocity, and called the slow wave. However, equation (2.15) shows that either wave's energy will travel at the velocity of the beam. The same result can be derived if an initial density perturbation is given with the analysis above.

## 2.2.2 Analysis of space-charge waves using the one-dimensional cold fluid model

In the experiments related to this dissertation, a typical length of the longitudinal perturbation is about 10 ns, which is more than 40 cm long for a 5 keV electron beam. Therefore, the length of the perturbation is much longer than the size of the beam, which is of the order of 1 cm. As a result, the simple model in the previous section is not adequate in this case. We need analyze the longitudinal space-charge waves with a self consistent model considering the variation of longitudinal electric field $E_z$. In this section, we introduce a more complex model to derive a self-consistent result.

In this model, the beam is considered as an infinitely long cylinder of line charge density of $\Lambda$ and radius $a$ inside a conducting drift tube of radius $b$. We assume that the perturbation is much smaller in density and velocity than the unperturbed quantities. Subscripts 0 and 1 represent the unperturbed and perturbed physical quantities, respectively. By assuming a perturbation of the form of $e^{i\omega t - kz}$, the line charge density $\Lambda$, beam velocity $v$, and current $I$ can be expressed as

$$\begin{cases} \Lambda(z,t) = \Lambda_0 + \Lambda_1 e^{i(\omega t - kz)} \\ v(z,t) = v_0 + v_1 e^{i(\omega t - kz)} \\ I(z,t) = I_0 + I_1 e^{i(\omega t - kz)} \end{cases}, \tag{2.16}$$

where

$$I = \Lambda v. \tag{2.17}$$

The continuity equation can be expressed as:

$$\frac{\partial I}{\partial z} + \frac{\partial \Lambda}{\partial t} = 0. \tag{2.18}$$

Under the assumption of small perturbations, all terms higher than the first order can be neglected. Thus, from Equation (2.16) and (2.17), we can derive

$$I_0 = \Lambda_0 v_0, \tag{2.19}$$

$$I_1 = \Lambda_0 v_1 + v_0 \Lambda_1. \tag{2.20}$$

From Equation (2.16) and (2.18), one can obtain

$$\Lambda_1 = \frac{kI_1}{\omega}. \tag{2.21}$$

The longitudinal momentum equation can be expressed as

$$\gamma_0^3 m \frac{dv}{dt} = qE_z, \tag{2.22}$$

16

where $\gamma_0^3 m$ is the longitudinal mass and remains essentially constant under the assumption of small perturbations. The longitudinal self electric field $E_z$ due to space-charge can be expressed as

$$E_z = E_s e^{[i(\omega t - kz)]}.$$ (2.23)

Substituting Equations (2.16) and (2.23) into (2.22), then one can derive

$$v_1 = -i \frac{qE_s}{\gamma_0^3 m(\omega - kv_0)}$$ (2.24)

By substituting (2.21) into (2.20), $v_1$ can be represented by $I_1$. Hence we can rewrite Equation (2.24) as

$$E_s = i \frac{\gamma_0^3 m}{q \Lambda_0} \frac{(\omega - v_0 k)^2}{\omega} I_1.$$ (2.25)

On the other hand, $E_z$ can also be derived by solving the Maxwell equations (see chapter 6.3 in reference [23] or Appendix A in reference [35] for details)

$$E_z = -\frac{g}{4\pi\varepsilon_0 \gamma_0^2} \frac{\partial \Lambda}{\partial z},$$ (2.26)

where g is a geometry factor that defines the proportionality between the longitudinal self electric field and the derivative of the line charge density. For space-charge dominated beams, the g-factor can be expressed as $g = 2\ln(b/\bar{a})$, where $\bar{a}$ is the average beam size. If we substitute Equations (2.16), (2.21), and (2.23) into (2.26), we can obtain the relationship of

$$E_s = i \frac{g}{4\pi\varepsilon_0} \left( \frac{k^2}{\omega} - \frac{\omega}{c^2} \right) I_1.$$ (2.27)

The right hand sides of the Equations (2.25) and (2.27) will be equal. As a result, the dispersion equation is:

$$(\omega - kv_0)^2 - \gamma_0^2 c_s^2 k^2 (1 - \frac{\omega^2}{k^2 c^2}) = 0, \qquad (2.28)$$

where the "sound speed" of the space-charge wave, $c_s$, is defined as

$$c_s = \sqrt{\frac{qg\Lambda_0}{4\pi\varepsilon_0 \gamma_0^5 m}} \quad . \qquad (2.29)$$

Under the linear perturbation assumption, the difference between the phase velocities of the two space-charge waves and the beam velocity is very small. Hence, we can make the approximation of $\omega = kv_0$, and $\gamma_0^2 (1 - \frac{\omega^2}{k^2 c^2}) \approx \gamma_0^2 (1 - \frac{v_0^2}{c^2}) = 1$, therefore, equation (2.28) can be simplified as:

$$\omega = k(v_0 \pm c_s). \qquad (2.30)$$

Thus the phase velocities of the fast wave and slow wave can be obtained

$$\begin{aligned} v_f &= v_0 + c_s \\ v_s &= v_0 - c_s \end{aligned} \quad . \qquad (2.31)$$

Equation (2.31) shows that an observer moving with the beam velocity can see the two space-charge waves moving in opposite directions at the same speed, i.e., $c_s$ is the propagation speed of space-charge waves in beam frame. Since it does not depend on the frequency, the space-charge wave is non-dispersive.

In order to derive the analytical solution for the propagation of space-charge waves, the continuity equation and the momentum transfer equation can be linearized as

$$\begin{cases} \dfrac{\partial \Lambda_1}{\partial t} + v_0 \dfrac{\partial v_1}{\partial z} + \Lambda_0 \dfrac{\partial v_1}{\partial z} = 0 \\ \dfrac{\partial v_1}{\partial t} + v_0 \dfrac{\partial v_1}{\partial z} \approx \dfrac{e}{m\gamma^3} E_z = \dfrac{-eg}{4\pi\varepsilon_0 m\gamma^5} \dfrac{\partial \Lambda_1}{\partial z} \end{cases} . \tag{2.32}$$

Furthermore, the initial conditions and boundary conditions are: (a) There is no perturbation anywhere along the z-axis when t < 0. (b) At z=0 for t>0+ a localized velocity perturbation and current perturbation are introduced in the form:

$$\begin{aligned} v_1(0,t) &= \delta v_0 f(t) \\ I_1(0,t) &= \eta I_0 f(t) \end{aligned}, \tag{2.33}$$

where $\delta$ is a small, positive quantity to specify the strength of the velocity perturbation; $\eta$ is a small quantity to specify the strength of the initial current perturbation; $f(t)$ is any smooth function with an amplitude of unity which represent the shape of the perturbation and is supposed to vanish when t is equal or smaller than zero. Thus, by substituting (2.33) into (2.20), the line charge density perturbation can be expressed as

$$\Lambda_1(0,t) = (\eta - \delta)\Lambda_0 f(t). \tag{2.34}$$

By applying the double Laplace transformations for both z and t, the equation (2.32) can be converted to algebraic equations for $v_1$, $\Lambda_1$ and $I_1$ in the k-s domain. Then the algebraic equations can be solved. By applying inverse Laplace transformations, the perturbed beam density, velocity and current in the real time-space domain can be obtained as [21]:

$$\Lambda_1(z,t) = -\dfrac{\Lambda_0}{2}[\delta\dfrac{v_0}{c_s} - (\eta - \delta)]f(t - \dfrac{z}{v_0 - c_s}) + \dfrac{\Lambda_0}{2}[\delta\dfrac{v_0}{c_s} + (\eta - \delta)]f(t - \dfrac{z}{v_0 + c_s}),$$

$$\tag{2.35 a}$$

$$v_1(z,t) = \frac{v_0}{2}[\delta - (\eta - \delta)\frac{c_s}{v_0}]f(t - \frac{z}{v_0 - c_s}) + \frac{v_0}{2}[\delta + (\eta - \delta)\frac{c_s}{v_0}]f(t - \frac{z}{v_0 + c_s}),$$

<div align="right">(2.35 b)</div>

$$I_1(z,t) = -\frac{I_0}{2}[\delta\frac{v_0}{c_s} - \eta + (\eta - \delta)\frac{c_s}{v_0}]f(t - \frac{z}{v_0 - c_s}) + \frac{I_0}{2}[\delta\frac{v_0}{c_s} + \eta + (\eta - \delta)\frac{c_s}{v_0}]f(t - \frac{z}{v_0 + c_s}).$$

<div align="right">(2.35 c)</div>

All these expressions have two terms: the first term is the slow wave; the second term is the fast wave. Both the fast wave and the slow wave maintain the shape of the initial perturbation, while the amplitude and polarity are decided by the initial conditions. By using $\Lambda_{1(s,f)}$, $v_{1(s,f)}$, and $I_{1(s,f)}$ to represent the profiles of line charge density, velocity, and current, respectively, for the slow wave and fast wave components, from equation (2.35) one can derive

$$\Lambda_{1(s,f)}(z,t) = \frac{\eta\Lambda_0}{2}[1 - \frac{\delta}{\eta}\frac{(c_s \pm v_0)}{c_s}]f(t - \frac{z}{v_0 \mp c_s}), \qquad (2.36\ a)$$

$$v_{1(s,f)}(z,t) = \frac{\eta v_0}{2}[\mp\frac{c_s}{v_0} + \frac{\delta}{\eta}(1 \pm \frac{c_s}{v_0})]f(t - \frac{z}{v_0 \mp c_s}), \qquad (2.36\ b)$$

$$I_{1(s,f)}(z,t) = \frac{\eta I_0}{2}[(1 \mp \frac{c_s}{v_0}) - \frac{\delta}{\eta}(\pm\frac{v_0}{c_s} \mp \frac{c_s}{v_0})]f(t - \frac{z}{v_0 \mp c_s}). \qquad (2.36\ c)$$

where we take the sign on the top for the slow wave components and the sign on the bottom for the fast wave components. Since $c_s \ll v_0$, it yields the following approximation:

$$\frac{\delta}{\eta}\frac{(c_s \pm v_0)}{c_s} \approx \pm\frac{\delta v_0}{\eta c_s} = \pm\alpha, \qquad (2.37\ a)$$

$$\frac{\delta}{\eta}(1 \pm \frac{c_s}{v_0}) \approx \frac{\delta}{\eta} = \alpha\frac{c_s}{v_0}, \qquad (2.37\ b)$$

$$\frac{\delta}{\eta}(\pm\frac{v_0}{c_s}\mp\frac{c_s}{v_0}) \approx \pm\frac{\delta v_0}{\eta c_s} = \pm\alpha, \tag{2.37 c}$$

where we introduce a dimensionless $\alpha$-factor, defined as

$$\alpha = \frac{\delta v_0}{\eta c_s}. \tag{2.38}$$

By substituting (2.37) into (2.36), one can obtain

$$\Lambda_{1(s,f)}(z,t) = \frac{\eta(1\mp\alpha)\Lambda_0}{2}f(t-\frac{z}{v_0\mp c_s}), \tag{2.39 a}$$

$$v_{1(s,f)}(z,t) = \frac{\eta(\alpha\mp1)c_s}{2}f(t-\frac{z}{v_0\mp c_s}), \tag{2.39 b}$$

$$I_{1(s,f)}(z,t) = \frac{\eta I_0}{2}[(1\mp\frac{c_s}{v_0})\mp\alpha)]f(t-\frac{z}{v_0\mp c_s}). \tag{2.39 c}$$

When dealing with mostly current perturbations, $\alpha$ represents the contribution of the energy modulations, which can be neglected if $\alpha \ll 1$. However, if the ratio of $v_0$ and $c_s$ is big enough to result in a non-negligible $\alpha$, we need consider the correction by taking the $\alpha$-factor into account. For example, for an electron beam with a radius of 4.9mm, a mean beam energy of 5075 eV, and a unperturbed current of 94.5mA moving in a conducting pipe with a radius of 1.9 cm, if the perturbation current is 7.6 mA and the perturbed energy is 10 eV, we can calculate $\eta=0.08$, $\delta=0.00097$, and $\alpha = 0.167$. For this case, the value of the $\alpha$-factor is big enough to affect the amplitudes of the fast and slow waves.

When a pure current perturbation is the initial condition, i.e. $\delta = 0$ and $\alpha = 0$, Equation (2.35) can be simplified as

$$\Lambda_1(z,t) = \frac{\Lambda_0\eta}{2}f(t-\frac{z}{v_0-c_s})+\frac{\Lambda_0\eta}{2}f(t-\frac{z}{v_0+c_s}), \tag{2.40 a}$$

$$v_1(z,t) = -\frac{\eta c_s}{2} f(t - \frac{z}{v_0 - c_s}) + \frac{\eta c_s}{2} f(t - \frac{z}{v_0 + c_s}), \qquad \text{(2.40 b)}$$

$$I_1(z,t) = \frac{\eta I_0}{2}[1 - \frac{c_s}{v_0}]f(t - \frac{z}{v_0 - c_s}) + \frac{\eta I_0}{2}[1 + \frac{c_s}{v_0}]f(t - \frac{z}{v_0 + c_s}). \qquad \text{(2.40 c)}$$

Equation (2.40) indicates that energy modulations and line charge density modulations can be generated from initial current modulations. Note from equation (2.40) that the fast and slow waves have the same polarity in the current profile, but the opposite sign in the energy profile. On the other hand, the current profile has different amplitudes for the fast and slow wave, while the velocity profile has identical amplitudes for both components. During the experiment, normally a "pure" current perturbation is obtained by neglecting the relatively small velocity modulations.

When the initial velocity perturbation is dominant, i.e. $\delta \gg \eta$, using a similar analysis, we can reduce the equation (2.35) to

$$\Lambda_1(z,t) = -\frac{\delta\Lambda_0}{2}(\frac{v_0}{c_s} + 1)f(t - \frac{z}{v_0 - c_s}) + \frac{\delta\Lambda_0}{2}(\frac{v_0}{c_s} - 1)f(t - \frac{z}{v_0 + c_s}), \qquad \text{(2.41 a)}$$

$$v_1(z,t) = \frac{\delta v_0}{2}(1 + \frac{c_s}{v_0})f(t - \frac{z}{v_0 - c_s}) + \frac{\delta v_0}{2}(1 - \frac{c_s}{v_0})f(t - \frac{z}{v_0 + c_s}), \qquad \text{(2.41 b)}$$

$$I_1(z,t) = -\frac{\delta I_0}{2}(\frac{v_0}{c_s} - \frac{c_s}{v_0})f(t - \frac{z}{v_0 - c_s}) + \frac{\delta I_0}{2}(\frac{v_0}{c_s} - \frac{c_s}{v_0})f(t - \frac{z}{v_0 + c_s}). \qquad \text{(2.41 c)}$$

## 2.3 General remarks

We have discussed the generation and propagation of space-charge waves in simplified 1-D models. Any density or energy perturbations can stimulate space-charge waves with fast and slow components. The wave behavior is very similar to that of sound waves, thus the phase velocity $c_s$ is called the "sound speed". For the case of a pure initial current perturbation, according to equation (2.40), one can find that the amplitudes of fast and slow wave in both current and energy profiles are related to $c_s$. The speed for the separation of fast and slow waves depends on $c_s$ too. Therefore, the sound speed is very important to characterize space-charge waves in beams. The definition of $c_s$ indicates that the space-charge waves will propagate faster with larger unperturbed line charge density and a bigger g-factor, i.e. a smaller transverse beam size. Furthermore, one can also conclude that with higher current or smaller beam radius, larger energy modulations can be obtained with the same initial pure current modulation strength $\eta$.

Even though our analysis in Sec. 2.2 neglects the transverse beam dynamics, the transverse physics still affect the longitudinal space-charge waves via the g-factor, which depends on the average beam radius in space-charge dominated beams. However, the derivation of g-factor is based on assumption of a conducting wall boundary, the long wavelength-limit, and uniform volume charge density in the beam. In reality, the beam transport channel cannot be an ideal conductor due to the small resistance of the metal pipes and various discontinuities. The density distribution inside the beam is usually very complicated and does not follow any well known distribution function. In addition, the average beam radius along the beam may not be

constant but varied due to periodic focusing and/or mismatching. Nonetheless, previous experimental observations have verified the linear 1-D cold fluid model and derivation of g-factor for small perturbations [22, 26]. However, for cases of nonlinear perturbations and more complicated transverse distributions, it still remains as an interesting topic for investigation.

# Chapter 3  High Resolution Measurement of Energy Profiles of Space-charge Waves

As indicated by the 1-D theory, one can expect a space-charge dominated beam with a pure density modulation to develop energy modulations further downstream. However, due to the lack of high resolution energy analyzers, most previous experimental studies on space-charge waves focused on the evolution of density modulations and have no precise measurements on energy modulations. To address this issue, a third-generation high resolution energy analyzer has been developed in the UMER lab and installed in a 2.5 m long beam transport line set up at the University of Maryland to study the longitudinal space-charge perturbation and energy spread evolution in a long uniform focusing channel [36].

In this chapter, we will present experimental observations of the energy modulation converted from the initial density perturbation. The experimental results are supported by analytical solutions of the one dimensional theory and the particle-in-cell (PIC) code simulations. First, in section 3.1, we give an overview of the long solenoid experiment (LSE) system, where most experimental studies are carried out in this thesis. Next, in section 3.2, we describe several different methods for generating current or energy modulations deliberately. Then, in section 3.3 and section 3.4, we show some measurements of energy perturbations using high resolution energy analyzers in LSE and compare experimental results with 1-D theoretical calculations and PIC code simulations. Finally, we summarize the new

progress in understanding of space-charge waves and discuss some unresolved

problems in section 3.5.
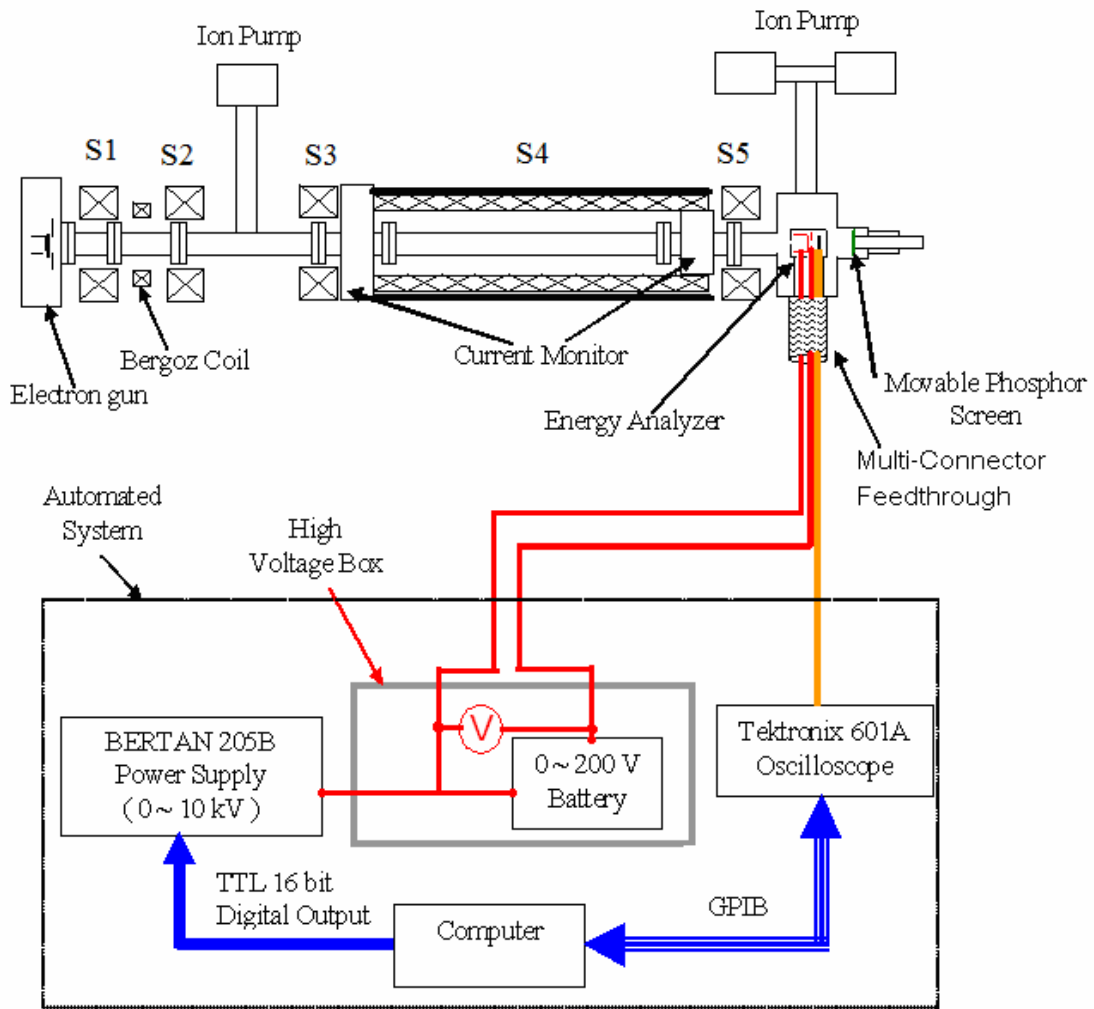


Figure 3.1: Schematic of the long solenoid experiment system setup [37].

## 3.1 Long Solenoid Experiment System

The Long Solenoid Experiment system (LSE) is the major experimental platform that was used during our experimental studies. In Sec. 3.1.1, we briefly describe the basic parameters and layout of the LSE system, and then in Sec. 3.1.2 and 3.1.3 we depict more about the electron gun and high resolution energy analyzers. Finally, the upgraded long solenoid experiment system is detailed as well as the reason for the upgrade.

### 3.1.1 Overview of the system

The Long Solenoid Experiment system is a linear system with solenoids serving as the basic focusing magnets [38]. Due to the straightforward design, the LSE system serves as both a facility to carry out beam dynamics experiments and a test bed of diagnostic tools for the University of Maryland Electron Ring. The schematic of the system is shown in Fig. 3.1. A Pierce type gridded thermionic electron gun is used as the source of the electron beam. The nominal operating beam energy of the LSE system is 5 keV, but the gun could also be operated in a large range from 1 kV to 10 kV. With the help of collimating apertures on a rotating plate near the beam waist, the size and the output current of the electron beam can be varied. The whole system is about 2.5 m long from the plane of the electron gun aperture to the middle plane of the diagnostic chamber where a high-resolution energy analyzer is installed. The long solenoid S4, which is 1.4 m long, serves as a uniform focusing channel to transport the beam into the energy analyzer. In order to match the beam into the long solenoid, three short solenoids, S1, S2 and S3, are placed in the system. Another short solenoid S5 is placed between the exit of the long solenoid and the energy analyzer in order to

control the amount of current injected into the energy analyzer. The axial magnetic field profiles along the axes of these solenoids were measured with a Hall probe. The fields off-axis can be obtained using the formulas in reference [23] derived from a Taylor expansion of the measured on-axis field. Mathematically, the effective length $L_{eff}$ of each of these solenoids can be defined by:

$$L_{eff} = \frac{1}{B_0^2} \int_{-\infty}^{\infty} B_z^2(z)dz ,$$ (3. 1)

where $B_0$ is the peak magnetic field along the axis and $B_z$ is the axis field as a function of the longitudinal direction $z$. The effective length $L_{eff}$ and the distance d between the center of each solenoid and the downstream edge of the gun aperture are shown in Table 3.1. One Bergoz fast current transformer is located between solenoids S1 and S2.

Table 3.1: Data for the solenoids.

|  | S1 | S2 | S3 | S4 | S5 |
| --- | --- | --- | --- | --- | --- |
| d (cm) | 11.0 | 27.0 | 51.6 | 133.5 | 210.0 |
| $L_{eff}$ (cm) | 4.34 | 4.24 | 7.28 | 130.8 | 5.16 |

A very high vacuum at low $10^{-8}$ to high $10^{-9}$ Torr is maintained by four ion pumps. The first ion pump is located at the electron gun with a capacity of 8 L/s. The other three ion pumps have capacities of 40 L/s. One is located between the second and third solenoids and two are located at the diagnostic chamber. The system is connected with an automated measurement system including a high-voltage power supply, a Tektronix oscilloscope (TEK DSA 601A) and a computer. A MATLAB

code was developed to guide the setting of the currents of the solenoids for matching the electron beams into the long solenoid.
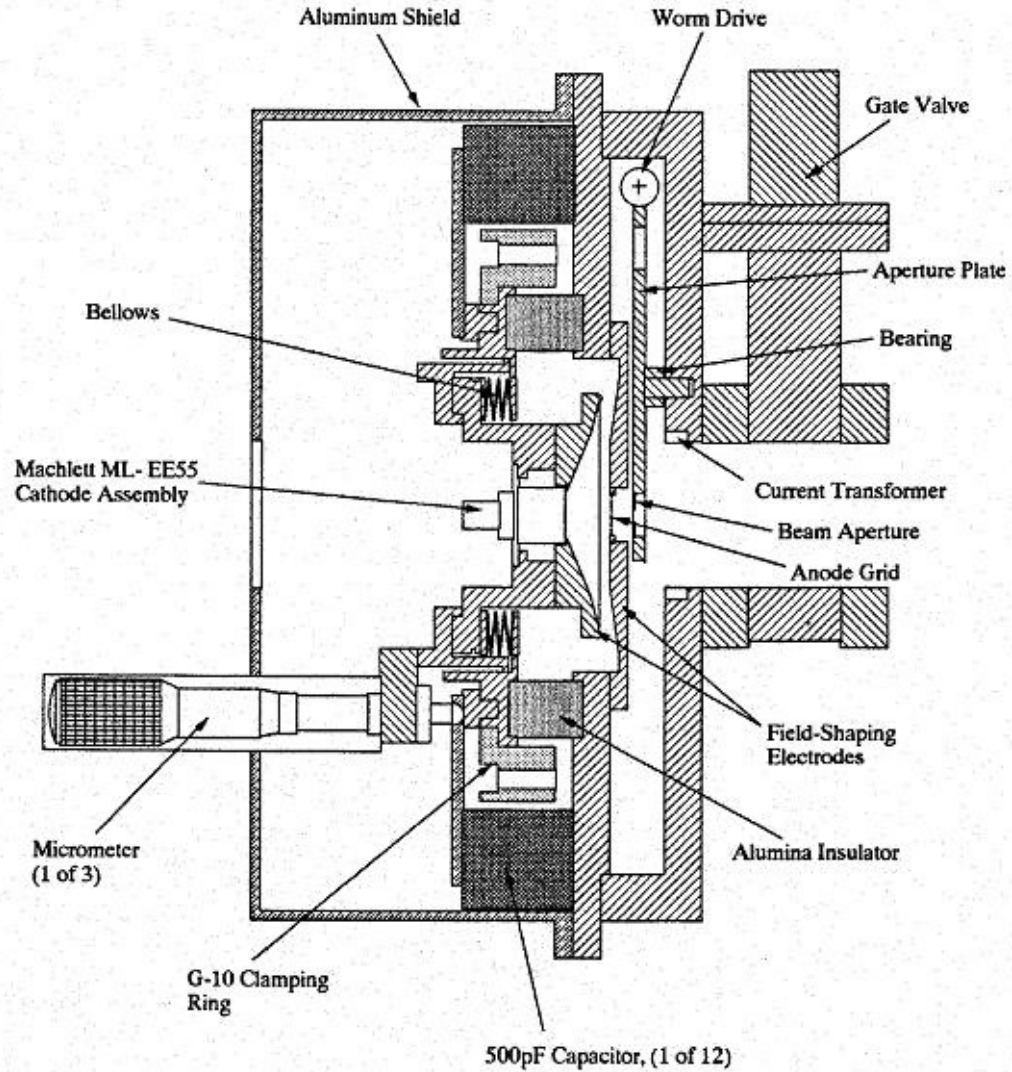
Figure 3.2: Schematics of the gridded electron gun. [39]

## 3.1.2 The electron gun

As illustrated in Figure 3.2, the electron gun used in the system is a variable-perveance gridded cathode gun [39] developed and constructed at the University of

29

Maryland. It has a standard B-type thermionic dispenser cathode, using a porous tungsten matrix impregnated with barium calcium aluminate (6BaO-1CaO-2Al$_2$O$_3$), with a radius of 4mm. Due to the small heated area of around 0.5 cm$^2$, heating inhomogeneity is not a big concern. The electron beam is accelerated between the anode mesh and the cathode and focused by the Pierce cone. The distance between the cathode and anode is adjustable by means of micrometers to anywhere between 9.3 mm and 23 mm, allowing us to change the gun perveance. A collimating aperture plate, which consists of apertures with different sizes and patterns, is located right after the anode and can be rotated by a worm drive to select a specific aperture. Some of these gun apertures are shown as examples in Figure 3.3. To protect the cathode, this gun also has a gate valve to isolate the cathode from the rest of the system.

| (a)Full-size | (b)Hole1 | (c)Hole2 | … | (d)Hole7 |
|---|---|---|---|---|
| d=12.5 mm | d=0.8 mm | D=3.2 mm | … | d=8 mm |
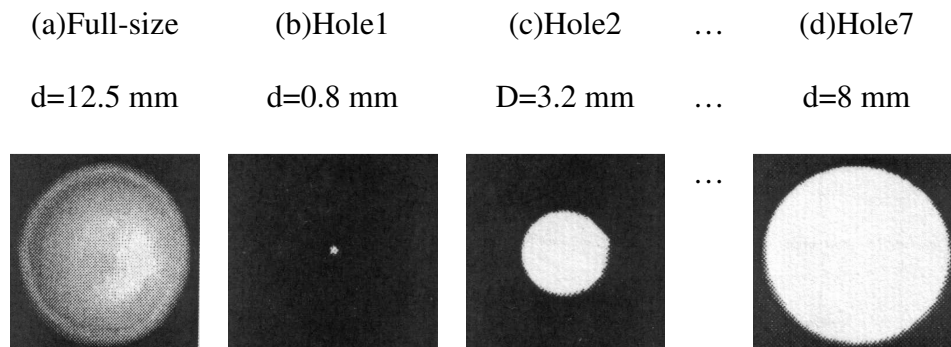
Figure 3.3: Examples of some gun apertures with different diameters d.
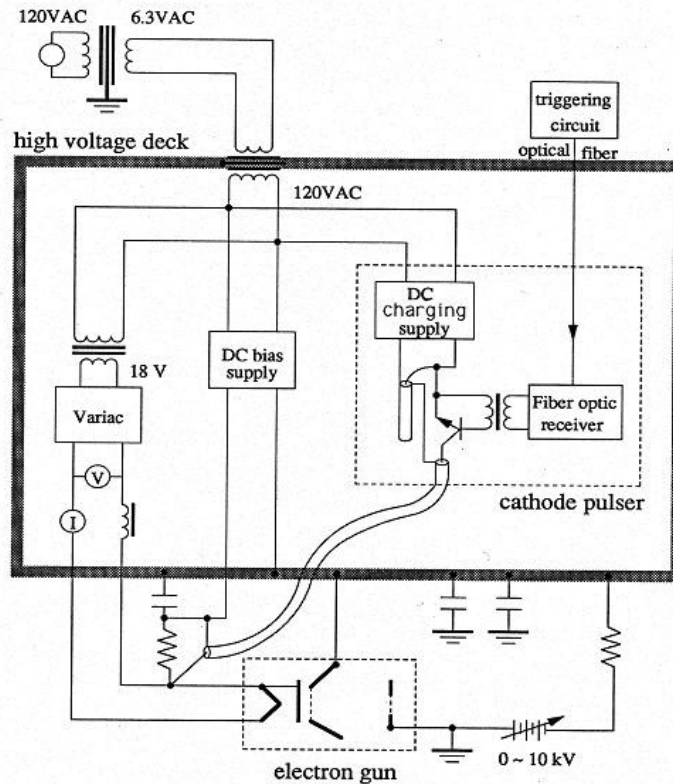
Figure 3.4: The diagram of the gun control circuit. [39]

The cathode is biased by a positive DC voltage relative to the grid to cut off the beam current. During emission, the grid-cathode pulser inside the gun control circuit produces a negative pulse between the cathode and the grid to turn on the beam. Thus, the beam shape and width is dependent on this pulse voltage. The gun control circuit diagram is shown in Figure 3.4. It consists of a high-voltage DC power supply for the anode grid, an AC power supply for the cathode heater, a DC cathode-grid bias power supply, and a grid-cathode pulse voltage generator. This pulse is triggered by an external triggering circuit. As shown in Figure 3.4, the DC high voltage is applied between the anode and grid through a 1-MΩ resistor, which protects the high-voltage power supply from damage in the event of a large discharge when the power supply

31

turns off. All the electronics are located in a high-voltage deck, which is isolated from the ground and charged up to –10 kV, except for the external triggering circuit, which generates a trigger signal by detecting the zero current of the AC power line and is connected to the electronics inside the high voltage deck by fiber optics and an insulated transformer.

The cathode pulser is composed of an external triggering circuit, a pulse forming line (PFL), a 2N3507 transistor, and a DC charging power supply. When the external trigger circuit provides a trigger signal, it is coupled by the fiber optics and forms a forward bias pulse between the base and emitter of the transistor. Since the DC bias of the emitter is -130V and that of the collector is 30V, as soon as the transistor is turned on by the forward bias pulse, it is working in the avalanche mode, where the transistor basically serves as a fast switch for a large dc current flowing through the transistor. When the DC current flows through the 50-$\Omega$ matching resistors, a voltage drop of about 60V is generated and applied between the grid and cathode to turn on the beam. The avalanche current will be terminated, i.e. the falling edge of the pulse voltage will form, when the reflection current comes back from the open end of the PFL. So the length of the transmission line determines the width of the pulse voltage, hence determines the beam pulse width. Normally, we fix its length to 10 m for producing a 100 ns beam pulse. A typical grid-cathode pulse signal is below -60 V with a rise time of 2 ns, running at 60Hz.
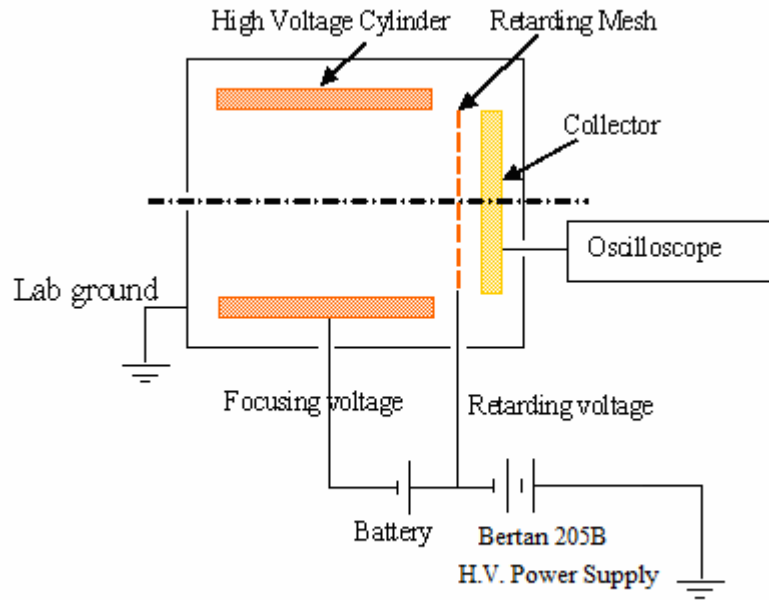
Figure 3.5: The schematic of the high resolution energy analyzer [37].

### 3.1.3 High resolution energy analyzer

At University of Maryland, a high resolution retarding potential energy analyzer has been developed in recent years [40, 41]. In the LSE system depicted in Figure 3.1, a third generation energy analyzer is located in the diagnostic chamber after 4 short solenoids and a long solenoid. It is a compact device with a length of 4.8 cm and a diameter of 5.1 cm, which is convenient to insert into the beam line. In addition, compared with previous generations of energy analyzers, the new design of a focusing cylinder with independently variable potentials greatly enhances its resolution by properly collimating the beam.

The circuit schematic of the device is illustrated in Figure 3.5. A grounded steel plate with a 1 mm diameter circular aperture lets a small amount of beam pass into the high voltage region. The high-voltage steel cylinder with a length of 2.5 cm

and an inner diameter of 2.5 cm serves as a radial focusing electrode in the energy analyzer. The retarding grid is a molybdenum wire mesh with a transmission of 80% mounted on a machinable ceramic (MACOR) ring, which insulates the retarding grid from the focusing cylinder so that the battery inside an external box can supply a voltage difference between the focusing cylinder and the retarding mesh. Both of them are connected to the same external high-voltage source through different high voltage input pins. Behind the high-voltage mesh there is a copper collector plate, from which the current signal is picked up by a 50 Ω BNC connector. As mentioned earlier, the unique feature of this device compared to the preceding generations is that the focusing cylinder is separated from the retarding mesh which allows different potentials between them. The difference between the focusing voltage and retarding voltage has been optimized for different beam energies so that the beam inside the device is well focused for an accurate measurement.

The high-voltage power supply used to retard the beam is a Bertan 205B, which has low noise and high resolution, with maximum output voltage of 10 kV. The output high voltage of the power supply can be controlled locally via a precision front panel or can be remotely programmed by a 16-bit digital signal. A battery provides the offset voltage on the focusing cylinder of the energy analyzer, which is in series with the high-voltage output from the power supply. The energy analyzer output current signal is sent directly to the oscilloscope. To improve the experimental efficiency and resolution, a computer-controlled automated data-acquisition system has been developed [37]. The entire control program is written in C language for high efficiency and low-level controllability. With this system, we can set the scanning

retarding voltage region and voltage step, select signal channel from the oscilloscope, set filter on/off, average number, etc. A full set of data can be taken within several minutes, which is impossible with manual control, formerly the usual method. The data taken by the computer are then automatically processed by a MATLAB code [37], which can analyze the data and display the time-resolved root-mean-square (rms) energy spread, full width at half-maximum (FWHM), peak, and mean energy along the beam pulse.

When the proper focusing voltage is used, the resolutions of this analyzer is less 0.2 eV for a 5 keV beam after considering of error sources such as the device misalignment, ripples of the high voltage power supply, background noise, and data acquiring [42]. However, the unknown temporal behaviors of beams inside the device affect the coherent errors when measuring a beam with energy modulations. This requires more studies in future. In addition, if the current density inside the energy analyzer is higher than a critical value, the longitudinal space-charge effect and the formation of a potential minimum similar to the virtual cathode in an electron gun will distort the measured energy spectrum by shifting it to the low energy end [41]. Therefore, during the measurement, we always try to control the current inside the energy analyzer to be less than 0.2 mA, corresponding to an energy analyzer signal of 10 mV, by changing the solenoid strength in front of the diagnostic chamber.

### 3.1.4 System upgrade of the LSE

As discussed in the previous section, the LSE system provides unique diagnostics and efficient set up for carrying out experimental research on space-charge dominated beams. In later sections, we present some new results obtained from this system that

35

help us understand the longitudinal beam dynamics in space-charge dominated beams. However, problems of the experimental system itself due to insufficient mechanical design and poor vacuum condition limited further experimental studies and urged us to first upgrade the system before any further experimental work.

The major reason for poor vacuum in the old system was the poor sealing of the two resistive wall current monitors, which were located at the entrance and exit of the long solenoid channel respectively as shown in Figure 3.1. In addition, the movable phosphor screen connected to the end of the beam transportation line relied on a differential pumping system which contains two vacuum regions. However, in practice when one tried to move the screen into the system, the pressure could rise to $10^{-6}$ Torr. Therefore, the movable phosphor screen, the only transverse diagnostic tool in the system, could not be used for transverse imaging of the beam at all. In the upgraded LSE system, we have not only fixed these problems but also implemented new diagnostic tools into the system.

The schematics of system upgrade are shown in Figure 3.6. A new diagnostic chamber LC1 has been installed to replace the three-way cross in the old LSE system between the second and third solenoid. The new chamber has five ports which connect to beam lines, the vacuum pump, a view window and a diagnostic complex feed through. Inside LC1, we installed a new energy analyzer, which is identical to the one previously installed in the chamber after the long solenoid except that a phosphor screen is attached to the bottom of the energy analyzer. The photo of the new diagnostic complex is shown in Figure 3.7. The phosphor screen is mounted inside the groove on the surface of a cubic bracket. A mirror inside the bracket is

36

aligned at 45 degrees with respect to the phosphor screen and the beam propagation direction so that the image of the beam in the mirror is parallel to the view window of chamber LC1. Another small mirror is attached to the bottom of the bracket and will be used to direct a laser beam to the cathode for generating photoemission. By moving the diagnostic complex up and down, one can use either the energy analyzer or phosphor screen to intercept the beam. Hence, both the longitudinal energy information and transverse distribution of the beam can be measured at the same location.
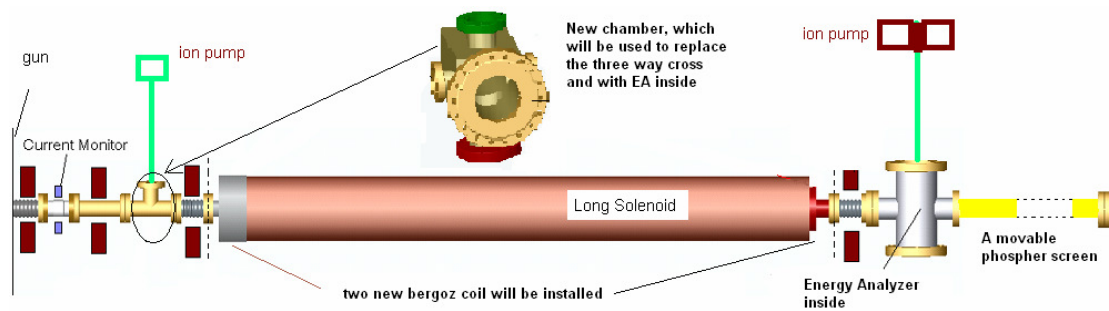


Figure 3.6: The schematics of the upgraded LSE system which includes a total of two diagnostics chambers, three Bergoz current monitors, and a new movable phosphor screen.

The two resistive wall current monitors were replaced by two new fast Bergoz current monitors identical to the one installed between the short solenoid S1 and S2. Besides being useful for matching the beam into the long solenoid, these two new current monitors can provide more information of current profiles and help us

understand the evolution of the current perturbations. Furthermore, to increase the signal to noise ratio, housings to shield each current monitor from external noise were also added to the system. These housings also help in increasing the system robustness, supporting the Bergoz monitors away from the glass gaps.
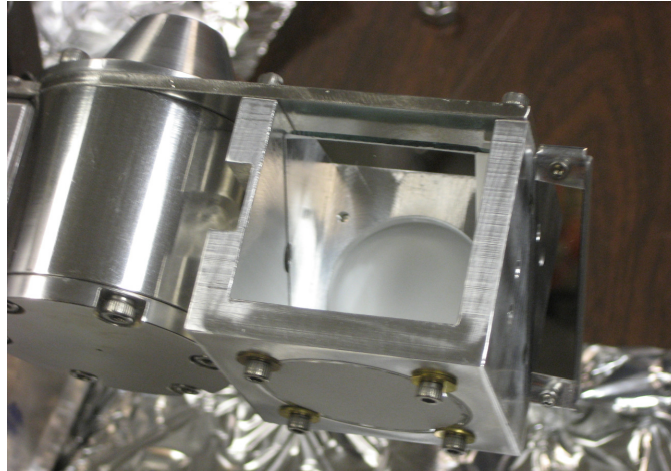


Figure 3.7: Diagnostic complex in the first diagnostic chamber: energy analyzer (left), fast phosphor screen with mirror (center), and small mirror for laser (right).

An important part of the upgrade is the installation of a new magnetically-actuated phosphor screen slider, with excellent vacuum compatibility. The new slider has a range of about 80 cm, covering the entire range from beyond the second chamber to the last 30 cm of the long solenoid. As shown in Figure 3.8, an internal magnetically-actuated tube holds the phosphor screen and its movement is controlled by a magnetic actuator, which is a slidable aluminum collar with built in magnets. A view window at the right end of the slider enables image capture using a camera with a telephoto lens. The whole system can be separated by a gate valve from the rest of the experiment.

Figure 3.8: The new movable phosphor screen installed in the system.

In addition to the planned hardware upgrade, some other system improvements have also been undertaken necessitated by the aging of the components. For example, because the dispenser cathode's time in operation was approaching its lifetime limit, its emission became low and instable with time. To solve this problem, the cathode has been replaced by a new one. We also practically rebuilt the gun pulsed electronics, replacing many components and redesigning parts of the circuit for clean output signal with lower noise. The rebuilt pulse voltage generation circuit is shown in Figure 3.9 as an example.

As shown in Fig 3.10, the upgraded experimental system now includes a comprehensive set of diagnostic tools which include two energy analyzers, three

Bergoz current monitors with typical rising time of 200 ps, and two phosphor screens. Due to the insertion of new components, the positions of the solenoid magnets have been changed and the new data are shown in Table 3.2, where B1, B2, and B3 represent the three Bergoz current monitors.

Table 3.2: Distance in cm from the center of the solenoids, diagnostic chambers, and Bergoz current monitors to the downstream edge of the gun aperture.

| S1 | S2 | S3 | S4 | S5 | LC1* | LC2** | B1 | B2 | B3 |
|------|------|------|-------|-------|------|-------|------|------|-------|
| 11.0 | 29.0 | 55.0 | 136.0 | 217.0 | 40.5 | 234.0 | 18.5 | 63.0 | 207.0 |

\* This is the distance from the front surface of the phosphor screen or the energy analyzer to the gun aperture plate.
\*\* This is the distance from the front surface of the energy analyzer to the gun aperture plate.
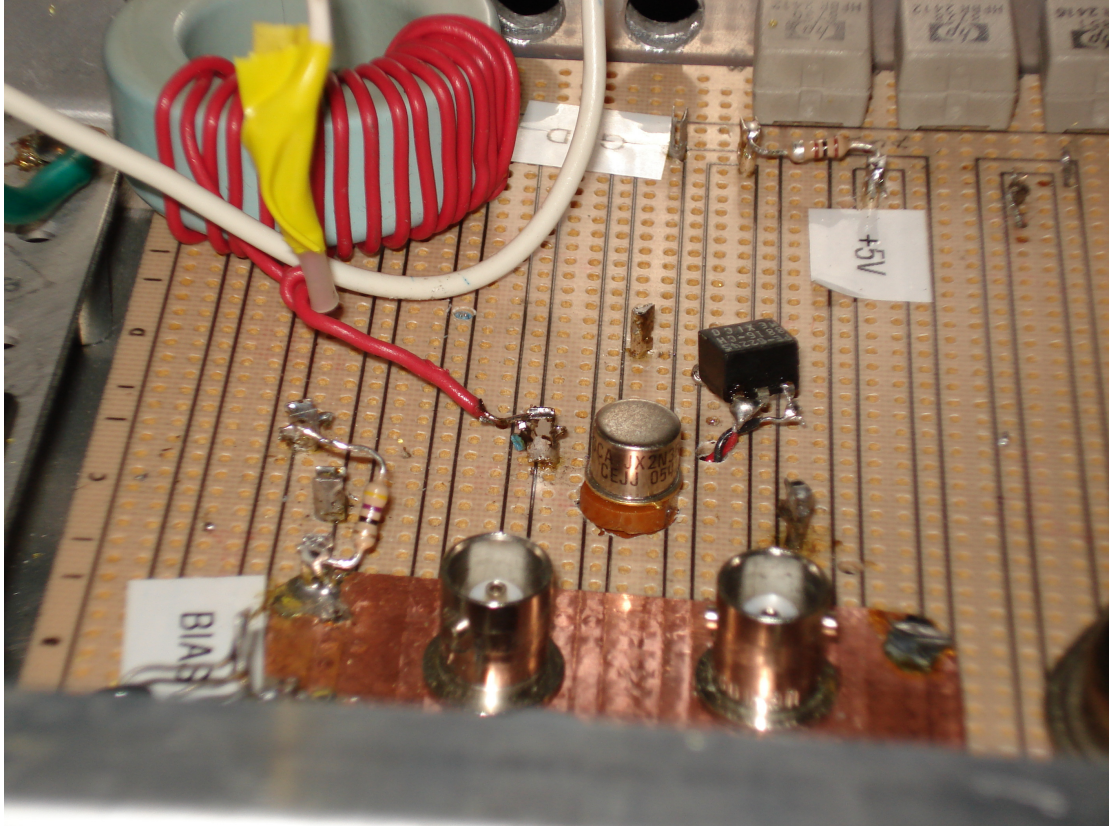
Figure 3.9: The rebuilt pulse generation circuit of the control electronics for the electron gun.
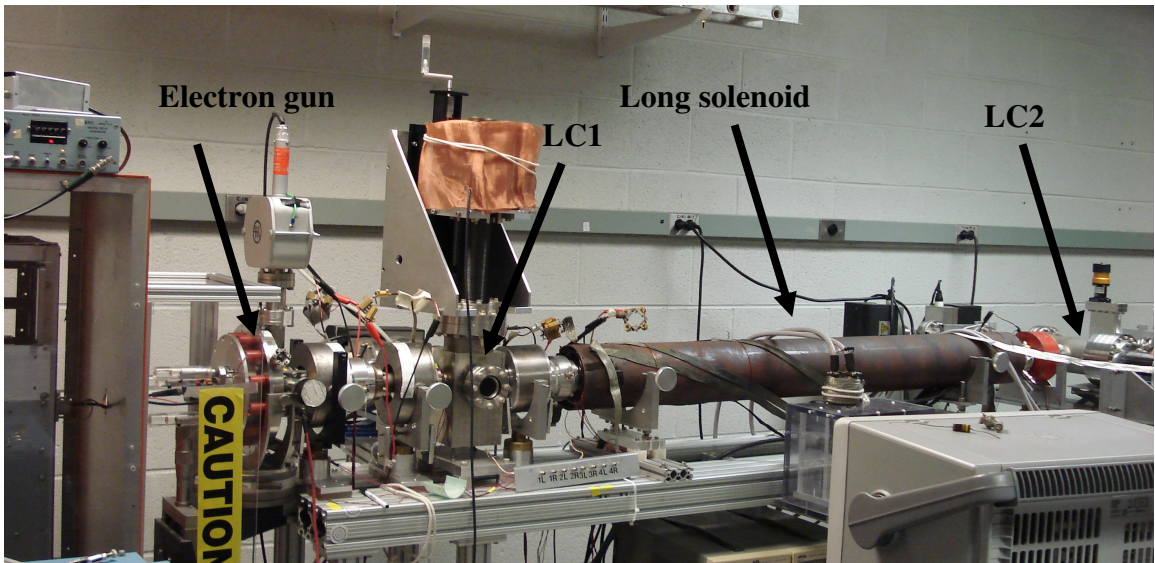


Figure 3.10: The upgraded long solenoid experiment system.

## 3.2 Generation of perturbations

In order to understand the physics involved in the evolution of the perturbations in space-charge dominated beams, we need to generate controlled perturbations to the beam. We have several ways to introduce initial density or energy modulations deliberately to the beam: an induction module (Sec. 3.2.1), an optical method (Sec. 3.2.2), and an electronic method (Sec. 3.2.3). For the experimental work related to this thesis, we used the electronic method, which is described in great detail later.

### 3.2.1 An induction module

The induction module is installed in the ring section at UMER and has the main purpose of focusing the beam longitudinally and preventing the beam end expansion. Recently, others have been able to apply a pulsed voltage of about 600 V in 8 ns to the beam longitudinally [43]. As a result, the beam energy can be modulated by the voltage pulse, and by changing the amplitude of the pulse signal, the energy perturbation strength can be changed accordingly.

### 3.2.2 Laser induced perturbations

Both the cathodes of the UMER and LSE electron guns are dispenser cathodes with photo emission capability. Thus, we can impinge a laser beam onto the cathode to generate pure density perturbations over the thermionic emission when the cathode is operated in the temperature limit regime [30, 31, 44]. In both systems, a Minilite II Q-switched Nd:YAG laser from Continuum has been used and the third harmonic laser which has a wavelength of 355 nm and 5 ns FWHM was directed into the vacuum chamber and the cathode eventually by a set of optical mirrors. By tuning the

laser power, we can vary the perturbation strengths without changing the thermionic emission. In addition, it is also possible to generate multiple perturbations by increasing the laser power high enough to achieve nonlinear oscillation in the laser profile. However, because the cathode needs to be operated in the temperature limited regime where the thermionic emission is very sensitive to the variation of temperature, it is very critical to keep a stable heating current of the cathode in order to generate a stable beam profile with laser induced perturbations.

### 3.2.3 Generate perturbations electrically

The original technique, which has been used to generate density perturbations during past years [21], is to deal with the grid cathode pulse voltage of the electron gun, of which the circuit schematics have been discussed earlier. A gridded cathode gun has a triode structure; hence, the gun can be operated in three regimes: cut off, amplification, and saturation. In saturation, the output current of the electron gun is not sensitive to the shape of pulse voltage, i.e. the current pulse shape shows a nice rectangular shape without any signatures of the imperfection of the grid cathode pulse voltage. Hence, normally the bias voltage is chosen to operate the gun in saturation mode. If the bias voltage is increased from the normal setting, the gun then will be in the amplification mode, where the fluctuations in the control voltage pulse are being amplified and appear in the output current profiles. As a result, the amplification mode provides a way to modulate beam current by modulating the gun pulse voltage.

A cable loop is connected to the middle of the pulse generation transmission line through a "T" connector. As a result, a perturbation is generated at the center of the voltage pulse due to the mismatch. By connecting or disconnecting the mismatch

cable, we can turn on or off the density modulation in the beam. As shown in Figure 3.11, the trace obtained from the oscilloscope is the pulse voltage signal with the mismatch modulation generating from the cable loop. The amplitude of the pulse voltage without perturbation is about -67.5 V, and that of the perturbation is about 15 V. The typical nominal beam energies are 5 keV for experiments at LSE, so we can estimate that the relative strength of the voltage perturbation is in the order of $10^{-3}$. However, one should note that the pulse signal in Figure 3.11 was taken without any beam, thus the exact voltage signal applied between the grid and cathode during beam emission is unknown and may be different from what we are shown here.



Figure 3.11: The pulsed voltage signal between the grid and cathode when the perturbation cable is connected to the PFL.

44

The analysis in Ref. [45] shows that the perturbation generated using this method is always predominant by the current modulation rather than the velocity modulation, i.e. $\eta \gg \delta$, where $\eta$ and $\delta$ are defined in equation (2.33). However, one should note that we can neglect the initial velocity modulation for the evolution of space-charge waves only when the dimensionless parameter $\alpha$, which is defined by equation (2.38), is much less than 1.

Typical current waveforms with perturbation resulting from the perturbed pulse voltage are shown in Figure 3.12. For the case of positive perturbation, the polarity of the current perturbation is consistent with that of the pulse voltage signal. In other words, the beam gains more current at the location of the perturbation. However, we found experimentally that by increasing the AK gap of the gun or applying a gun aperture, a negative current perturbation, which reduces localized beam current, could be generated using the same pulse voltage signal shown in Figure 3.11. An example has been shown on the left in Fig 3.12. The mechanism of the generation of negative perturbations can be found in Ref. [45] and Ref. [23].



Figure 3.12: Beam current profiles with negative (left) and positive (right) perturbations.

## 3.3 Observation of energy modulations converted from current modulations in the LSE before upgrade

One way to verify the one dimensional cold fluid model is to experimentally measure the evolution of space-charge waves. Previous studies have successfully demonstrated the propagation of space-charge waves by measuring the current profiles [21, 30]. In this section, we report the first precise measurement of energy profiles of space-charge waves in the LSE system before upgrade. Using the electrical method mentioned earlier, we generated beams with different current perturbations from the gun (Sec. 3.3.1) and measured the energy profiles with the high resolution energy analyzer in the downstream diagnostic chamber (Sec. 3.3.2). As the one dimensional theory predicts, energy modulations were obtained downstream. In Sec. 3.3.3, we compare the experimental results with analytical results from one dimensional theory and simulation results from WARP.

### 3.3.1 Initial current perturbations

In order to generate current perturbations with different strengths, we managed to operate the gun in amplification mode and changed the bias voltage to obtain different perturbation strengths. Four groups of electron beams with different main beam currents and different strengths of current perturbations are achieved, as shown in Table 3.3, where $V_b$ represents the bias voltage, $I_0$ represents the main beam current, $I_1$ represents the perturbation current, and $\eta$ is the current perturbation strength, defined as $I_1/I_0$.

Table 3.3: Data for current perturbation generation at the gun.

| | $V_b(V)$ | $I_0$ (mA) | $I_1$(mA) | $\eta$ |
|---|---|---|---|---|
| Case (a) | 2 | 69.6 | 3.97 | 0.057 |
| Case (b) | 14 | 77.4 | 10.85 | 0.137 |
| Case (c) | 30 | 67.2 | 16.00 | 0.226 |
| Case (d) | 32 | 45.6 | 13.20 | 0.29 |
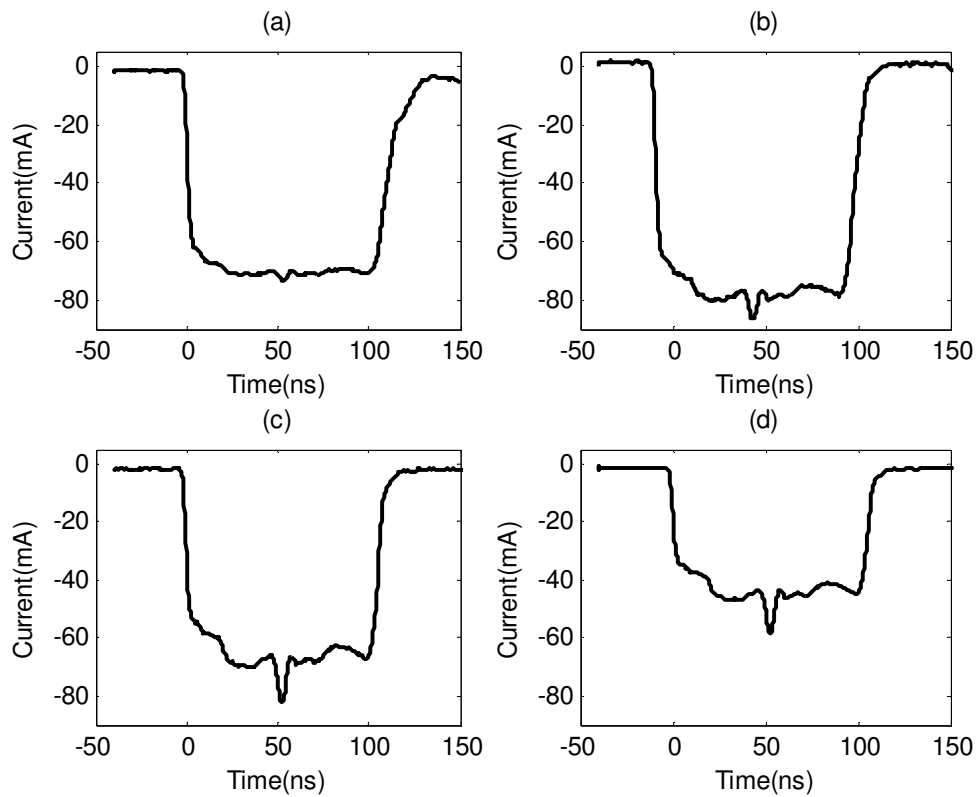


Figure 3.13: Four initial beam currents profiles with different perturbation strengths.

The current profiles in Figure 3.11 are acquired from the Bergoz current monitor between matching solenoids S1 and S2. Consistent with the previous analysis for the different working regimes of the electron gun, the strength of the current perturbation increased with the bias voltage due to the increasing amplification factor. But this is not necessarily true for the perturbation amplitude after comparing the value of $I_1$ for the case of $V_b$=30V and $V_b$=32V. It is also not unexpected to see that the main beam currents are affected by the changing bias voltage and the current shapes are not clean due to operation in amplification mode. However, one may expect a monotonic decreasing of the main beam current when the bias voltage is increased. The three cases for bias voltage of 14V, 30V, and 32V comply with this expectation, but the case for the lowest bias voltage of 2V has less current than the case for a higher bias voltage of 14V. The reason for this conflict is because we had an aged cathode with low emission and less stability over a long time. Furthermore, due to the low emission of the aged cathode, even when the bias voltage was only 2V, the electron gun still worked in the amplification regime. In spite of all the abnormal behavior of the cathode, we found that the beam was still relatively stable during our data collection period, which was about 5 minuets in each case. Therefore, for the experimental results presented in the following section, the cathode condition is not a significant consideration.

### 3.3.2 Measurement of energy modulations

According to the theoretical predictions we discussed in chapter 2, any perturbations in the beam can launch space-charge waves. As shown in Figure 3.13,

the current perturbations can be obtained from the longitudinal current profile measured by the Bergoz current monitor. In order to measure energy profiles of space-charge waves in beams, we need to use the high resolution energy analyzer, which can measure the time resolved longitudinal energy spectrum in the beam. By integrating the energy spectrum, the longitudinal mean energy profile along the beam can be calculated.
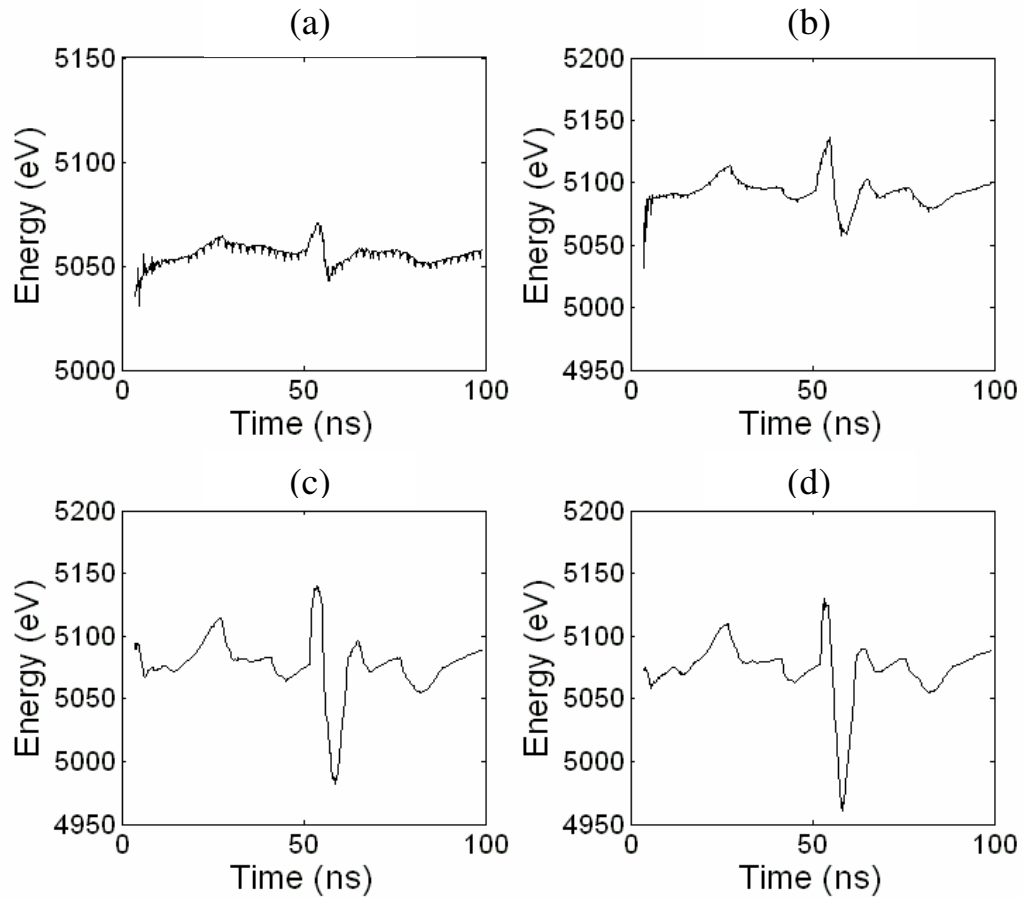


Figure 3.14: Mean energy waveforms derived from energy analyzer signals for different cases.

In Figure 3.14, we plot the mean energy along the beam at a distance of 2.3 m after the gun for the four different beams corresponding to those shown in Table 3.3 and Figure 3.13. Because we are only interested in the localized space-charge waves stimulated by current perturbation near to the beam center, in Figure 3.14, the energy profiles have been zoomed in and do not show the beam edges. As one would expect, with an initial condition of "pure" current modulations, energy modulations can be achieved, which split into two peaks at the beam center. One is positive and close to the beam head, corresponding to the fast wave, the other is a negative peak and near to the beam end, corresponding to the slow wave. According to the one-dimensional cold fluid theory, the peaks of the fast wave and the slow wave should have the same amplitude. However, here we see some inconsistency with the theoretical predictions. Especially for the result of case d, the amplitude of the slow wave is much larger than that of the fast wave. The reason for this is not clear up to now. However, it may be related to the following aspects: First, in case c and case d, strengths of current perturbations are more than 20% of the main beam current, so nonlinear effects should not be neglected, while the one-dimension theory has the assumption of linearity, which implies that the strength of the perturbations must be small in comparison with the beam current, say <10 %. Second, during the experiments, the beams are not stable enough due to the aging problem, which could also cause minor errors of the measurements.

Another observation is that some other peaks are obtained for these four groups of results. Compared with the initial currents in Figure 3.11, it is apparent that they are due to the bumps near the beam head and beam end. In other words, these

fluctuations are due to the imperfect rectangular shape of the beam current, which results from the oscillations in the waveform of the pulse voltage signal. Here we only focus on the peaks for the slow wave and fast wave at the beam center, which is stimulated directly by the intentional current modulations we introduced.

### 3.3.3 Comparison of simulations, experimental results and theory

For more complicated cases, where it is not easy to carry out an experiment, numerical simulations are more flexible for predicting the evolution of the space-charge waves. However, before using the simulation code to predict new physics results, we need to first validate the code itself. Therefore, to check the prediction for the evolution of space-charge waves by the simulation code, we want to benchmark simulations with the experimental data presented in the previous section and analytical results from the one-dimensional cold fluid theory. In addition, by comparing these results, we can discover new physics in the experiment. In the following paragraphs, we will describe the simulation procedure in more detail.

WARP is a particle in cell (PIC) code. It uses macro-particles to do the numerical calculation. Each macro-particle represents a large number of real particles in the experiment. Before starting the simulation, initial conditions such as density and velocity distribution of macro-particles need to be specified first. In addition, to calculate the field distribution, a number of grids need to be defined in space. On each grid point, the self-consistent electric and magnetic fields are calculated from the distribution of macro-particles and boundary conditions. The macro-particles are pushed by the fields, which is interpolated from the self-consistent fields on the

neighboring grid points, to new positions with a new distribution. Then the calculations of new fields and new particle distributions are iterated until the end of simulation.
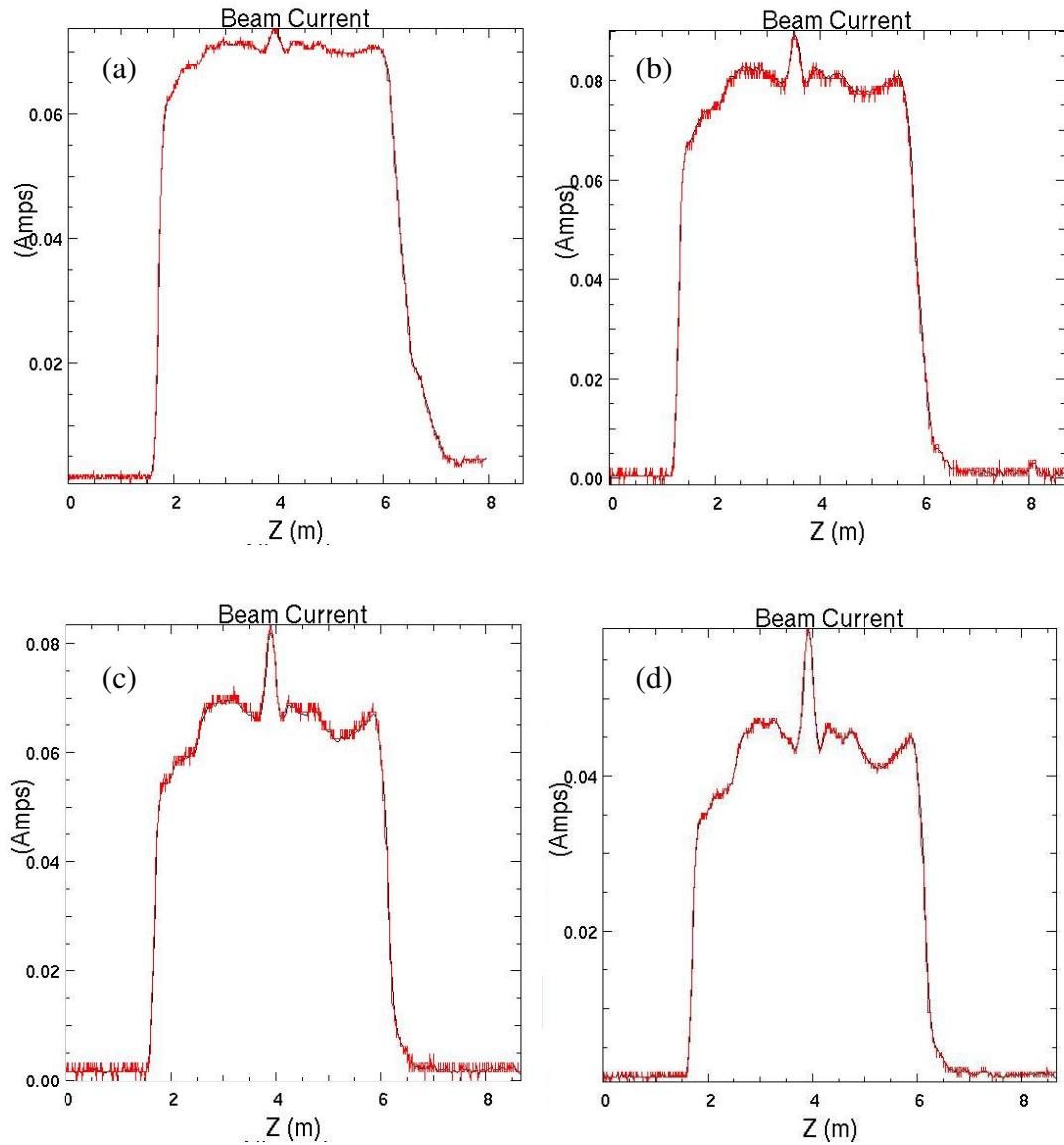


Figure 3.15: The initial current profiles imported into WAR for the 4 different cases.

First, the current profiles of different beams with perturbations, measured by the Bergoz current monitor, were imported into the WARP code to serve as the initial conditions for the longitudinal current distributions. Figure 3.15 shows the current profiles used in the WARP code. A considerable amount of digital noise is observed in these current profiles which are shown in red. In order to reduce the noise, the data was smoothed before the WARP simulations were started. The smoothed current profiles appear as the black solid lines in Fig 3.15. Since we used the beam frame as the reference frame in WARP, the current profile was transformed from lab frame to beam frame by multiplying the time by the nominal beam velocity. We also assumed that there were no energy perturbations initially. Then, the parameters such as beam radius $a$, main beam current $I_0$ and main beam kinetic energy $E$ were set up in the WARP code. Using the magnetic field strength of the long solenoid channel from the experiment, the matched beam radius could be calculated according to the following envelope equation:

$$\kappa_0 a - \frac{K}{a} - \frac{\varepsilon^2}{a^3} = 0 \tag{3.2}$$

where R is beam radius, $\varepsilon$ the transverse emittance. K is the generalized beam perveance defined as equation (2.3), $\kappa_0$ is the external focusing strength defined by

$$\kappa_0 = \left( \frac{qB_z(z)}{2mc\beta\gamma} \right)^2 . \tag{3.3}$$

where $B_z(z)$ is the axial magnetic field, m is the mass of an electron, c is the speed of light, q is the charge of an electron, and z is the axial distance.

Table 3.4: Beam parameter settings in WARP

|          | $I_0$/mA | $E_0$/eV | $a$/mm |
|----------|----------|----------|--------|
| Case (a) | 69.6     | 5055     | 5.3    |
| Case (b) | 79.2     | 5092     | 5.6    |
| Case (c) | 67.2     | 5074     | 5.2    |
| Case (d) | 45.6     | 5077     | 4.4    |

In the WARP simulations, a "smooth uniform field" corresponding to that of the long solenoid was used to represent the magnetic field variation along this channel. The comparison between measurements and simulations show that this approximation has only a negligible effect on our results. The initial transverse distribution of the electron beams in WARP is a semi-Gaussian distribution, which is uniform in space and Gaussian in velocity space, with a uniform temperature. Since the external focusing magnetic lenses are solenoids, which have transversely angular independent field distribution, a WARP-RZ code was used for simulation the experiments. Different settings for each group are shown in Table 3.4. Other numerical settings for the simulation are: the length of the beam pulse is 100 ns; the particle number is 50000; time step for pushing particles is $2.36 \times 10^{-10}$ second; the number of cells in the r direction is 64; the number of cells in the z direction is 256. All these numerical parameters have been tested with different values and we found that the values listed above are optimal in terms of speed and accuracy for our simulations.
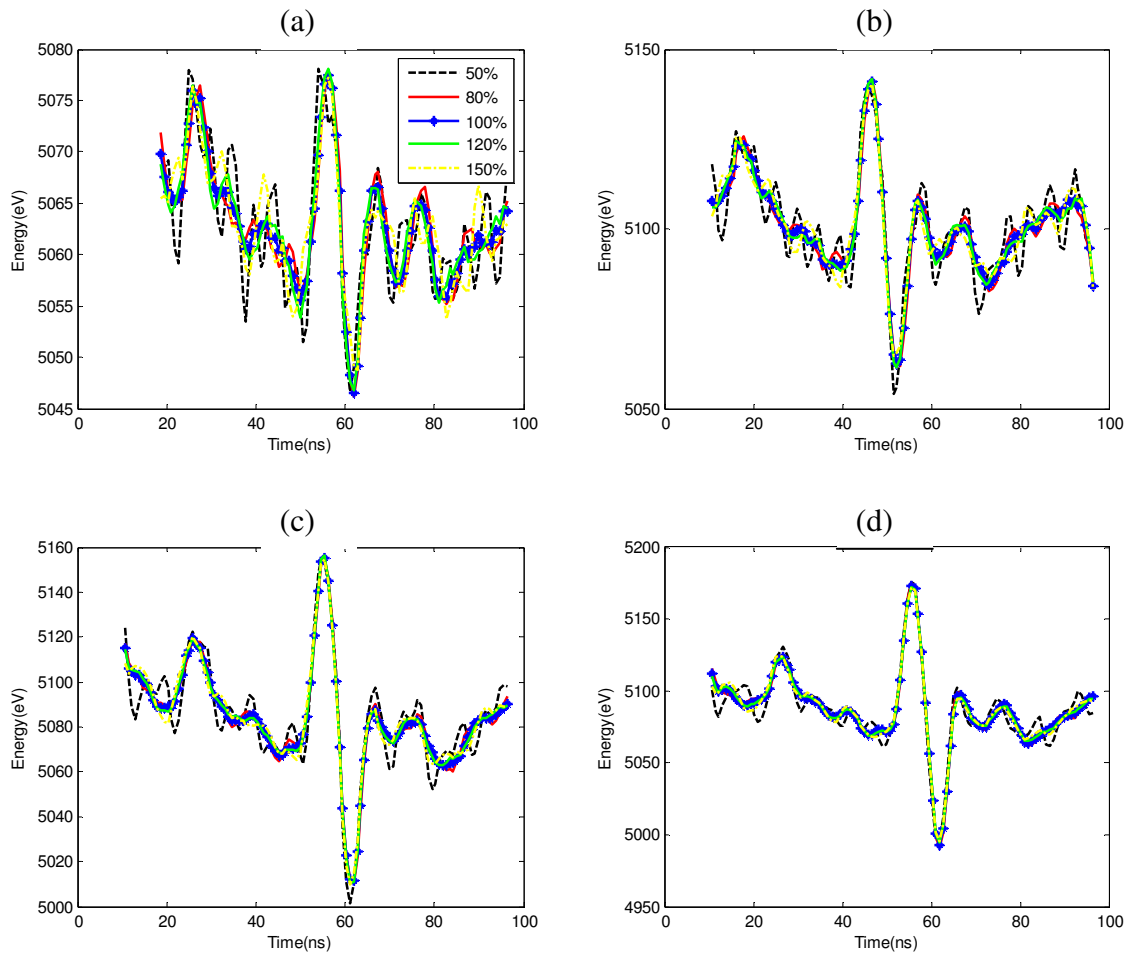
Figure 3.16: The results of mean energy vs. time for different initial beam radii in WARP

After the initial settings, simulations were carried out in the r-z geometry for a channel length of 2.3 m, which is the distance between the Bergoz current monitor and the retarding field energy analyzer in the experiment. One major concern in the accuracy of the simulation was whether our results depend on the beam radius and hence on the extent of transverse mismatch. To answer this question, we performed WARP simulation studies for each group by changing the value of the beam radius.

The mean energy, the initial current, and the focusing fields remained unchanged, but for each case, the initial radius was changed to 150%, 120%, 80%, and 50% of the matched beam radius. By doing this, we could verify the effect of the transverse mismatch on the longitudinal energy profiles. The results of these WARP simulations are plotted in Figure 3.16, which clearly shows that they are insensitive to transverse beam mismatch.
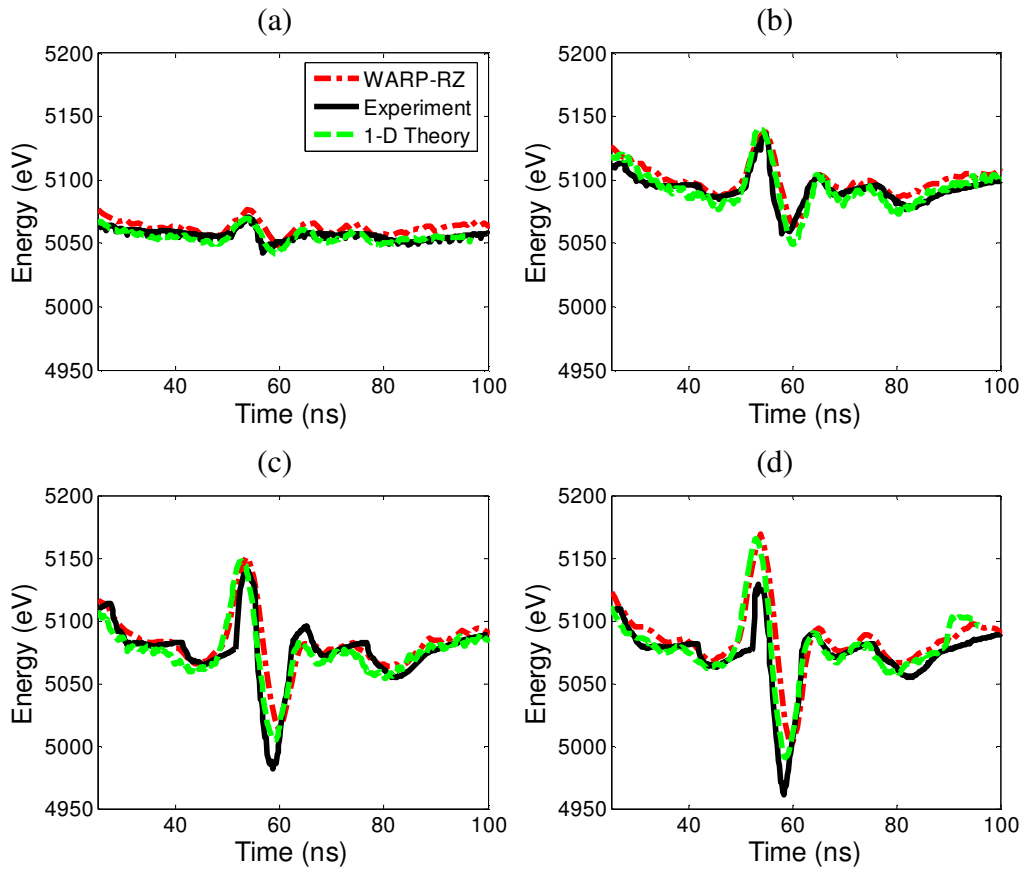


Figure 3.17: Comparisons of the profiles of the mean energy for the experiment results (black solid lines), WARP simulation (red dash dot lines) results and one-dimensional cold fluid theory (green dash lines).

In order to compare the results with the one-dimensional linear theory, the analytical solutions for each group were found using equation (2.40) by assuming the initial velocity perturbation is zero. All the results from WARP, the 1-d theory and the experiment are shown in Figure 3.17. From these curves, similar shapes of energy perturbations for WARP simulation, experimental results, and the one-dimensional cold fluid theory can be observed in each case. Besides the fast wave and slow wave generated near the beam center, some other perturbation peaks with positive and negative polarity can be observed near the beam head and beam tail. In case (a) and (b), we find very good agreement among experimental, simulation, and theoretical results. This verifies the linear theory when the initial perturbation strength is relatively small. In case (c) and (d), although the results from 1-d theory and WARP are very close, they have obvious discrepancy with the experimental results. Especially in case (d), the experimental result indicates a decrease of the amplitude of the fast wave and a growth of that of the slow wave while the simulation and theory predict a symmetric pattern for fast and slow waves.

In order to quantitatively compare the experimental results with simulation and theory, it is useful to compare the peak-to-peak values of the energy waveforms, which are defined as the difference between the peak values of the fast wave and the slow wave. The values for the energy perturbation peak-to-peak strengths $dE/E_0$ predicted or measured at z = 2.3 m using the different methods and initial current perturbation strengths $\eta$, are shown in Table 3.5.

Table 3.5: Energy perturbation peak-to-peak strengths and η

| η | dE/E$_0$ | | |
|---|---|---|---|
| | Experiment | WARP | 1-D theory |
| 0.057 | 0.0056 | 0.006 | 0.0056 |
| 0.137 | 0.0152 | 0.0144 | 0.0179 |
| 0.226 | 0.0312 | 0.027 | 0.0283 |
| 0.29 | 0.0331 | 0.0328 | 0.0345 |
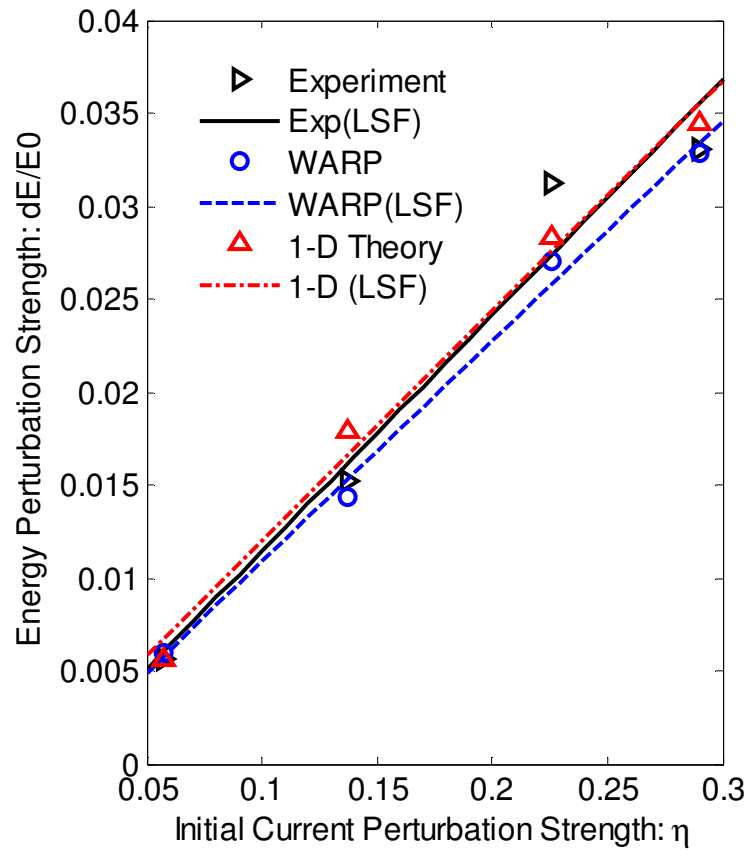


Figure 3.18: Energy perturbations strengths versus initial current perturbations strengths for experimental data, WARP simulations, and 1-D theoretical calculations. The least square fit (LSF) results are also plotted for comparison.

Figure 3.18 shows the relationship between $dE/E_0$ and $\eta$ based on the data in Table 3.5. The experimental results show very good agreement with both WARP simulation and analytical results based on the one-dimensional cold fluid theory. All these results show that the peak-to-peak strength $dE/E_0$ of the energy modulation grows linearly with the current perturbation strength $\eta$, and the slope is about 0.1. Using the least square method, the slope can be calculated: for the experiment data, which yields 0.127; for the WARP simulation results it is 0.119, and for the one-dimensional theoretical prediction, it is 0.124. Therefore, the conclusion can be drawn that good predictions of the energy perturbation strength evolution can be derived from the WARP simulation and the one-dimensional cold fluid theory.

In both the 1-D model and WARP simulation mentioned above, we assume that the initial velocity perturbation is equal to zero. However, according to the analysis in chapter 2, amplitudes of space-charge waves are affected by velocity perturbations via the $\alpha$-factor. When $\alpha > 0$, equation (2.39b) shows that the amplitude of the fast wave increases by $\alpha$ times, and that of the slow wave decreases by $\alpha$ times, while the peak-to-peak value of the energy modulation does not change. If amplitudes of initial energy perturbations are 15 eV for all cases above, we can derive that the value of $\alpha$-factor is 0.42, 0.17, 0.10, and 0.096 for case (a)-(d), respectively. Only in case (a), the effect of initial velocity perturbation is significantly big, but it still does not affect the comparison results in Table 3.5 and Figure 3.18. In addition, after considering the $\alpha$-factor in case (d), we still cannot explain the asymmetry pattern of the slow wave and fast wave from experimental observation. Furthermore, we only have one data point of energy profile in each case, which is not

adequate to analyze the effect of the initial velocity perturbation. Therefore, we will discuss more about the effect of $\alpha$-factor with more data points in the next section instead of this section.

## 3.4 Observation of space-charge waves in the upgraded LSE system

Lack of knowledge of initial conditions in previous experiments motivates us add new diagnostics in the upgraded LSE system. With more diagnostic tools installed, we are able to obtain more information for the evolution of longitudinal space-charge waves originated from density modulations at the beam source. For example, the evolution of the current perturbations can be measured at three different locations and the energy profiles can be measured both at the beginning and the end of the transportation line. So, we can repeat similar experiments presented in the previous section but with ability of obtaining more useful information on the initial conditions of beams.

In Sec. 3.4.1, we demonstrate an experimental method in measuring the sound speed, defined in equation (2.29), and discuss the related errors. Next, in the following Sec. 3.4.2, we present experimental results on the evolution of current modulations and energy modulations of different beams with matched radii of 4.9 mm in the long solenoid channel of the new system. Then, in Sec 3.4.3, we show some preliminary experimental results on the study of the relationship between the space-charge wave propagation and the matched beam radius.
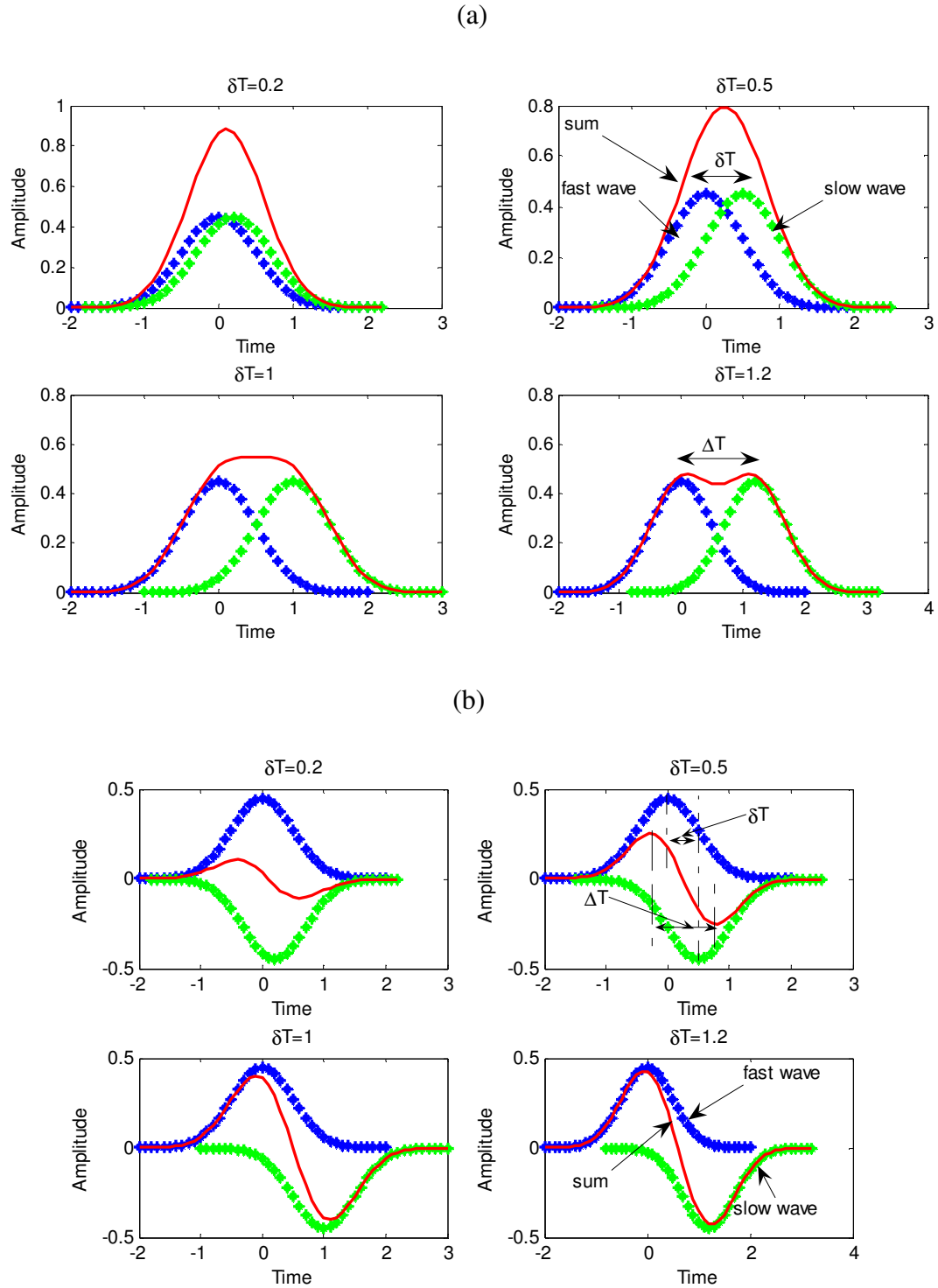
Figure 3.19: Illustration of the separation of the fast and slow waves. (a): in the current waveforms; (b): in the energy waveforms. blue stars, green stars, and red solid lines represent the fast waves, slow waves, and the sum of them respectively.

### 3.4.1 Separation of fast and slow waves

Before presenting the experimental results, it is necessary first to discuss the relationship between the sound speed $c_s$ and the peak-to-peak time difference in energy and current waveforms of the perturbed beams. Assuming a linear perturbation, the shape of the perturbation is preserved in both energy and current profiles. With a pure density initial perturbation, the current modulations will have the same polarity, but the energy will have the opposite polarity. If we define the time separation between the fast and slow waves by $\delta T = \dfrac{\Delta z}{v - c_s} - \dfrac{\Delta z}{v + c_s}$, where $v$ is beam velocity, and $\Delta z$ is the distance traveled by the beam, it will be easy to calculate the $c_s$ using the following formula with the assumption that sound speed is much smaller than the beam velocity:

$$c_s = \frac{\delta T}{2\Delta z} v^2 \qquad (3.4)$$

However, as we will discuss in the following section, the measured value of time separation $\Delta T$ is not always equal to $\delta T$. Assume that the fast and slow waves have a Gaussian distribution:

$$h(t) = \frac{1}{\sigma\sqrt{2\pi}} e^{(-\frac{t^2}{2\sigma^2})} \qquad (3.5)$$

where $\sigma = 0.5$. Then we can simulate the process of the separation of the fast and slow waves in both current and energy waveforms as shown in Figure 3.19. In current waveforms, with a small separation of the fast and slow wave, the sum expands longitudinally and changes in amplitude rather than showing two peaks. When the separation becomes significant compared to the width of the perturbation, two peaks

62

in current profiles appear and ΔT can be measured. Even though ΔT is smaller than δT initially, they are still close in value. Thus, one would expect a slightly smaller sound speed when replacing δT by ΔT in Equation (3.4). Due to opposite polarities of fast and slow waves, the evolution of space-charge waves in energy profiles is very different from that in current profiles. As shown in Figure 3.19(b), with a very short distance of propagation, the sum of the energy profiles of fast and slow waves shows two peaks that are separated by a significantly longer distance than δT. With further propagation of the waves, the two peaks of the energy perturbation increase in amplitude and move toward each other until the fast wave and slow wave are separated completely. As a result, the measurement of $c_s$ from the energy profile overestimates its value.

In summary, one can calculate sound speed by measuring the separation time of fast and slow waves. However, the result using the current profile tends to underestimate the real value, and that from the energy profile could overestimate the real value. We will describe these errors in the following experimental results.

### 3.4.2 Observation of space-charge waves in beams with 4.9 mm radii

By modulating the pulsed voltage between grid and cathode and changing the working condition of the gun, we managed to obtain different current profiles with both negative and positive initial perturbations. In this section, we describe the measurement results of the evolution of these perturbations by both taking the current profiles with three Bergoz current monitors and measuring the mean energy profiles at two chambers. As an important parameter characterizing the propagation of space-charge waves, sound speed $c_s$ is also measured from the separation time between the peaks of energy and current modulations using equation (3.4). In addition, we also compare the 1-d theoretical predictions with experimental results.

During the experiment, the AK gap of the electron gun was changed to 22 mm from the original 17.6 mm so that both negative and positive perturbations could be achieved by varying the bias voltage of the electron gun. In addition, there was no aperture plate in use. For all cases, the strengths of solenoids were chosen to match unperturbed beams into the long solenoid with a matched beam radius of 4.9 mm. When the bias voltage was set to 30 V and 35 V, the polarities of the current perturbations were found to be negative. On the other hand, when the bias voltage was increased to 48V and 52 V, positive perturbations were introduced to the main beam current.
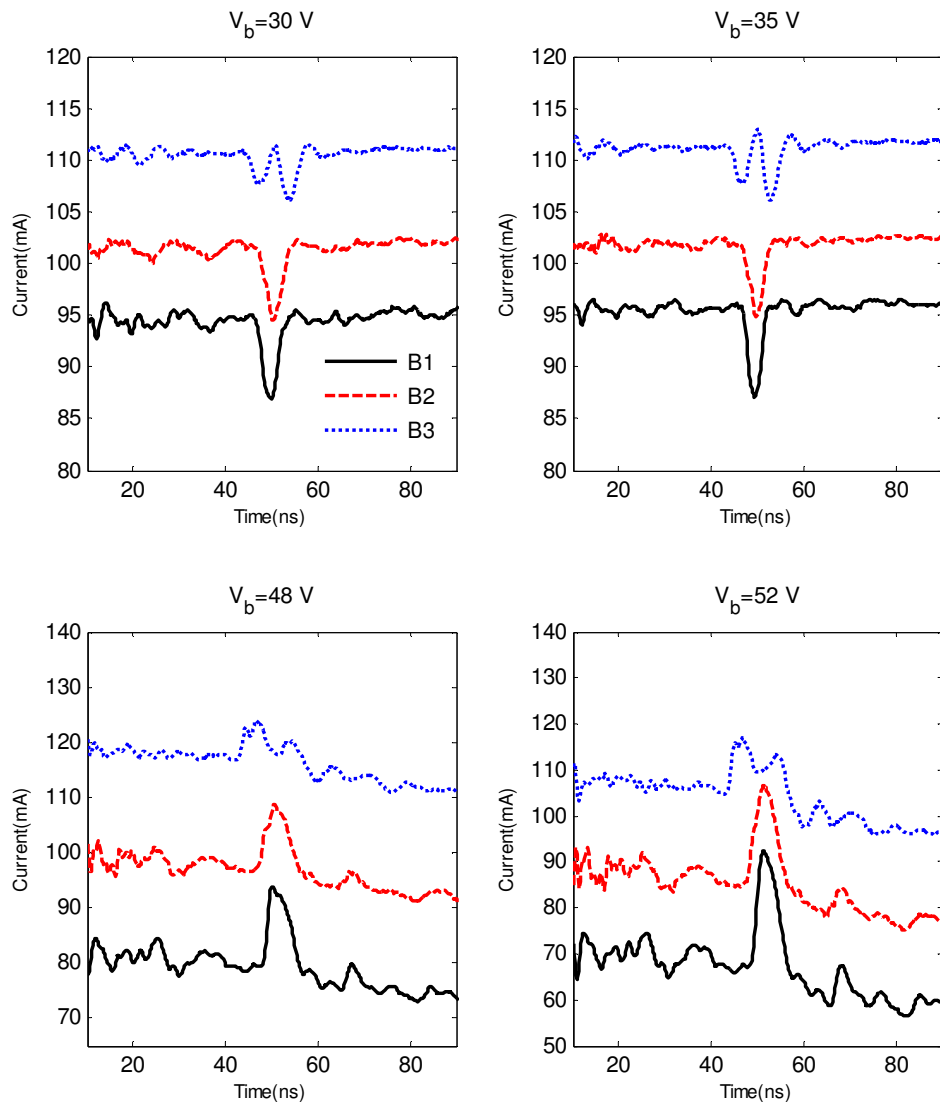
Figure 3.20: Current profiles of the 4.9 mm beam measured by three Bergoz current monitors when the bias voltage was set to 30 V, 35 V, 48 V, and 52 V, respectively. When $V_b$=30 V and 35 V, current profiles measured by B2 and B3 are shifted up by 10 mA and 20 mA, respectively. When $V_b$=48 V and 52 V, current profiles measured by B2 and B3 are shifted up by 20 mA and 40 mA respectively. The beam currents are represented by positive values.
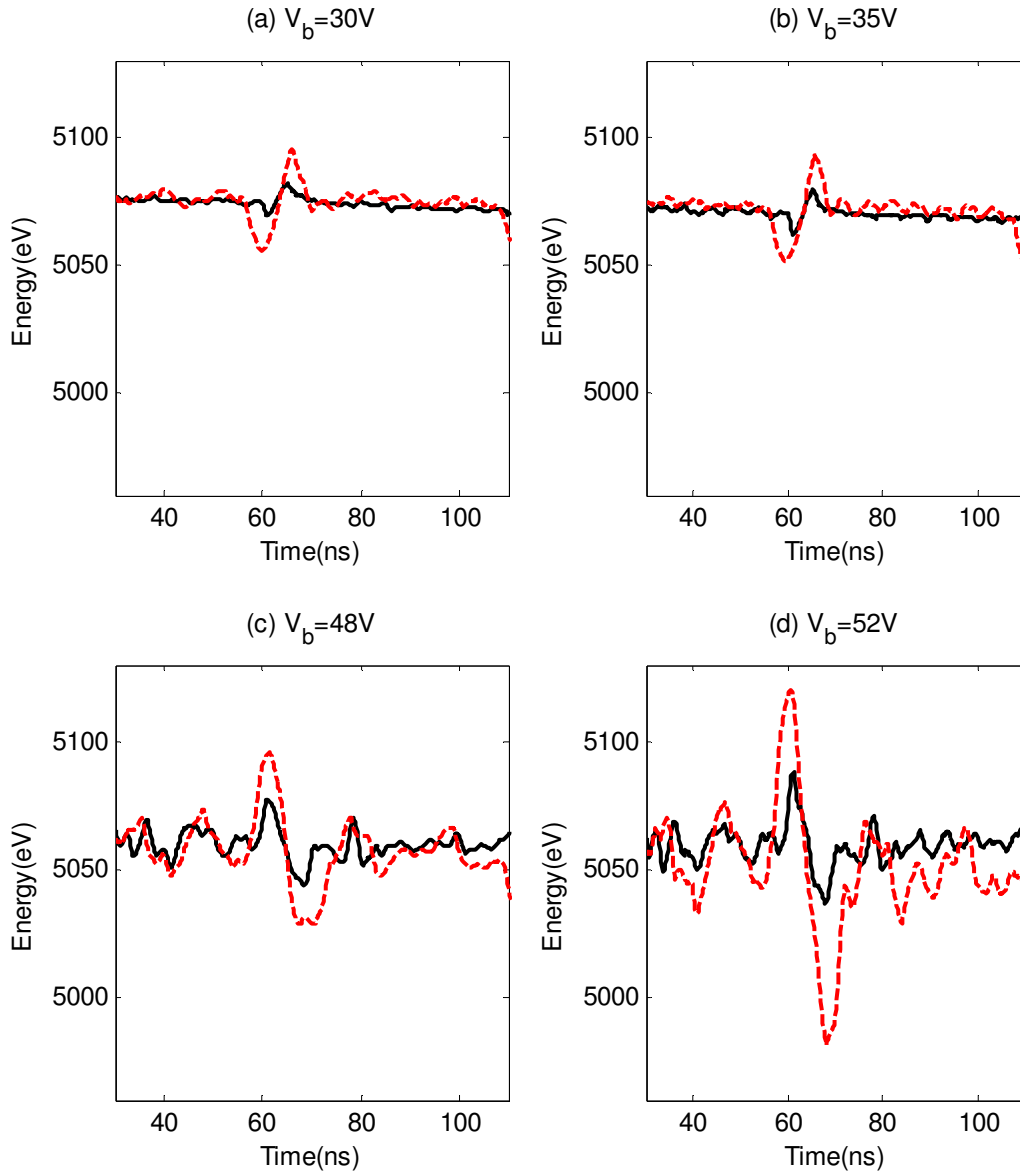
Figure 3.21: Mean energy profiles measured at LC1 (black solid lines) and LC2 (red dash lines) for 4.9 mm beams with different bias voltages.

Table 3.6: Parameters of current and energy profiles and calculation of sound speed

| | | $V_b=30$ V | $V_b=35V$ | $V_b=48V$ | $V_b=52V$ |
|---|---|---|---|---|---|
| Current Modulations | $I_1$ | -7.6 mA | -8.5 mA | 13.0 mA | 22.5 mA |
| | $I_0$ | 94.5 mA | 95.6 mA | 80.8 mA | 69.8 mA |
| | $\eta$ | -0.08 | -0.09 | 0.161 | 0.32 |
| | $c_s^{b3}$ | $2.76\times10^6$ m/s | $2.67\times10^6$ m/s | $3.52\times10^6$ m/s | $3.34\times10^6$ m/s |
| | $\Delta c_s^{b3}$ | -3.8% | -7.3% | 32.3% | 34.1% |
| Theory | $c_s^t$ | $2.87\times10^6$ m/s | $2.88\times10^6$ m/s | $2.66\times10^6$ m/s | $2.49\times10^6$ m/s |
| Energy Modulations | $E_0$ | 5075 eV | 5070 eV | 5057 eV | 5053 eV |
| | $\delta_1$ | 0.0026 | 0.0034 | 0.0067 | 0.01 |
| | $\delta_2$ | 0.0075 | 0.0081 | 0.011 | 0.027 |
| | $c_s^{e1}$ | $7.88\times10^6$ m/s | $8.70\times10^6$ m/s | $1.53\times10^7$ m/s | $1.44\times10^7$ m/s |
| | $\Delta c_s^{e1}$ | 174.6% | 202.1% | 475.2% | 478.3% |
| | $c_s^{e2}$ | $2.51\times10^6$ m/s | $2.44\times10^6$ m/s | $3.04\times10^6$ m/s | $2.88\times10^6$ m/s |
| | $\Delta c_s^{e2}$ | -12.5% | -15.3% | 14.3% | 15.7% |

Note:

$\delta_1= dE_1/ E_0$; $\delta_2= dE_2/ E_0$, where $dE_1$ and $dE_2$ represent peak to peak values of the energy perturbations in LC1 and LC2 , respectively.

$$\Delta c_s^x = \frac{c_s^x - c_s^t}{c_s^t}\times100\% \quad x = b3,\ e1,\ or\ e2.$$

All the current profiles measured by the three Bergoz current monitors (B1, B2, and B3), which are located 18.5 cm, 64 cm, and 207 cm downstream respectively, are presented in Figure 3.20, where the current profiles are zoomed in to enhance the visibility of perturbations near beam centers. By comparing the total charge of different current profiles, we found that even in the worst case, about 95.7% of the beam was transported through the whole beam line. In addition, most of the beam losses happened between B1 and B2, which indicates that the beam was well matched in the long solenoid channel. Therefore, the beam losses of all the four cases are low enough to be negligible to our experiment.

In Figure 3.21, mean energy profiles at LC1 and LC2 are plotted for these four different cases with different bias voltages. Unlike the current profiles in Figure 3.18, where two peaks are observed after the long solenoid channel, signatures of fast and slow waves are present in all energy profiles in Figure 3.21. For the beam with a positive initial current perturbation, we obtain a similar energy profile to the earlier experiment, with a positive fast wave and a negative slow wave. However, for beams with negative initial current perturbations, the energy profile consists of a negative polarity fast wave and a positive polarity slow wave.

In Table 3.6, we list some parameters such as the main beam current $I_0$, perturbation current $I_1$, initial current perturbation strength $\eta = I_1/I_0$, main beam energy $E_0$ etc. for reference. In addition, using equation (3.4), we derive sound speed from the current profiles measured by B3, the energy profiles in LC1 and LC2, and list them as $c_s^{b3}$, $c_s^{e1}$, and $c_s^{e2}$. Sound speeds calculated from equation (2.29) are also listed as $c_s^{t}$ for comparison. For all the four cases, values of $c_s^{e1}$ have extremely large

deviations from the theoretical calculation. This indicates that in LC1 fast and slow waves are still very close and the two peaks are moving toward each other, hence, as discussed in Sec 3.4.1, the measurement from energy profiles can overestimate the sound speed. When η is relatively small, i.e. the cases for the bias voltage of 30 V and 35 V, values of $c_s^{b3}$ are smaller than theoretical calculations by less than 8%. However, when the perturbation strength is increased further to more than 16%, the experimental results are more than 30% bigger than values derived from one dimensional cold fluid model. Absolute values of $\Delta c_s^{e2}$ are consistent for different cases with a range from 12.5% to 15.7%. However, experimental measurements underestimate the sound speed for beams with small perturbations and overestimated the sound speed for beams with larger perturbations. Although clear explanations for the inconsistency are not available now, nonlinear effects and complexity in the experiment compared with 1-D model may be relevant. Also, one should note that since all experimental measurements of sound speeds only use one data point, random errors could also contribute to the deviation.

To compare the experimental results of the evolution of current and energy perturbations with the 1-D theory in more detail, we need solve numerical solutions using equation (2.35). In order to study the effect of different initial velocity perturbations on the evolution of fast and slow waves, for each case we assume three different amplitudes of the energy perturbations: 0 eV, 15 eV, and 30 eV. If $E_1$ presents the amplitude of the energy perturbation, the velocity perturbation strength $\delta$ can be estimated by $\delta = \dfrac{E_1}{2E_0}$. Therefore, we can calculate the $\alpha$-factors using equation (2.38) for each case accordingly. In Table 3.7, we list the calculate results

for each case along with the initial current perturbation strength $\eta$ for comparison. From these calculated values of $\alpha$, we can see that the effect of velocity perturbation is more significant for cases with lower bias voltages, i.e. smaller current perturbations.

Table 3.7: Relationship between the initial energy perturbation and $\alpha$-factor for different beams

|  |  | $E_1=0$ |  | $E_1=15\ eV$ |  | $E_1=30\ eV$ |  |
| --- | --- | --- | --- | --- | --- | --- | --- |
|  | $\eta$ | $\delta$ | $\alpha$ | $\delta$ | $\alpha$ | $\delta$ | $\alpha$ |
| $V_b=30\ V$ | -0.08 | 0 | 0 | 0.0015 | -0.26 | 0.003 | -0.52 |
| $V_b=35\ V$ | -0.09 | 0 | 0 | 0.0015 | -0.225 | 0.003 | -0.45 |
| $V_b=48\ V$ | 0.161 | 0 | 0 | 0.0015 | 0.135 | 0.003 | 0.27 |
| $V_b=52\ V$ | 0.32 | 0 | 0 | 0.0015 | 0.075 | 0.003 | 0.15 |

For each case, we show current profiles of space-charge waves at the location of B3 calculated from the 1-D model in Figure 3.22 along with the experimental results. When $V_b=30\ V$ or $35V$, amplitudes of the current profiles of fast and slow waves are sensitive to the initial energy perturbations. If a zero initial energy modulation is assumed, the amplitude of the fast wave is larger than that of the slow wave, which is opposite to the experimental observation and 1-D results with a non-zero initial energy perturbation. This is can be explained by analyzing equation (2.39c). When the beam has pure initial current perturbation, the amplitude of the current profile of the fast wave is always larger than that of the slow wave due to a zero value of $\alpha$-

factor. But when $\alpha < 0$, in the current profile, the amplitude of the fast wave decreases by an amount of $\dfrac{\eta I_0 |\alpha|}{2}$, while that of the slow wave increases by the same amount. When $|\alpha|$ is significantly large, the amplitude of the slow wave exceeds that of the fast wave eventually. Thus from the comparison in Figure 3.22 (a) and (b), we can conclude that the initial velocity perturbation generated from the gun is not negligible for beams with smaller current perturbations. In addition, one can see that the 1-D results is closer to the experimental results by assuming $E_1$=15 eV than $E_1$=30 eV for both cases of $V_b$=30 V and 35V. The separation of the fast and slow waves for the cases with bias voltage of 30V and 35 V shows consistent results between the experiment and theory for all conditions of initial energy perturbations.

When $V_b$=48 V or 52V, the current profiles of fast and slow waves are relatively less sensitive to the initial condition of energy perturbations due to smaller values of the $\alpha$-factor. As indicated by equation (2.39c), the amplitude of the fast wave is always larger than that of the slow wave when $\alpha > 0$. The two peaks in the beam current waveforms of the beam with bias voltage of 48V and 52V separate further in the experiment than the theoretical prediction, which is consistent with the discrepancy of sound speed between experimental measurement and theoretical calculation shown in Table 3.6. Furthermore, by comparing the experimental results with the 1-D predictions, one can notice beam loss of the perturbations for both these two cases in experiment, especially for the case of $V_b$=52 V. We will discuss the effect of beam loss on the evolution of space-charge waves later.
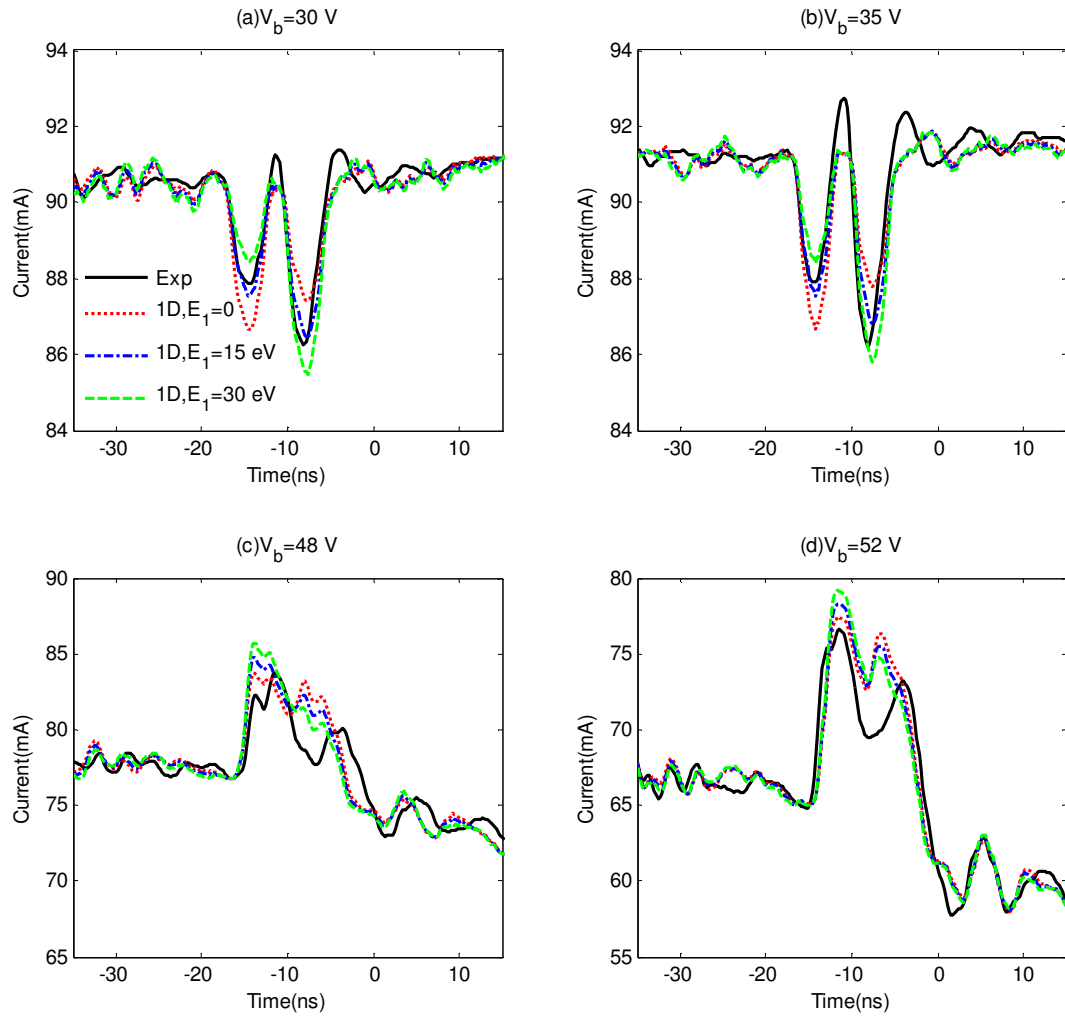
Figure 3.22: Current profiles at the location of B3 calculated from 1-D theory along with the experimental results (black solid lines). In the 1-D theory, the amplitude of initial energy perturbation is assumed to be 0 eV, 15 eV, and 30 eV, respectively. The beam currents are represented by positive values.

Figure 3.23 and 3.24 show the comparison of energy profiles at LC1 and LC2 obtained form the experiment and analytical calculations using 1-D theory with varied initial conditions of energy perturbations. Similar to the current profiles shown in Figure 3.22, amplitudes of energy modulations are sensitive to the change of initial energy modulations at LC1 and LC2 for both cases of $V_b=30$ $V$ and $35V$, while those for beams with $V_b=30$ $V$ and $35V$ are less sensitive.

In Figure 3.23, the 1-D theory predicts larger perturbation strengths for all these beams in LC1. In Figure 3.24, even though the separation time between peaks of energy modulations agrees between the experiment and theory, the amplitudes of energy modulations exhibit bigger discrepancy between theory and experiment than those in LC1. There are several possible reasons to explain the different results obtained from the peak separation time and perturbation strength: first, it is possible that the relatively large beam size in the matching section of the transportation line slows down the propagation of the space-charge waves and leads to smaller perturbation amplitudes; second, some other mechanism, such as nonlinear effects, beam loss, or transverse-longitudinal coupling, may contribute to limit the perturbation strength growth; finally, we are still not clear about the characterization of the transition response of the energy analyzer, which can increase the error of the measurement of the energy profiles.
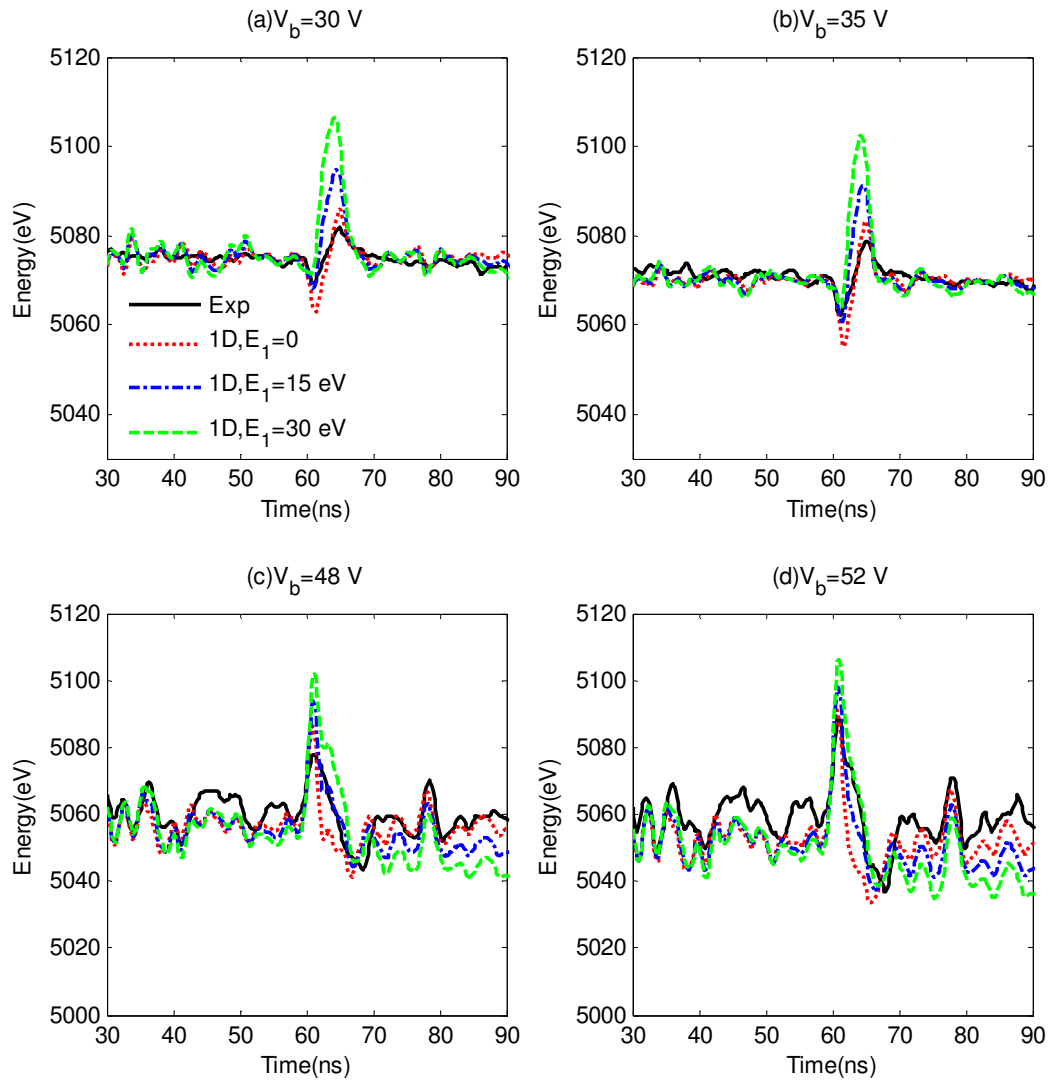
Figure 3.23: Energy profiles at LC1 calculated from 1-D theory along with the experimental results (black solid lines). In the 1-D theory, the amplitude of initial energy perturbation is assumed to be 0 eV, 15 eV, and 30 eV, respectively.
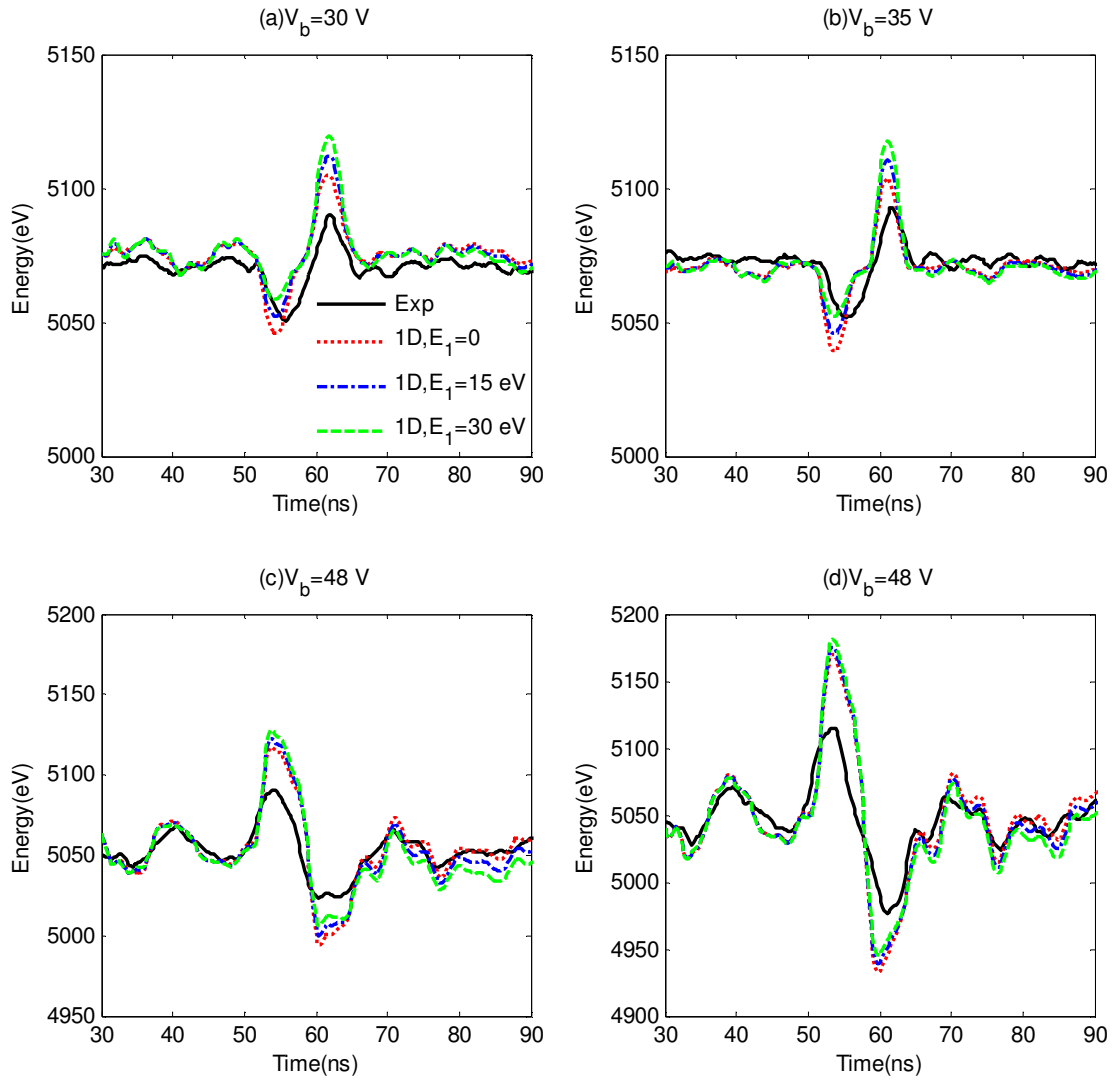
Figure 3.24: Energy profiles at LC2 calculated from 1-D theory along with the experimental results (black solid lines). In the 1-D theory, the amplitude of initial energy perturbation is assumed to be 0 eV, 15 eV, and 30 eV, respectively.

### 3.4.3 Observation of space-charge waves in beams with different radii

We have discussed in detail the accuracy of 1-D theory for modeling the evolution of space-charge waves. One thing that the 1-D model has simplified is the transverse complexity often existing in practice. The average beam radius is the only parameter correlating the transverse dynamics with the 1-D theory. In this section, we describe some preliminary experimental research in the relationship between matched beam radius and the propagation of space-charge waves.

When the beam was transported through the long solenoid channel, we changed the strengths of the solenoid magnets so that a matched beam radius of 4.9 mm, 3.9 mm, and 2.9 mm inside the long solenoid channel could be obtained. Then we repeated the experiment with these beams by measuring the current and energy profiles.
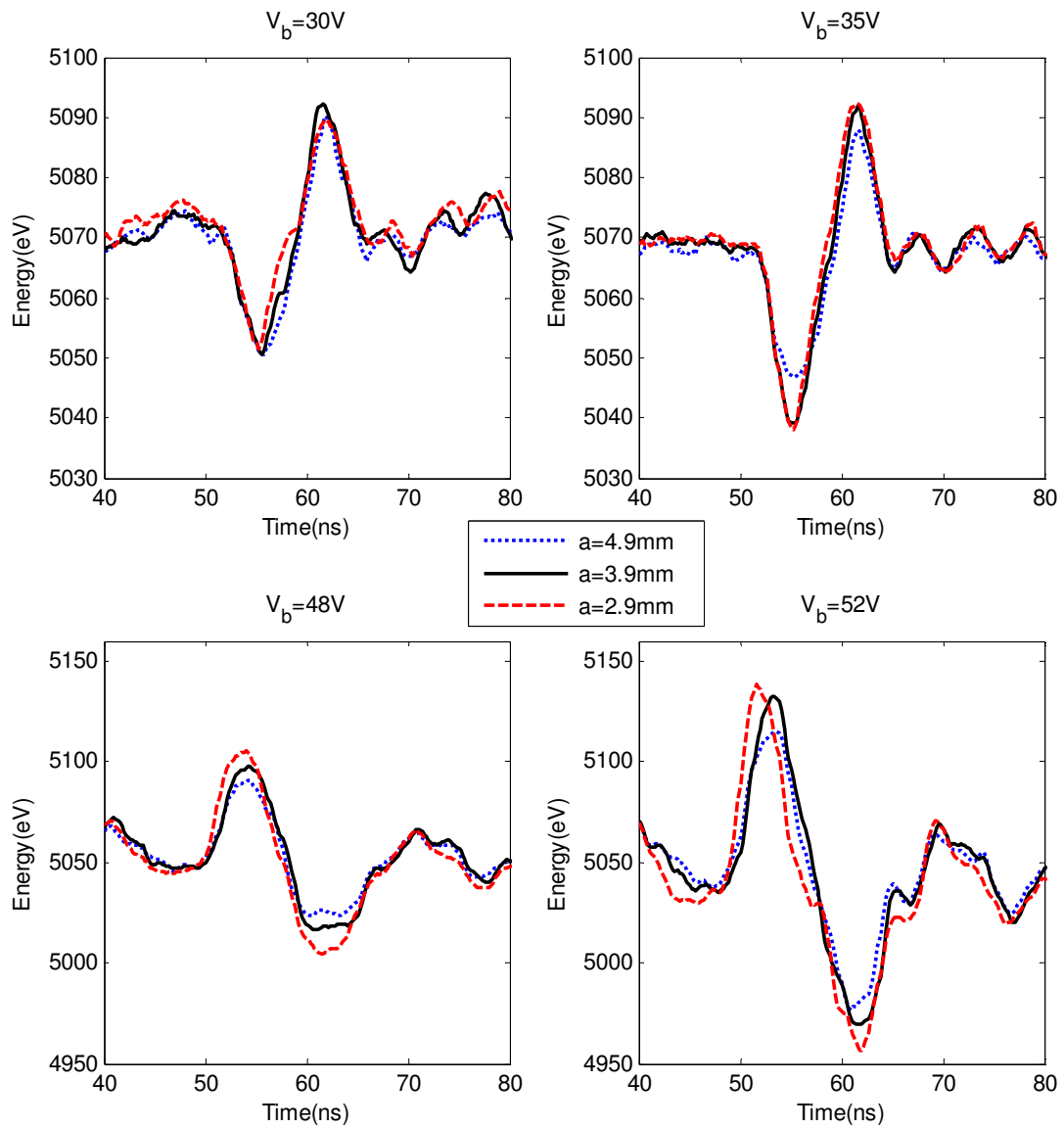
Figure 3.25: Energy profiles measured at LC2 for beams with different match radii (a=4.9 mm: blue dotted lines; a=3.9 mm: black solid lines; a=2.9 mm: red dash lines) in the long solenoid.
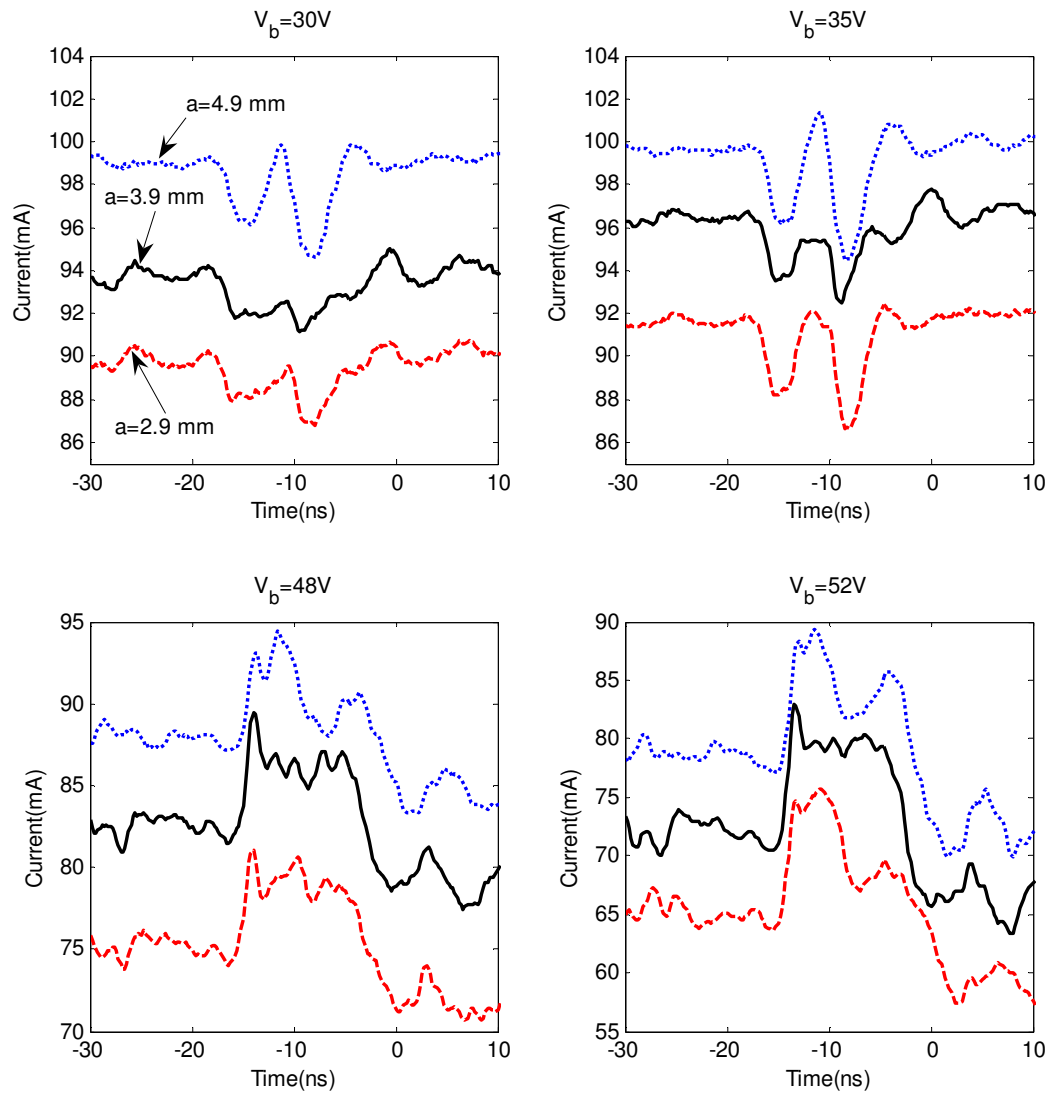
Figure 3.26: Current profiles measured by B3 for beams with different match radii
(a=4.9 mm: blue dotted lines; a=3.9 mm: black solid lines; a=2.9 mm: red dash lines)
in the long solenoid. All the current profiles have been zoomed in and rearranged
vertically for visibility of all curves. The beam currents are represented by positive
values.

Energy profiles and current profiles for different beam radii are shown in Figures 3.25 and 3.26, respectively. Because the strengths of matching solenoids did not vary much for beams with the same bias voltage, current profiles measured by B1 and B2 are almost identical for beams with different radii, but with the same bias voltage. Therefore, in Figure 3.26, we only show current profiles measured by B3.

Before discussing the experimental results, let's recall the 1-D theory and see what it predicts for the radius change. When the beam radius decreases, the g factor will increase. The definition of sound speed indicates that for the same type of particle beams with the same main beam energy, the sound speed is proportional to $(g\Lambda_0)^{1/2}$. Hence, a decrease of beam radius results in an increase of sound speed. On the other hand, equations (2.35b) and (2.35c) suggest that with larger sound speed, the fast and slow wave separate further for the same transportation distance and have larger amplitude as well.

In Figure 3.25, for the cases of $V_b$=30V and 35V, both the modulations amplitudes and peak-to peak separation time do not change much for different matched beam radii in the long solenoid channel. When the bias voltage was increased to 48 V and 52 V, both the perturbation strengths and the separation of fast and slow waves are relatively more sensitive to the radius change. For current profiles shown in Figure 3.26, one can observe more complicated changes in current perturbation profiles than the 1-D theory predicts when the beam radii are changed. For all cases, the decrease of beam radius breaks the preserved shape of the initial single perturbation. In particular, for the higher bias voltages case, multiple oscillations occur inside the perturbation. As a result, it is very hard to estimate the

difference of sound speed from the amplitude and peak-to-peak separation time in current profiles of space-charge waves.

We are not very sure if this indicates the existence of the coupling between longitudinal and transverse dynamics. Here, we only showed some preliminary measurements to introduce this topic. To further investigate it, it would be helpful to carry out more measurements on the transverse behavior of perturbed beams.

## 3.5 Summary

We conducted the first high resolution measurement on energy profiles of space-charge waves in the LSE system before upgrade. Further measurements have also been conducted in the new system with more diagnostics providing more details of the evolution of space-charge waves. All these results have been compared with 1-D theory and they show that 1-D theory is a good model for predict the general trends of the evolution of the space-charge waves.

However, some discrepancies between the 1-D model and the experimental results indicate the complexity of the evolution of space-charge waves. To investigate the cause of these discrepancies, the simple 1-D model is inadequate to include more complicated issues such as envelope oscillations, mismatch of the beam radius, and other nonlinear effects.

From the preliminary results shown in Sec 3.4.3, the dependence of space-charge waves on transverse beam radius is beyond the prediction of 1-D theory and still required further investigation.

# Chapter 4  Fast imaging of the longitudinal perturbations

In order to better understand the longitudinal dynamics of the perturbed space-charge dominated beam and probe the correlations between transverse and longitudinal time-resolved distributions, we discuss experimental measurements of the transverse distributions in this chapter. Because the width of the perturbation is about 10 ns, which is small compared to the length of the whole beam, which is typically 100 ns wide, we needed to develop a technique that capture the beam images in a time interval as small as several nanoseconds.

We have three different imagers for measuring transverse distributions of electron beams: a P43 screen, an optical transition radiation (OTR) imager, and a fast phosphor screen. The P43 screen has the advantage of high damage tolerance of charge densities and high intensity of light output. But it has an intrinsic 1.3 ms decay time, which is very large compared with our typical beam length, i.e. 100 ns. Therefore, the P43 screen is used for fully time-integrated imaging of our beams. As will be discussed in detail later, the light generated from the OTR imager, a silicon based aluminum mirror, is prompt, but the intensity is very low because of the low energy of our beams. Thus, to achieve clear time-sliced transverse images of beams with OTR, a large number of frame integrations for different beam pulses is required, which leads to a long data acquisition time. The fast phosphor screen, which has a decay time of about 3 ns, is a new diagnostic tool introduced to research in beam physics for the first time by us. We have demonstrated experimentally that it is suitable for beam diagnostic purposes. Furthermore, the light output of the fast

phosphor is sufficient to perform progressive time-resolved imaging. The robustness and practical lifetime of the fast screen still requires further investigation.

In this chapter, we show the first time-resolved photos of different electron beams from each of the OTR screen (Sec. 4.1) and the fast phosphor screen (Sec. 4.2). A brief summary ends this chapter in Sec. 4.3.

## 4.1 Fast imaging using the OTR light

In this section, we present the time-resolved transverse measurement of the perturbation using an OTR imager. Since OTR screens were first installed in diagnostic chambers in the University of Maryland Electron Ring (UMER), this experiment was carried out using the UMER beam. In the following, the UMER system is briefly introduced first (Sec. 4.1.1). It is followed by an overview of the application of OTR as a diagnostic tool for relativistic beams (Sec. 4.1.2). Next, the OTR diagnostics at UMER are described succinctly (Sec. 4.1.3). Finally, we discuss experimental results obtained from the fast imaging using the OTR screen.

### 4.1.1 UMER system

As shown in Figure 4.1, the UMER, designed for transport studies of space-charge dominated beams in a strong focusing lattice, is a small scale electron storage ring with a comprehensive set of beam diagnostic tools [46]. The design parameters of the UMER can be found in Table 4.1.

Table 4.1: General parameters of the University of Maryland Electron Ring

| | |
|---|---|
| Energy | 10 keV |
| Current | ≤100 mA |
| Generalized Perveance | 1.5e-3 |
| Rms emittance, 4xrms, norm | ≤3μm |
| Pulse length | 50-100ns |
| Circumference | 11.52m |
| Pulse Rep. rate | 60 Hz |
| Mean beam radius | <1cm |
| FODO period | 0.32m |
| Zero-current Phase advance, $\sigma 0$ | 76° |
| Zero-current Betatron tune,$\upsilon 0$ | 7.6 |
| Tune depression | ≥0.2 |
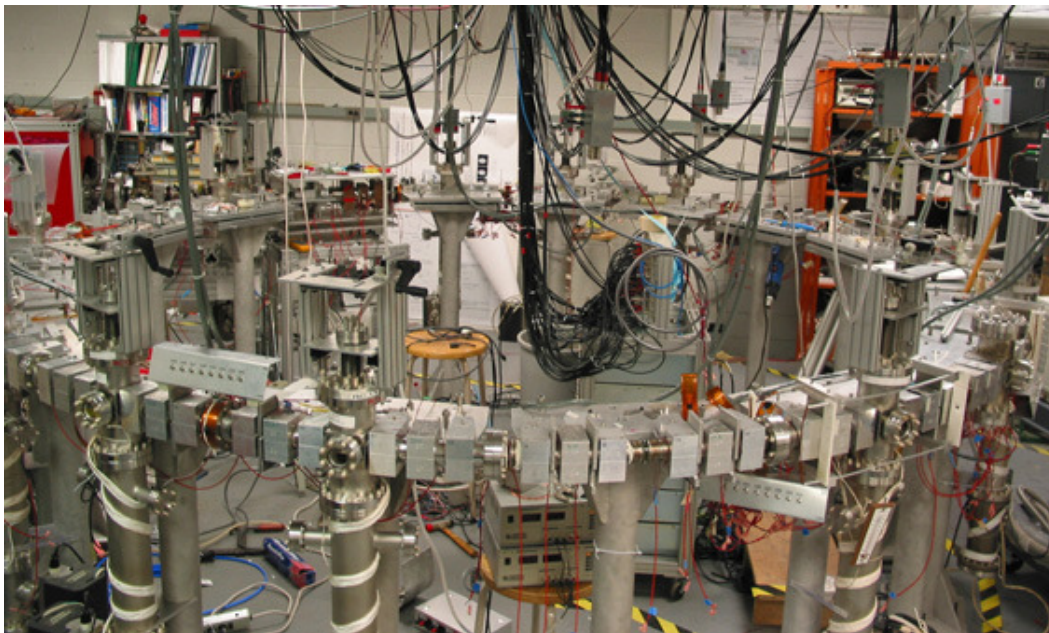


Figure 4.1: The photo of the University of Maryland Electron Ring (UMER).

A gridded, variable perveance Pierce-type electron gun is used as the beam source. The structure of this electron gun is very similar to the one in the LSE system, so by using the same methods applied in the LSE electron gun, we can generate initial current perturbation from the electron gun by modulating the gun pulse voltage. In the injection section, a short solenoid, 6 quadrupoles, 5 horizontal/vertical magnetic steers, and Helmholtz coils for earth's magnetic field compensation are used to match the beam. After the matching line, two large aperture magnetic quadrupoles, a pulsed dipole, and two steering magnets can inject the beam into the ring sections and recirculate the beam. The ring sections of the UMER consist of 36 alternating-focusing (FODO) periods over an 11.5 m circumference. Each FODO period contains a 10 degree bending dipole and two quadrupole magnets. As indicated in Figure 4.2, one unique feature of the UMER magnets are their printed circuit design which benefit from the relative low field strength required by the UMER beam.

To allow detailed comparison between theory and experiment, UMER has a comprehensive set of beam diagnostics. There are two diagnostic chambers in the injection line and 13 diagnostic chambers along the ring. Inside these diagnostic chambers, capacitive beam position monitors are used to determine the beam centroid and current; phosphor screens are also installed for taking the transverse images of the beam. In addition, a fast (200 ps rise time) Bergoz current monitor is installed right after the first injection chamber (IC1) in order to monitor the longitudinal current profile of the beam.
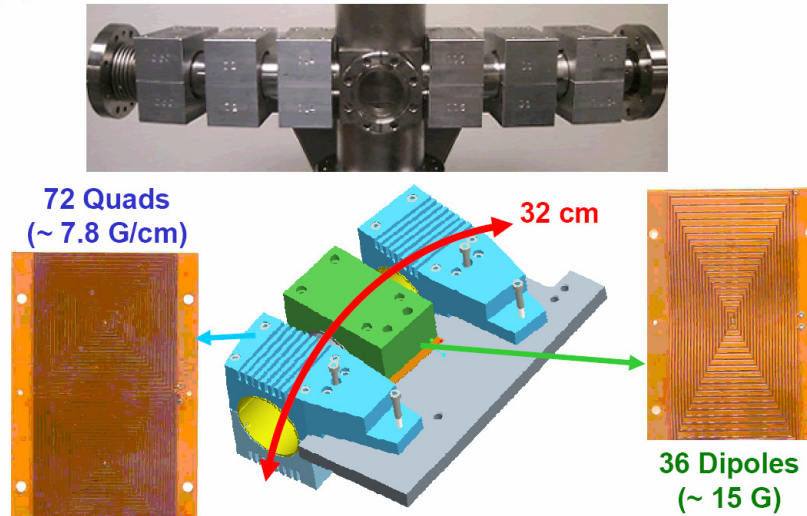
Figure 4.2: Components of one UMER ring lattice. Top: the assembling of one 64 cm section in the ring including a diagnostic chamber. Bottom: a printed circuit quadrupole and a printed circuit dipole.

## 4.1.2 OTR as a diagnostic tool for relativistic beams

When a charged particle beam with a constant velocity passes through two different mediums with different dielectric constant, for example, from the vacuum to a metal plate, the fields generated from the particle beam will change quickly and some of the field energy is converted to optical transition radiation (OTR) [47]. This process can be described by a collapsing dipole. As the charge particle beam approaches the metal surface, the image charge is also approaching the metal surface. When it reaches the surface and stops suddenly, radiation is generated.

The first theoretical prediction of the OTR was made by Ginsburg and Frank in 1945 [48]. Later, in 1959, Goldsmith and Jelley observed the OTR from high energy protons and confirmed the existence of the OTR [49]. The first work utilizing OTR as

beam diagnostic tool was made in 1979s by Wartski, who demonstrated that the OTR image can be used to measure beam intensity profiles, and the angular distribution of the OTR pattern can be used to measure the energy of a highly relativistic beam [50]. Since then, OTR has been widely used for measurement of the beam energy, divergence and emittance of the high energy beams [51]. For this application, a thin foil is generally used to let the beam pass though. As a result, both backward OTR, which is generated when the beam enter the metal from the vacuum and the forward OTR, which is generated when the beam enter the vacuum from the metal foil. The magnitude and angular distribution of them are the same. However, the center of backward OTR intensity is in the direction of specular reflection of the incident beam and that of the forward OTR is consistent with the direction of the beam propagation [52]. In order to measure the beam divergence, an OTR interferometer generally consists of two parallel thin metal foils, oriented 45 degree with respect to the incident beam. When the distance between these two foils is comparable with the vacuum coherent length, the visibility of the interference pattern between the forward OTR from the first foil and the backward OTR from the second foil can be used to calculate the rms beam divergence [53].

### 4.1.3 OTR diagnostics at UMER

Even though the OTR has become a diagnostic tool for highly relativistic beams for a long time, it has not been widely used for low energy beams because of the low light yield and large angular distribution of the radiation pattern. Because of the need for time resolved imaging of the UMER beam, a fast imaging technique using the OTR radiation has been recently developed and implemented in UMER. The OTR

86

imager is a rotatable silicon screen which has a 0.1 μm Al coating on one side and a P43 phosphor deposited on the other side. It has been verified experimentally that OTR observed from the OTR imager can be used for diagnostic purpose for the 10 keV UMER electron beam [54].

The angular distribution of OTR obtained from an electron incident on a perfect conductor can be described as the following equation [55]:

$$\frac{d^2W}{d\omega d\Omega} = \frac{e^2\beta^2}{4\pi^2 c}\left(\frac{\sin(\theta-2\psi)}{1+\beta\cos(\theta-2\psi)} + \frac{\sin\theta}{1+\beta\cos\theta}\right)^2 \tag{4.1}$$

where W is the energy of the radiation, ω is the angular frequency of the radiation, Ω is the solid angle, e is the electron charge, β is the velocity of the electron divided by the speed of light, θ is the observation angle in the horizontal plane formed by the velocity of the electron *V* and n, the normal to the screen, ψ is the angle between *V* and n. The orientation of the OTR imager relative to the incident beam and the field of view angle of the OTR light is illustrated in the Figure 4.3. During the experiment, we choose ψ=35°. This angle is determined by the compromise between maximizing the light intensity inside the field of view and avoiding the refection of the cathode light by the mirror. One should also note that since the beam energy is very low, the electron beam has been fully stopped by the OTR imager. As a result, there is no forward transition radiation in this case and the light observed is totally from the backward radiation. The locations of the OTR stations at UMER and the measurement system setup are illustrated in Figure 4.4. The OTR imagers are installed in two diagnostic chambers: IC1, about 36 cm away from the gun aperture; and the eighth ring chamber (RC8), about 6.4 m downstream.
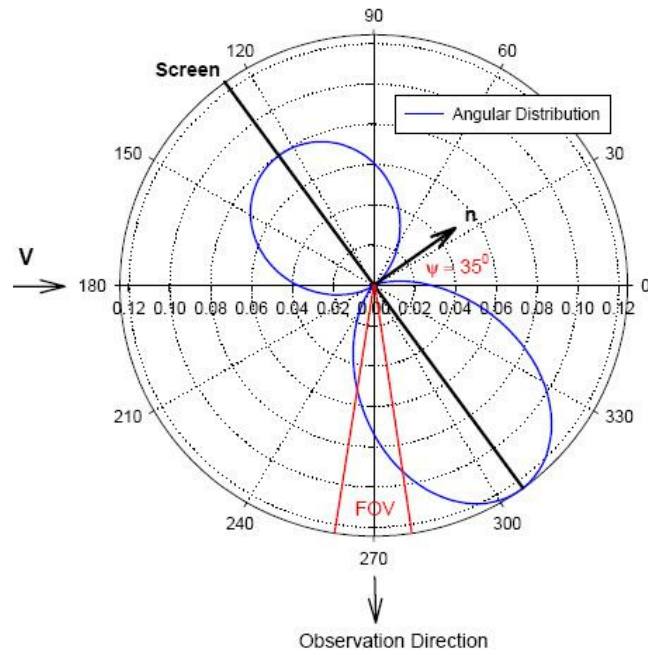
Figure 4.3: Angular distribution of the OTR light emitted from the OTR screen in

UMER [54]
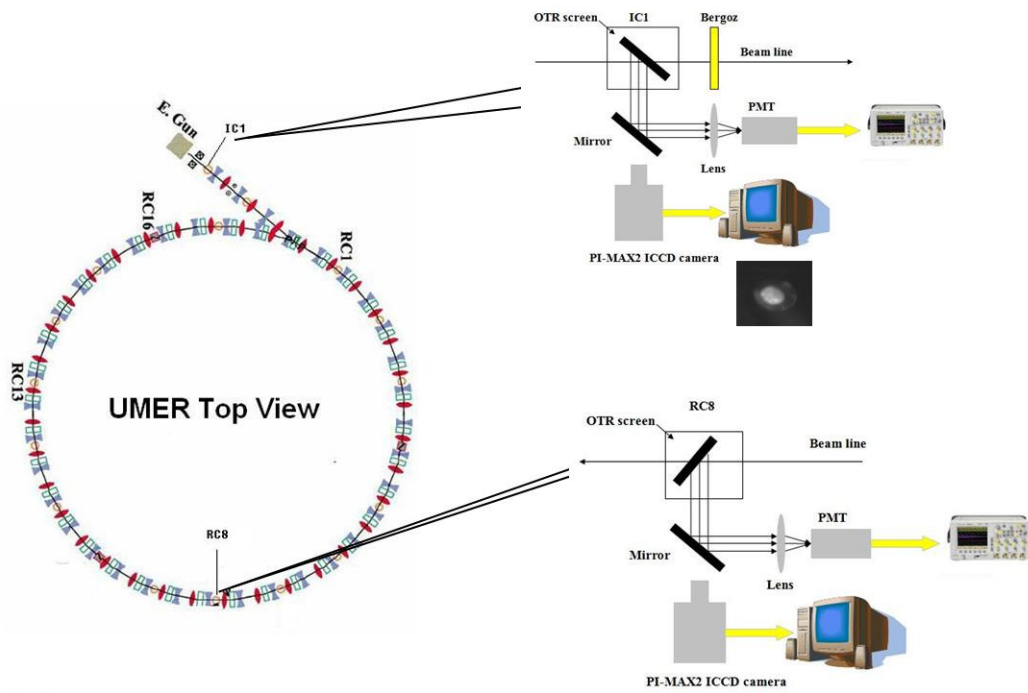


Figure 4.4: The OTR experiment setup in UMER.

With the advantage of the prompt (~fs) time response of OTR light, one can obtain time sliced images of the beam using a high-sensitivity intensified gated camera with multiple frame-integration. In our experiment, we view the OTR screen installed in IC1 with a fast (1 ns rise time) Hamamatsu photomultiplier tube (PMT) with 1 ns response time to acquire the optical signal of the OTR light so that we can compare it with the current signal from Bergoz current monitor. In RC8, a gated 16-bit PIMAX2 ICCD camera with a minimum gate width of 3 ns is used to capture the time resolved beam images. The gate pulse can be programmed and controlled by a computer. By carefully synchronizing the gate pulse with the beam current signal, sliced images for different parts of the beam can be obtained. Since the beam from the UMER gun is relatively stable and reproducible, in order to achieve a good signal to noise ratio for each sliced image, multiple frames were applied for each exposure of the ICCD camera.

## 4.1.4 Experimental results

To generate initial current modulation in the UMER beam, we used the electrical method by connecting a cable to the pulse generation circuit of the electron gun. For the UMER electron gun, when the bias voltage is lower than 45 volts, the beam current has a single positive perturbation which is consistent with the shape of the modulated pulse voltage. When the bias voltage is increased further, the single perturbation on the current waveform becomes negative as discussed earlier in chapter 3. A bias voltage of 45 V was selected to drive the electron gun in the amplification mode and keep the perturbation amplitude big enough for observing the

correlation between the transverse and longitudinal dynamics. In addition, a gun aperture was in use and the unperturbed beam current was about 25 mA.

When the bias voltage is set to 45 volts, the current waveforms of both the perturbed and unperturbed beam measured by Bergoz are shown in Figure 4.5, in which current profiles measured by the photo multiplier tube are also plotted for comparison. The current profiles derived from both methods agree very well except that the PMT signal has a relatively slower response to the perturbation compared to the Bergoz signal. This is mainly due to the response time of the PMT is about 1 ns, while the typical response time of Bergoz current monitor is 200ps. The measured perturbation width is about 10 ns for both methods. Hence, in terms of response time, the OTR signal is more than enough for probing the transverse details inside the perturbation.
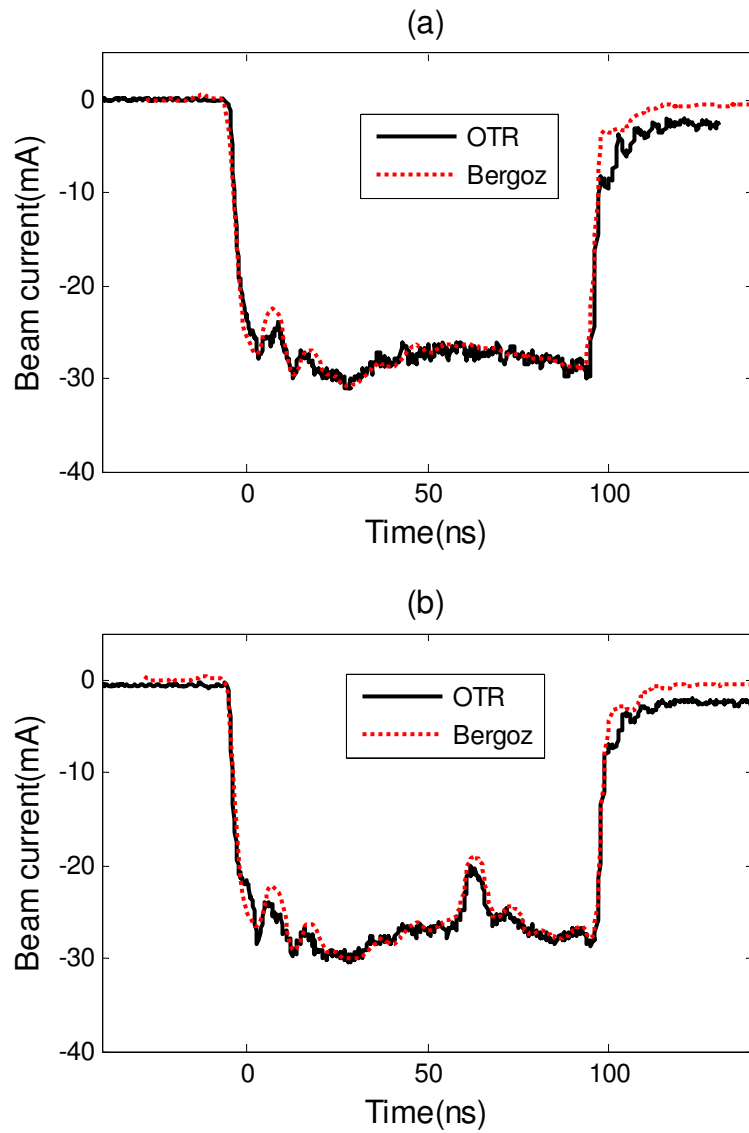
Figure 4.5: Perturbed and unperturbed beam current profiles in UMER (a) without perturbation measured by PMT at IC1 (black solid line) and Bergoz current monitor (red dotted line), and (b) with perturbation measured by PMT at IC1 (black solid line) and Bergoz current monitor (red dotted line).
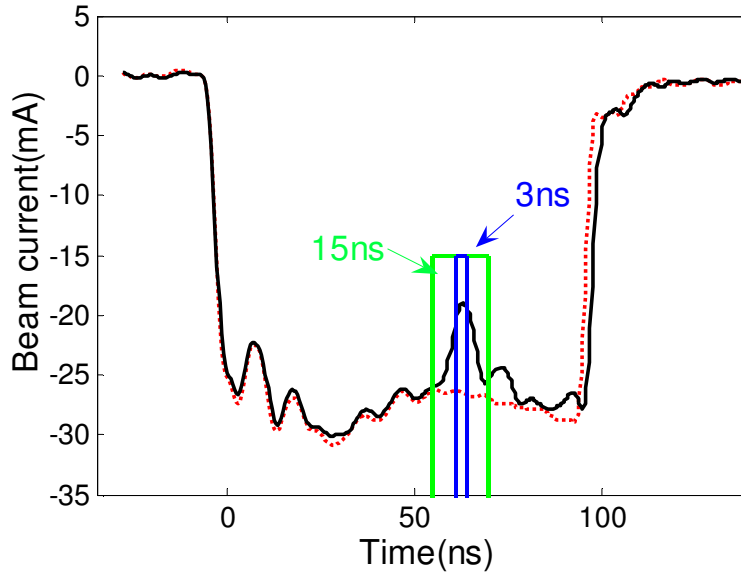
Figure 4.6: Illustration of the position and width of the gate window. The 15-ns gate window covers the whole perturbation, while the 3-ns gate window is inside the perturbation.

Since later the OTR screen in IC1 was contaminated during the experiment, we were not able to carry out time-resolved imaging there. In chamber RC8 of UMER, we tried various gate widths of the ICCD camera in taking the sliced images of the perturbation shown in Figure 4.5. Figure 4.6 shows positions and widths of two different gate windows. A 15 ns wide gate with 50,000 frame integrations was used first to cover the whole perturbation which is about 10 ns wide. Then, a smaller window of 3ns was applied inside the perturbation. As shown in Figure 4.7 (a) and 4.7 (b), only a subtle difference in the transverse distributions can be observed for the beam with and without perturbation for the 15-ns sliced images. This indicated that 15 ns is too long an integration time to reflect the details in the change of transverse distributions resulted from the longitudinal perturbation.

The measurement results are quite interesting for the 3-ns sliced images as shown in Figure 4.7 (c) and 4.7 (d), which exhibit a substantial change when the perturbation is turned off. Transversely the beam images for both cases include a halo and a beam core. But when the perturbation is added, the size of the beam core becomes smaller and the distribution of the beam core is less uniform than that of the unperturbed beam. Another interesting observation is that the perturbation affects the size and profile of the beam core significantly, but not the halo. The halo remained the same for both cases. Since the 3 ns gate window cuts down a lot of light intensity from the OTR which is not quite intense for low energy beam, for the photos shown in Figure 4.7 (c) or (d), frame integrations as many as 170,000 (47 minutes for the UMER beam operating at 60Hz) were used in order to get a clear image.
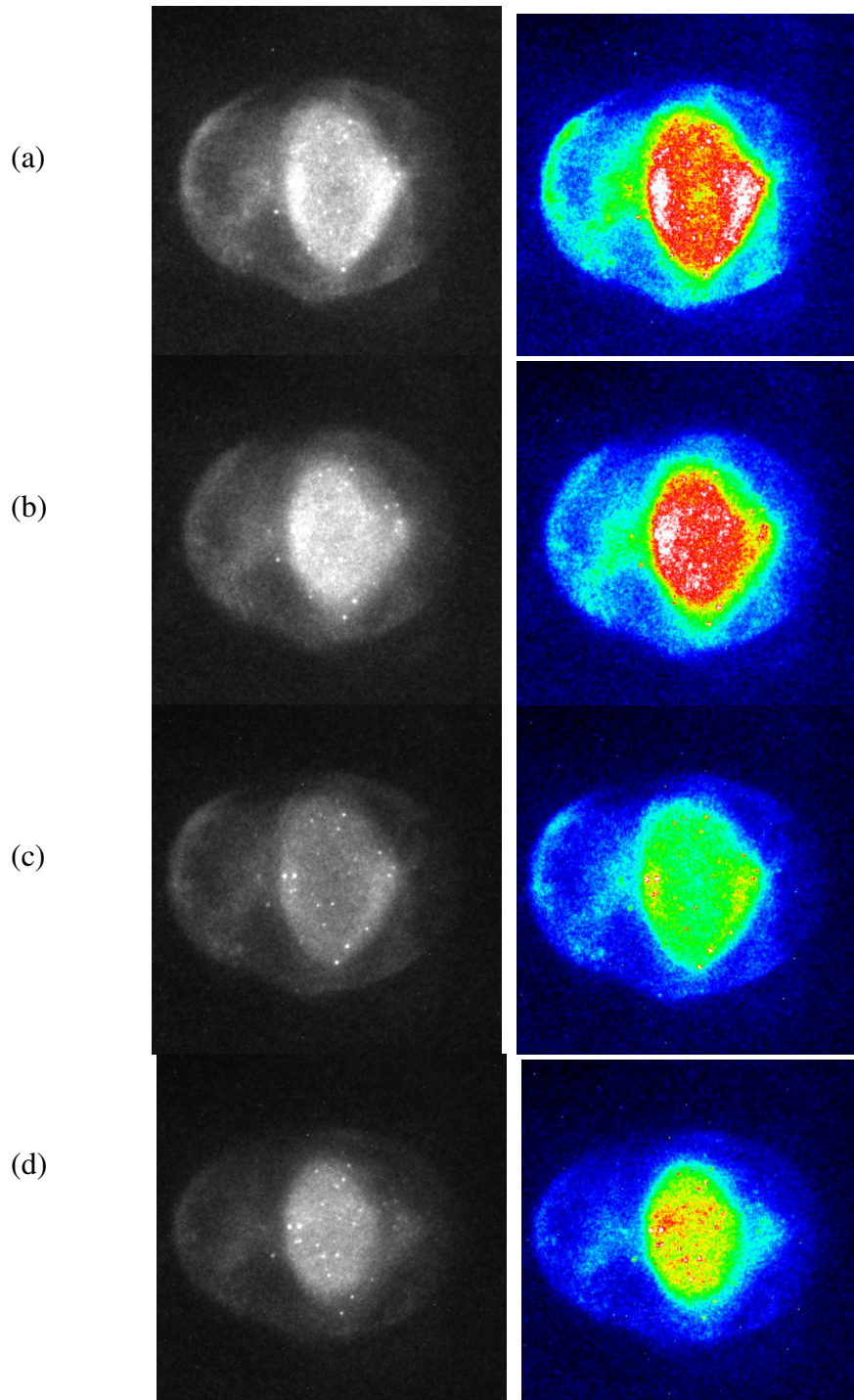
Figure 4.7: Sliced images of the perturbed and unperturbed beams at RC8 (left: grayscale; right: color coded). (a) 15 ns without perturbation; (b) 15 ns with perturbation; (c) 3 ns without perturbation; (d) 3 ns with perturbation.

To confirm that the 3-ns sliced images taken from the OTR are useful, we also tested the beam stability by taking three whole beam images during a two-hour interval. The results are shown in Figure 4.8 and indicate that the UMER beam is very stable and repeatable for a long term. Therefore, the integrated image for 170,000 pulses can still provide us relatively accurate information of the beam's transverse behavior that affected by the perturbation. More importantly, this is the first comparison of transverse profiles of a beam with and without a deliberate longitudinal perturbation.
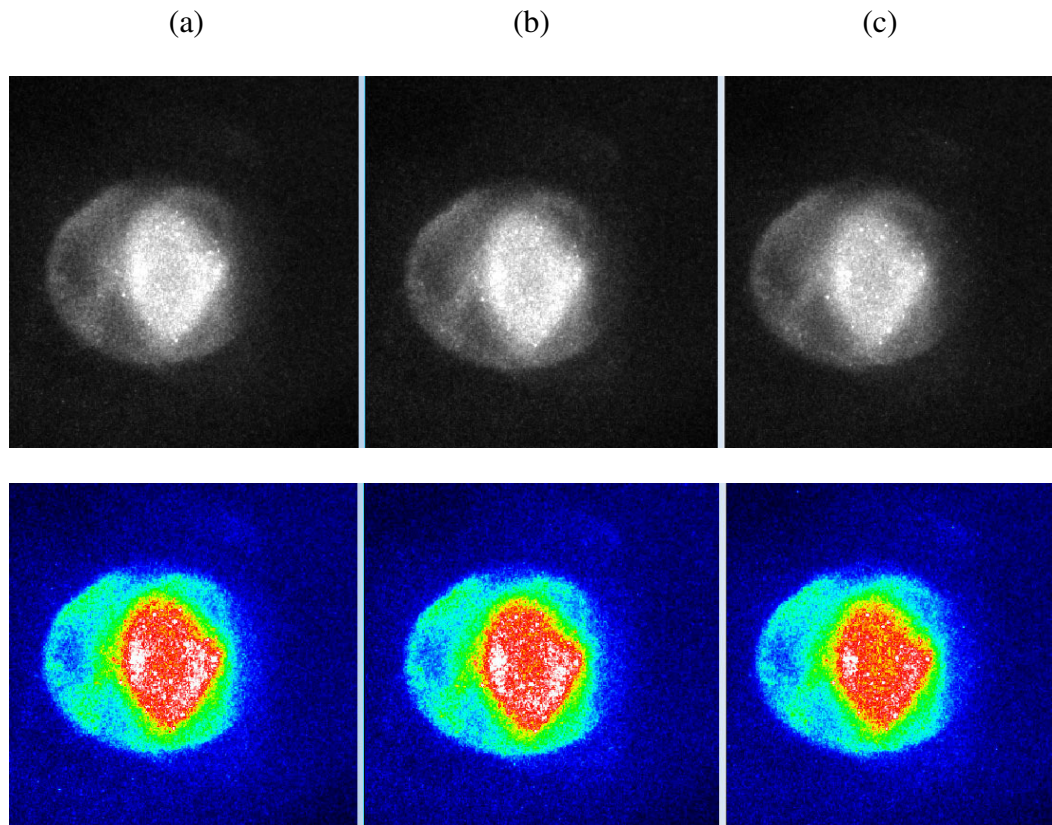


Figure 4.8: Beam images at RC8 obtained from the OTR light at different time. (a) the first image (top: grayscale; bottom: color coded) (b) 30 minuets later (top: grayscale; bottom: color coded) (c) 2 hours later (top: grayscale; bottom: color coded) All the photos were taken using the same camera settings.

## 4.2 Fast imaging using a fast phosphor screen

The fast phosphor screen is composed of a ZnO:Ga deposited quartz plate with thin transparent aluminum coating. The peak light output of this screen occurs at a wavelength of 390 nm, and the beam image is visible to the unaided eye. Since there is no previous experimental testing data of the maximum current density current tolerance, normal life time or spatial resolution available to us from the commercial manufacture, we need test the screen experimentally before utilizing it for beam diagnostics.

In the following, we first briefly describe the experimental setup for the fast imaging experimental using a fast phosphor screen in Sec 4.2.1. Then, experimental results of parabolic beams are discussed thoroughly in Sec 4.2.2. Next, in Sec. 4.2.3, we apply this fast imaging technique to rectangular beams with both negative and positive perturbations. Finally, we present the longitudinal energy profiles of the beams we have measured.

### 4.2.1 Experimental setup

The fast phosphor screen was first installed in the LSE system for testing. As shown in the Figure 4.9 (a), the fast imaging measurement was carried out at the front part of the LSE system. The screen is installed in the bracket under the high resolution energy analyzer in LC1.

During the experiment, beams with different current profiles but the same nominal energy of 5 keV are generated from the electron gun. From the gun aperture to the chamber, the beam is focused by S1 and S2, between which a Bergoz current monitor is used to monitor current profiles. Similar to the OTR experiment in UMER,

96

the PMT and the ICCD camera are used for obtaining the optical signal emitted by the fast phosphor screen in LC1. The setup of the control and data acquisition system is illustrated in Figure 4.9 (b), where a computer is used to control the PIMAX 2 ICCD camera through a digital controller.

(a)



(b)
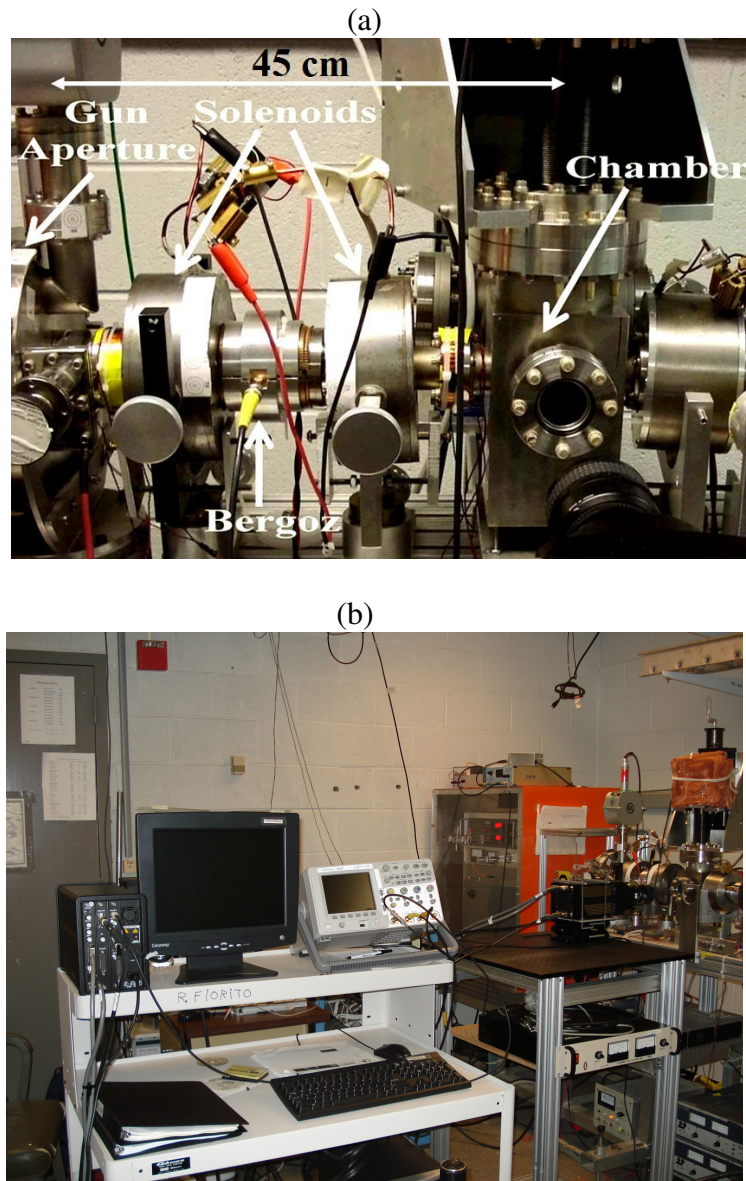


Figure 4.9: System setup for the fast imaging experiment in LSE. (a) the beam line used for fast imaging in LSE system; (b) set up of the data acquisition system of fast imaging experiment in LSE.

**4.2.2 Time resolved measurement on the parabolic shape beam**

By connecting a low-pass filter to the transmission cable of the pulse voltage, the pulse voltage can be modified to a nearly parabolic shape. When the gun is working in amplification mode, the beam pulse will have a similar shape. Since the longitudinal current of the parabolic beam is not constant, it is a very good candidate to test the response characteristics of the fast phosphor screen. At the same time, it will also be interesting to see the correlation between the transverse and longitudinal dynamics of the parabolic beam. An aperture with a radius of 1.6 mm is applied to reduce the beam current since we do not know the charge collection limit of this screen. By changing the bias voltage of the electron gun, beam current profiles with different peak current values can be generated. In this experiment, we used two different beam profiles with the peak current of 23mA and 13 mA respectively. We can also achieve moderate current by increasing the bias voltage without applying an aperture. However, in this case we need operate the gun close to the cut off mode, where the beam is relatively unstable in practice.
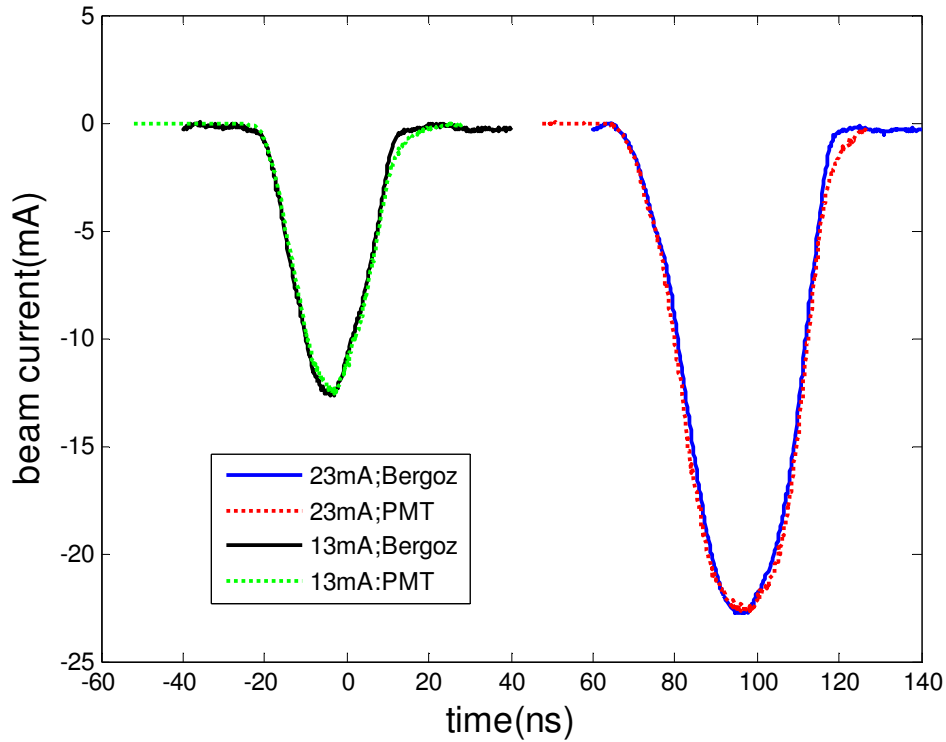
Figure 4.10: Parabolic shape beam current profiles measured by Bergoz current monitor (blue and black solid lines) and PMT (red and green dotted lines).

As mentioned earlier in the OTR experiment, the quickest way to measure the response time and charge linearity of the fast phosphor screen is to compare the beam current profile, which is measured by capturing the light signal from the screen with a PMT, with that measured by a Bergoz current monitor. The comparison has been illustrated in the Figure 4.10. Since the bias voltage for the 13 mA parabolic beam is higher than that of the 23 mA parabolic beam, the width, defined as 20%-to-20% of the maximum amplitude, of the former is 27.4 ns, smaller than that of the latter one, i.e. 41.2 ns. For both beams, the results indicate that the light signal from the phosphor responds nearly as fast as the Bergoz signal except for a relatively slow tail from 20% of the maximum amplitude to zero. Furthermore, the good fit of the pulse

shapes for both signals also proves that the fast phosphor has a linear response to the charge impinging on it. Given all these features, the fast phosphor signal is reliable for diagnostic purpose on the beam. However, additional issues such as life time and the maximum charge density tolerance of the screen will still require more detailed experimental investigation.
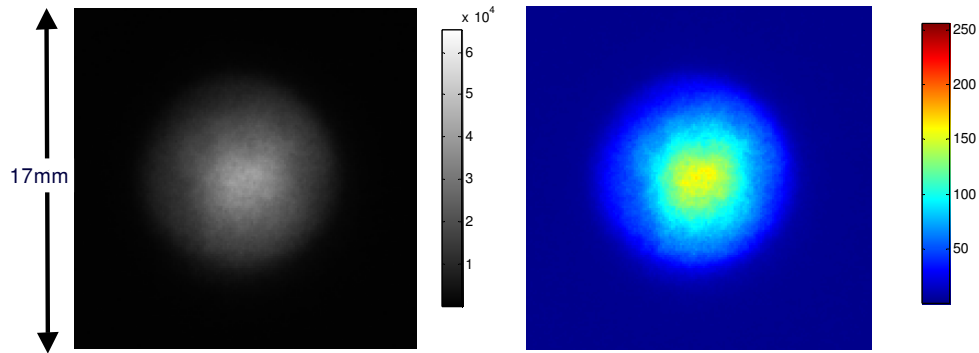


Figure 4.11: The image of the 23 mA parabolic beam, integrated over the entire beam pulse (left: greyscale; right: color coded).

Before taking the sliced images, a 150 ns long gate pulse was applied to the ICCD camera so that an integrated image of the whole 23 mA parabolic beam can be recorded. The result is shown in Figure 4.11. From both the grayscale and the color coded version of the beam photo, one can find that the beam has a relatively smooth distribution transversely, more or less like a Gaussian distribution. During the experiment, the currents of solenoids S1 and S2 were set to 4.7 A and 3 A, respectively.
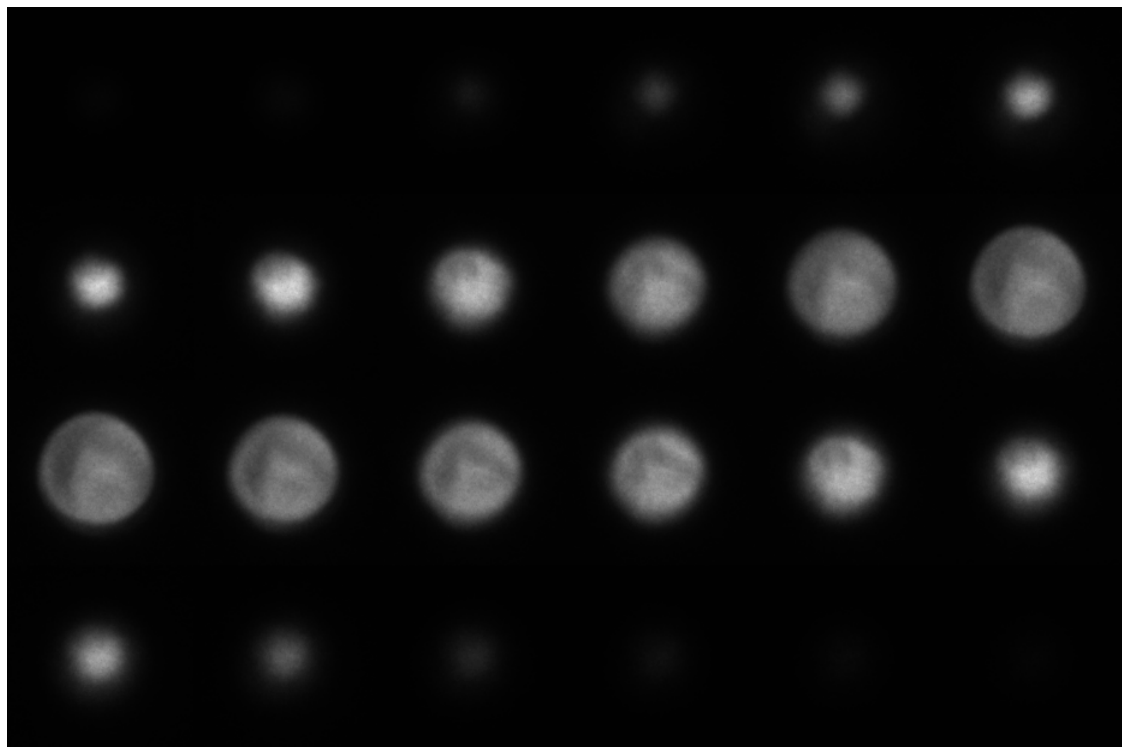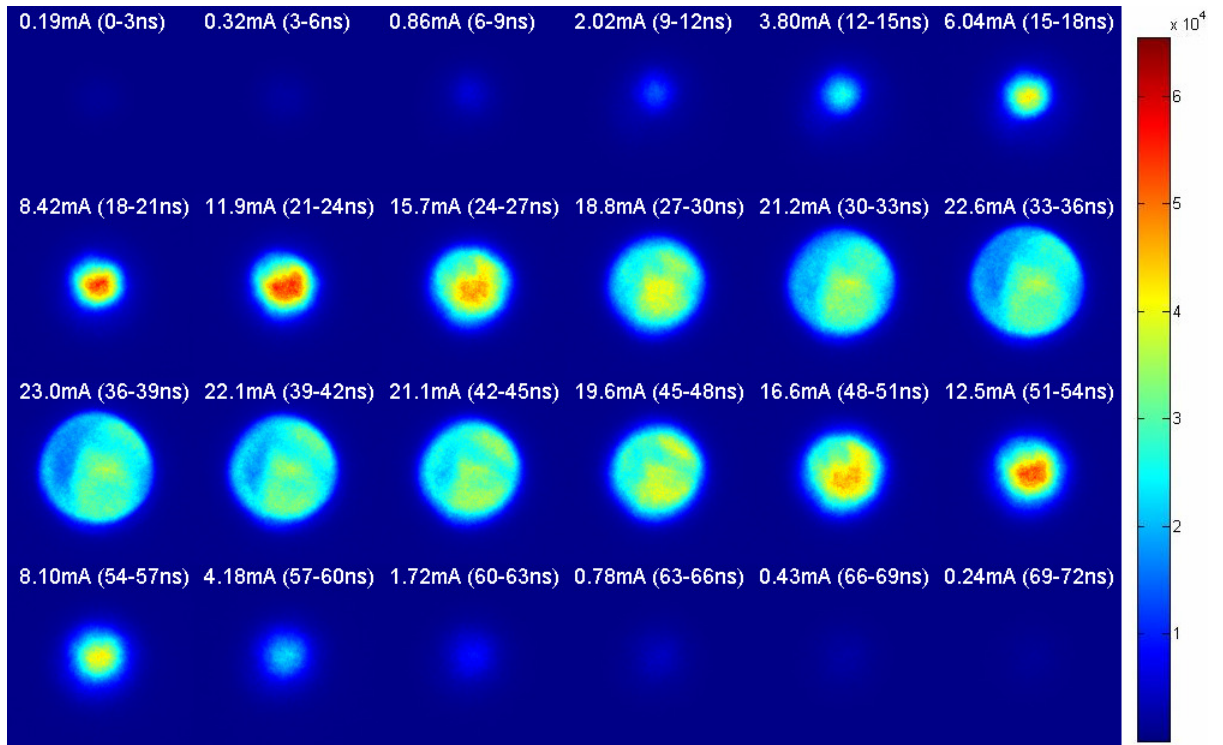
Figure 4.12: Progressive 3 ns sliced images along the 23 mA parabolic beam. Top: color coded; bottom: grayscale.

Since the light intensity of the fast phosphor is high enough that the beam image can be directly seen by eyes, it only took 6 frame integrations, about 0.1 second for the 60Hz beam, to obtain this integrated image of the whole beam. By simple scaling, one can estimate that a clear 3-ns sliced photo will take about 10 times more frame integrations than that of the whole beam image, which is still about 1 second only. Therefore, by moving the 3-ns gate window of the ICCD camera from the beam head to the beam tail with a time interval of 3 ns, a series of 3-ns sliced beam images can be taken progressively along the beam quickly and efficiently.

Figure 4.12 shows the progressive images of the beam using this method. The current value in each image is calculated from the scaled total light intensity of that image, which is proportional to the total charge in the 3 ns window and hence proportional to the average current as well. The time 0 ns represent the start point of the imaging process which is chosen to be near the beam head. One can easily notice that the 0%-to-0% pulse length obtained from the sliced images is more than 70 ns, while the 0%-to-0% pulse length measured by the Bergoz is only about 54 ns. The reason for that is partly because of the relatively slow falling tail of the light signal. On the other hand, the dynamic range of the 16-bit camera is so wide that we can capture the 3-ns sliced beam image with a current as low as 0.19 mA, which can not be detected by our oscilloscope from the Bergoz signal. Other than that, more interesting correlations between transverse and longitudinal dynamics are shown in the sliced images. Both the beam sizes and transverse distributions are changing all the time along the beam affected by the parabolic longitudinal current distribution. Consistent with the symmetry of the longitudinal current profile, the images with

similar average current have almost identical distribution. None of these sliced images has a similar distribution with the whole beam image in Figure 4.11 even though the same image as Figure 4.11 can be achieved by adding up all the sliced images. The distributions at the low current parts of the parabolic beam, i.e. close to both beam head and tail, are more or less symmetric and similar to the whole beam image. For the high current parts of the beam, i.e. between 24 ns and 51 ns, the internal transverse density distribution of the beam shows a changing structure. This structure appears to show higher order modes of body plasma waves. These transverse waves may be originated from the non-uniform emission from the cathode, which introduces transverse perturbations and propagate transversely [56].
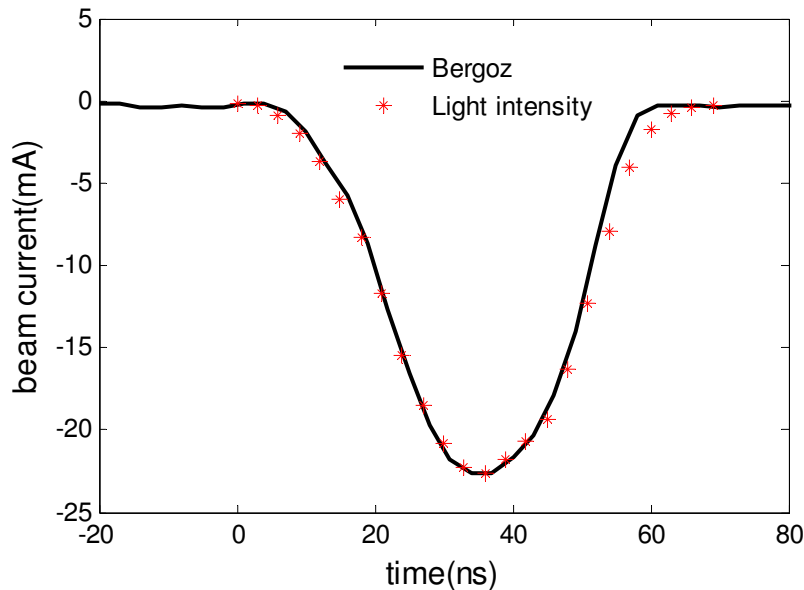


Figure 4.13: The total light intensity of each sliced image scaled according to the beam current profile.

As mentioned earlier, the light intensity of each sliced image can be used to estimate the average current for the beam that the sliced image represents. Figure 4.13

shows that these average current estimates fit with the current profile measured by the Bergoz current monitor very well. This is also a very good evident for the charge linearity of the light output from the fast phosphor screen.

From the 3-ns sliced images along the beam, we derive the two times rms radius of the beam envelope, which we plot as a function of time in Figure 4.14, where X= $2x_{rms}$ and Y= $2y_{rms}$ stand for the radius of the beam envelope in horizontal and vertical directions, respectively. As a result of the asymmetric distributions and exotic patterns for the higher current part of the beam, i.e. between 27 ns to 48 ns, the beam has a larger radius in the vertical direction than in the horizontal direction.
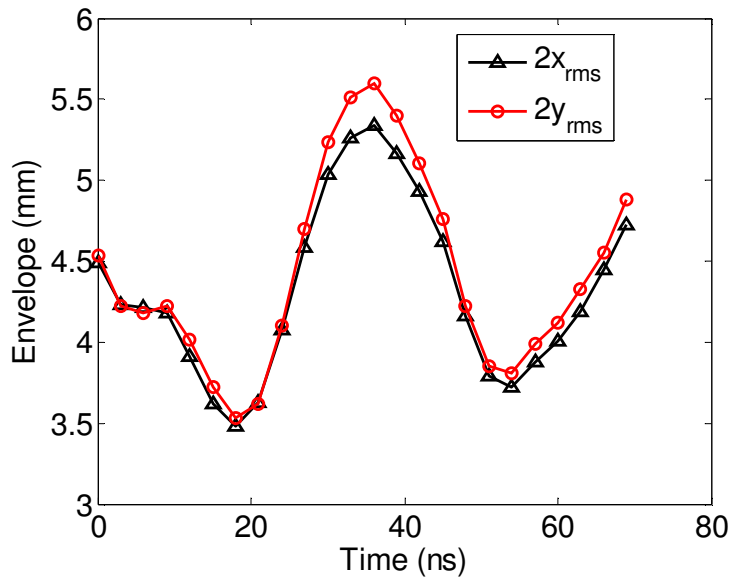


Figure 4.14: The rms radius (X: horizontal, Y: vertical) of the envelope for the 23mA parabolic beam, measured from the sliced photos. The accuracy is about 1% resulting from the error in estimating the spatial resolution of each pixel.

### 4.2.3 Time resolved imaging on the longitudinal perturbations

The experimental results from previous section using the parabolic beam validate the new type of phosphor screen as a fast imaging tool on our beam. In order to achieve the information of the correlation between the transverse distribution and the longitudinal current perturbations, we carried out experiments of the time resolved imaging on the longitudinal perturbations.
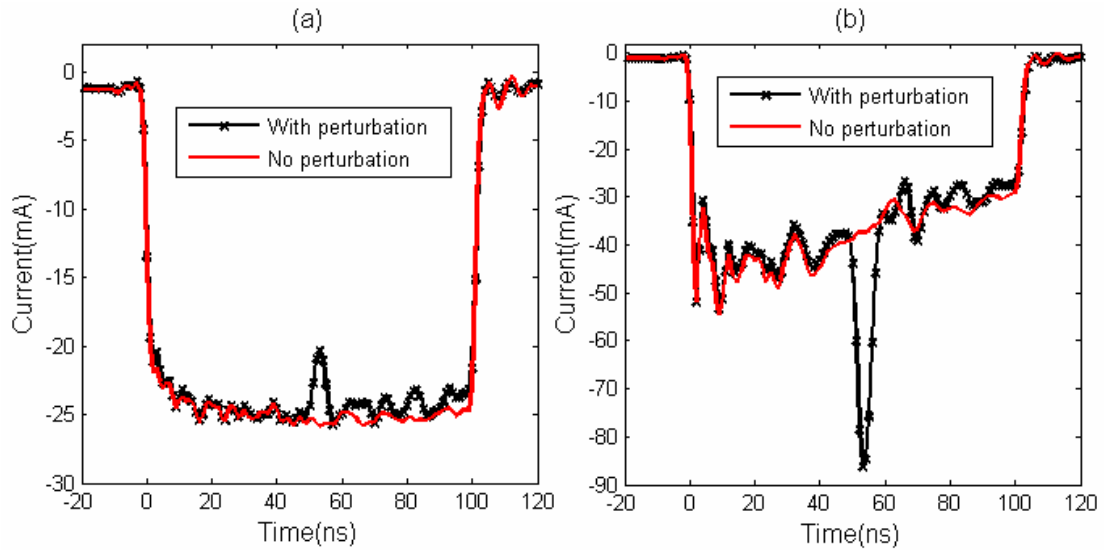


Figure 4.15: Current profiles of rectangular beams with and without perturbations. Bias voltage is 59V for both cases.

Both negative and positive perturbations were introduced into the rectangular beams at LSE system. For each of these cases, the electron gun was operated in amplification regime by setting the bias voltage to 59 V. If a gun aperture, which is 1.6 mm in radius, is in use, a negative current perturbation can be observed as shown in Figure 4.15 (a), in which the main beam current is about 25 mA and the perturbation strength is about 20%. Furthermore, a rectangular beam with a positive perturbation can be achieved when the beam aperture is removed. Figure 4.15 (b)

shows the beam current profile with a positive perturbation when the aperture plate is not applied. The main beam current is about 40 mA and the perturbation strength is over 100% which will introduce extremely nonlinear effects. By connecting or removing the perturbation cable from the control circuit of the electron gun, we can turn on and off the perturbations in both the 25 mA beam and the 40 mA beam. Beams without the perturbations are also presented in Figure 4.15 for comparison.
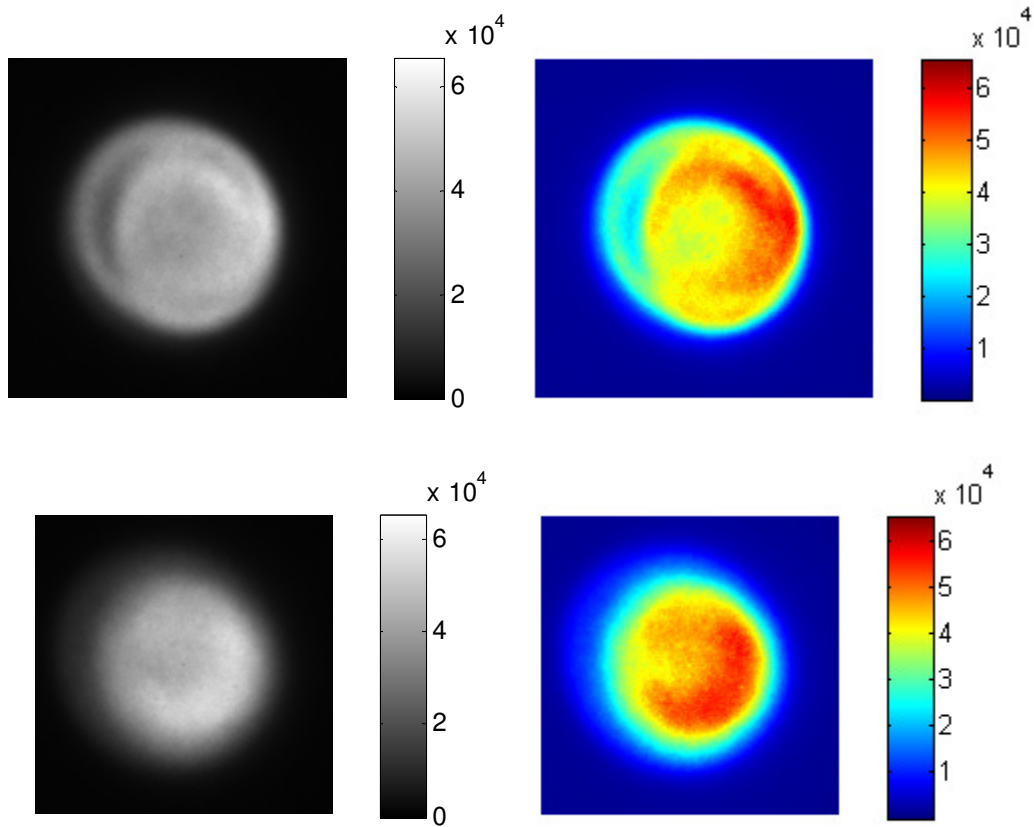


Figure 4.16: Integrated images for the whole beam. Top: 25 mA beam with a negative perturbation; Bottom: 40 mA beam with a positive perturbation. For both cases, the bias voltage is 59V; the current for S1 and S2 are 4.7A and 3.4A, respectively.

Using the same technique as for the parabolic beam, both time-integrated images and progressive time resolved images were taken for the 25 mA beam and the 40 mA with the perturbations turned on and off. The integrated images of these two beams with perturbations are shown in Figure 4.16 along with the color-coded version respectively. The time-integrated images for these two beams without perturbations look the same as those with perturbations, therefore, we do not show them here. The photos in Figure 4.16 are taken with the same lens with exactly same focal length, so they have the same spatial resolution per pixel. Therefore, we can directly compare the beam sizes from these photos and find that the 40 mA beam has a slightly smaller beam size. This is because the envelope oscillations of the two beams were different due to the same magnets strengths using in experiment. In addition, the internal particle density distributions of both beams are not uniform and show different structures which may indicate some sort of high-order body waves.
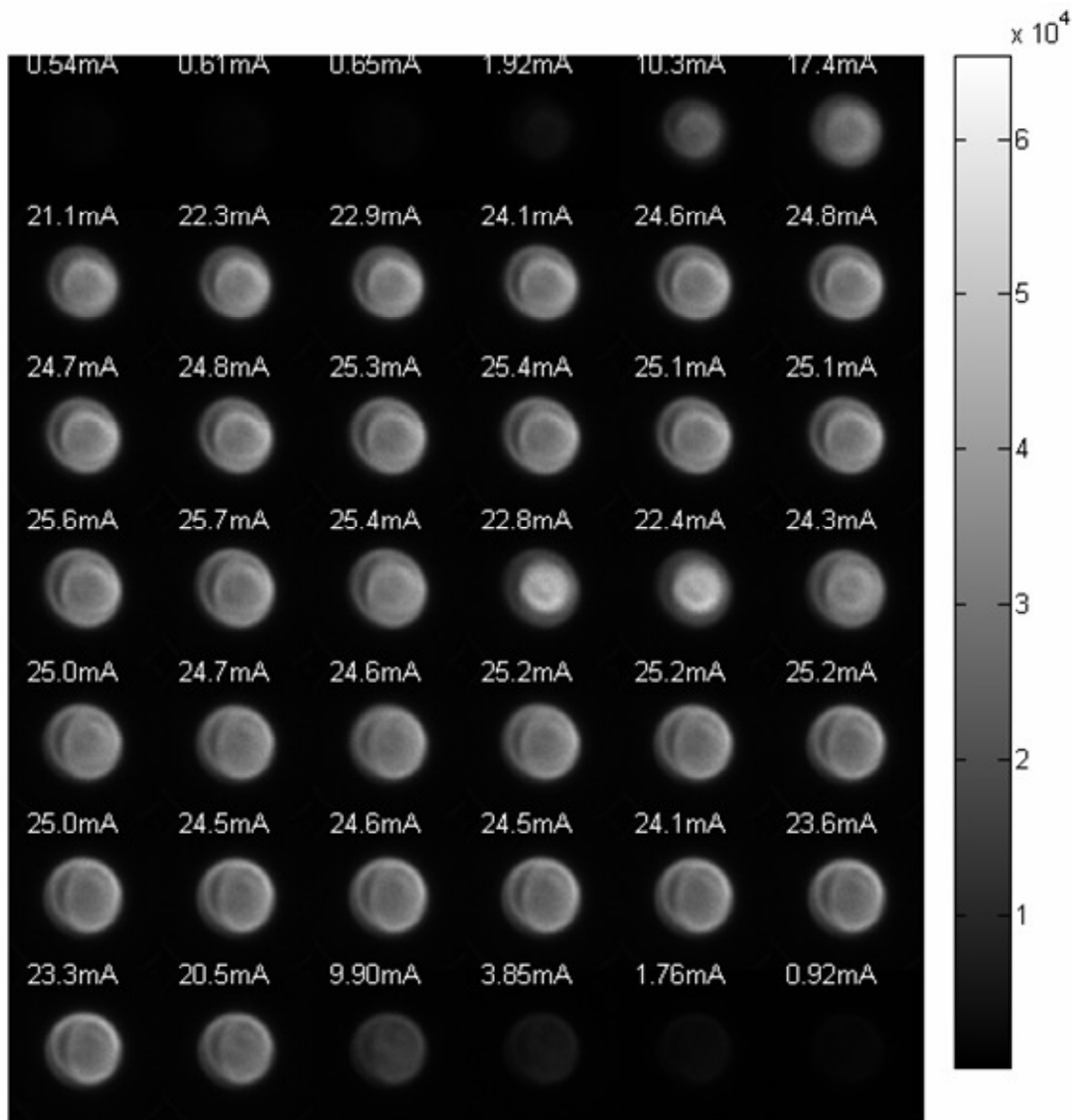
Figure 4.17: Progressive 3-ns sliced images of the 25 mA beam with a negative

perturbation (grayscale).
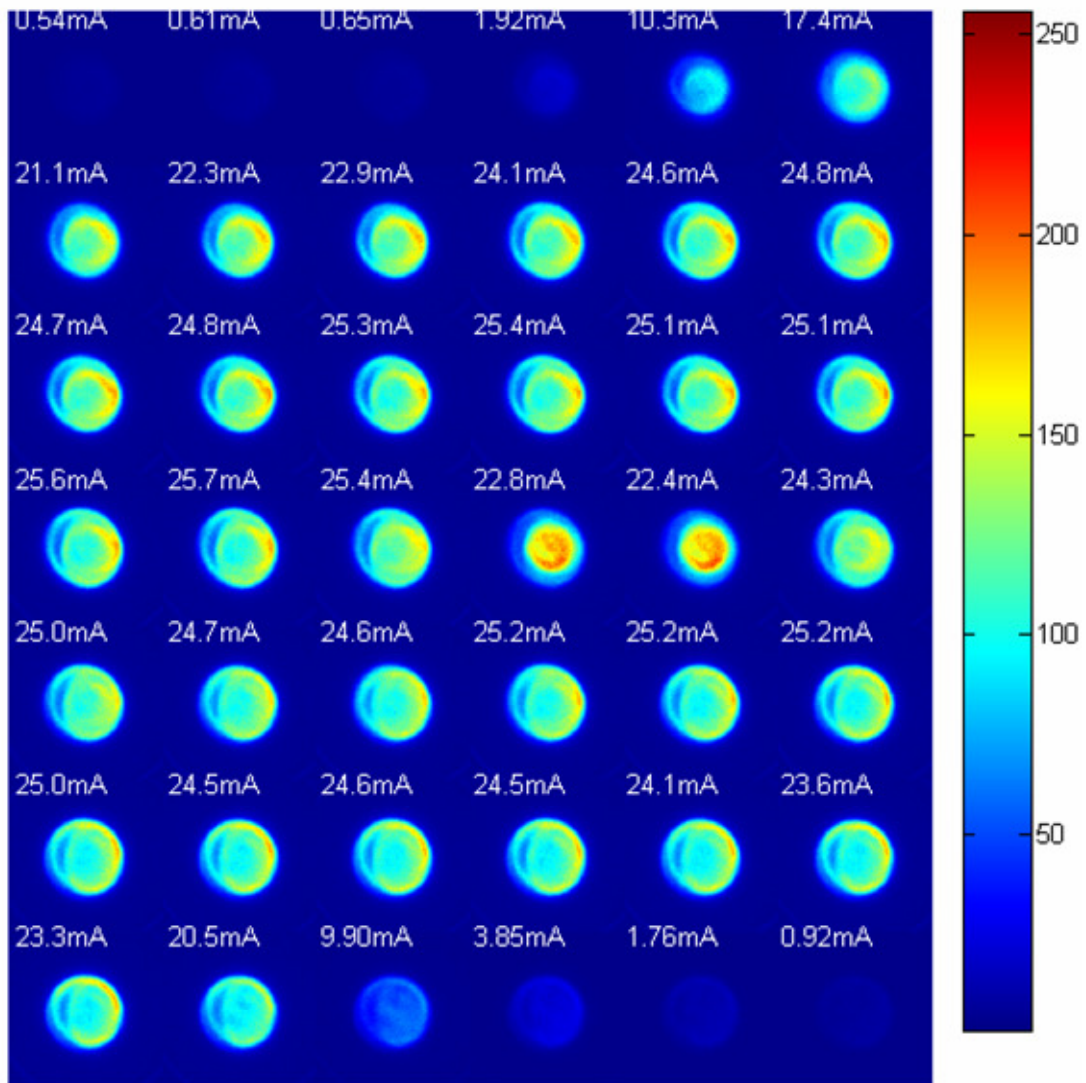
Figure 4.18: Progressive 3-ns sliced images of the 25 mA beam with a negative

perturbation (color-coded).
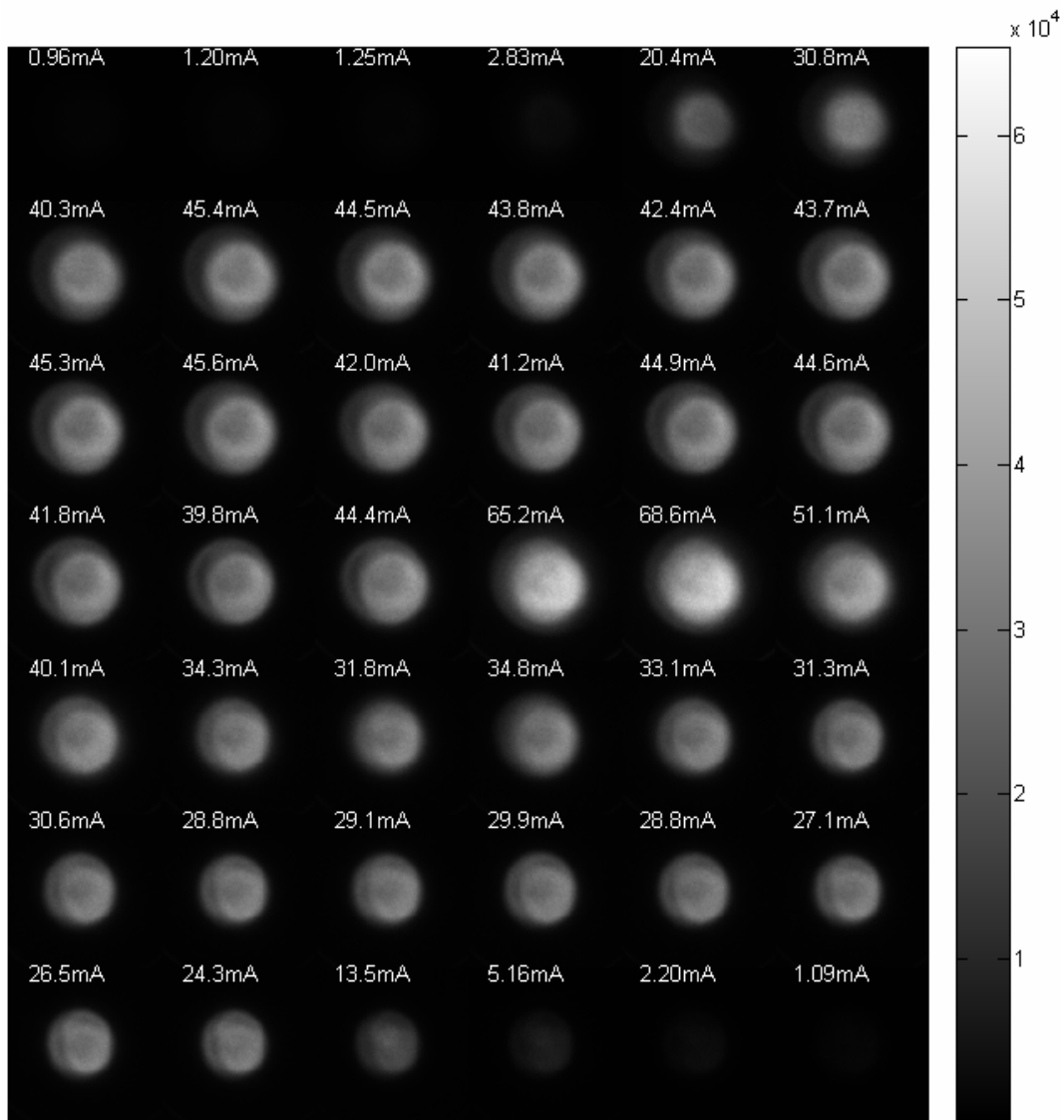
Figure 4.19: Progressive 3-ns sliced images of the 40 mA beam with a positive
perturbation (grayscale).
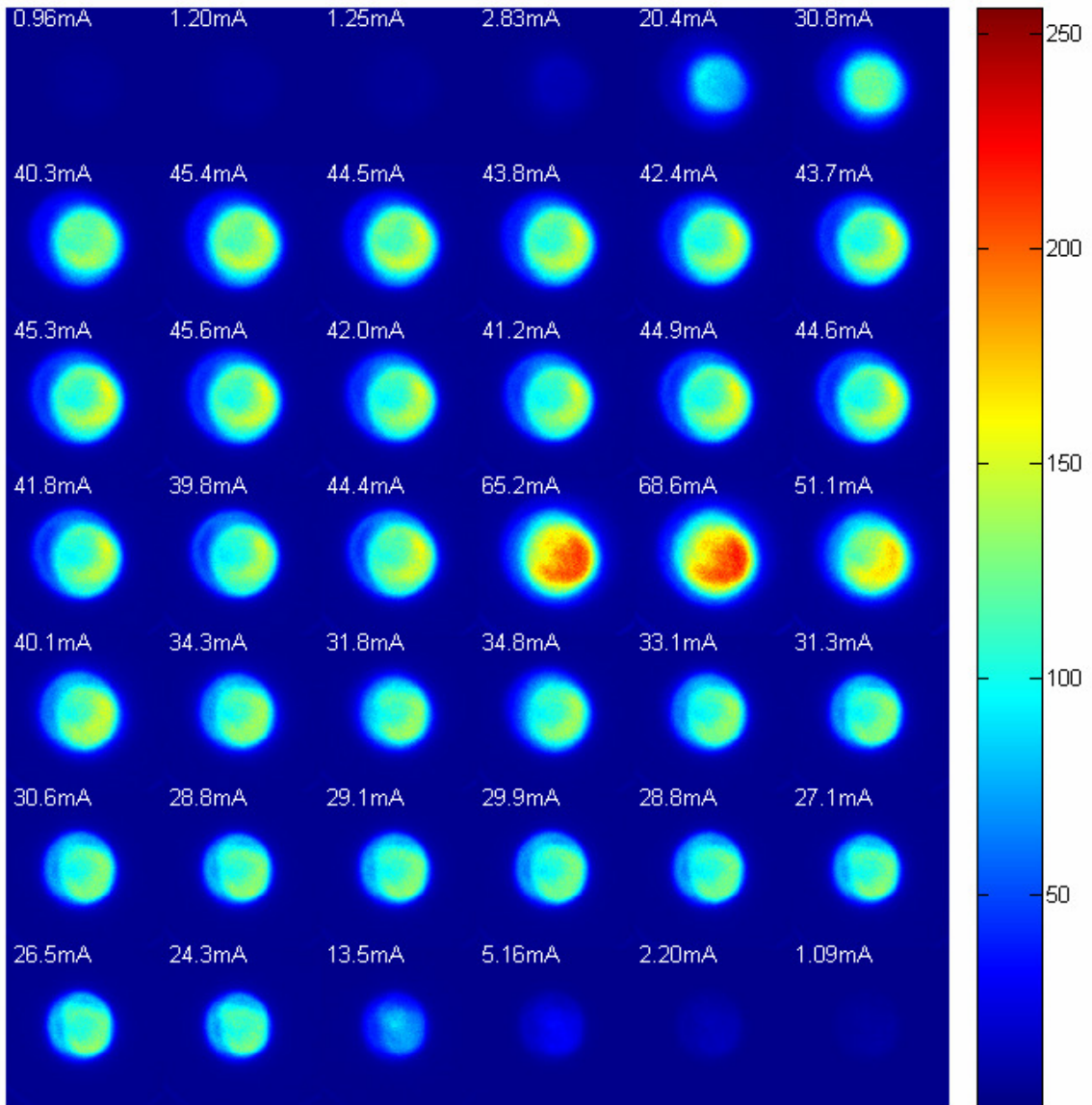
Figure 4.20: Progressive 3-ns sliced images of the 40 mA beam with a positive

perturbation (color-coded).
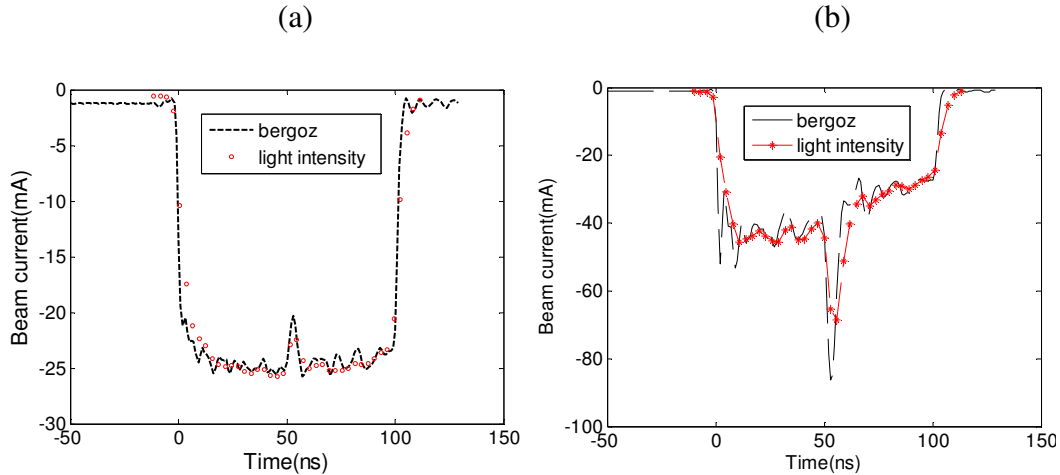
Figure 4.21: Comparison of the total light intensity and Bergoz signal. (a): perturbed 25 mA beam; (b): perturbed 40 mA beam.

The progressive sliced 3 ns images for the 25mA beam with a perturbation are shown in Figures 4.17 (greyscale) and 4.18 (color-coded), covering a length of 126 ns from the beam head to tail. The labelled current values in the images are calculated from the scaled light intensity as we did with the parabolic beam earlier. The comparison of the current profiles derived from the light intensity and Bergoz monitor is shown in Figure 4.21 (a), which is helpful for locating the longitudinal position of each image. The 25 mA beam has a relatively flat top, i.e., a constant current, except for the perturbation region when the perturbation was turned on. Consequently, the time-sliced images show almost no difference for the unperturbed part of the beam between 22 ns and 84 ns, indicating a constant transverse distribution due to the constant beam current. By comparing these images with the integrated image shown in Figure 4.16, one can find that they have extremely similar transverse distributions. It is quite obvious that the images with average current of 22.8 mA and 22.4 mA, which were taken inside the perturbation, have slightly

smaller sizes and different internal density distributions than images taken at other locations along the beam. Another interesting observation is that, for both perturbed and unperturbed parts of beams, the image of the beam consists of a dense core surrounded by a faint halo.

Progressive sliced images covering the perturbation of the 40 mA beam are shown in both Figure 4.19 and Figure 4.20. Average currents calculated from scaled light intensity are shown in Figure 4.21(b) along with the Bergoz signal and also are indicated on the top of each sliced image. The current profile of the 40 mA beam is tilted with a slope, which leads to a continuous current decrease along the beam. As a result, the beam size varies accordingly and become noticeably smaller towards the beam end. From Figure 4.19 or 4.20, the images inside the perturbation can be easily identified and correspond to average currents of 65.2 mA, 68.6 mA, and 51.1 mA, which have significantly bigger current values than other images.

For better comparison of the beam with and without perturbations, we show the sliced images covering the perturbation along with the images taken at the same location for the unperturbed beams in Figure 4.22. In Figure 4.22(b), the first photo was taken at the onset of the perturbation and the fourth photo was taken at the end of the perturbation. Photos in Figure 4.22(a) were taken at the same locations with those in Figure 4.22(b) but without a perturbation. The four photos in Figure 4.22(a) are almost identical, as expected from the constant longitudinal distribution. By comparing the second and the third photos in Figure 4.22 (a) and (b), one can find that both transverse distributions and sizes change dramatically in the perturbed region when the perturbation is turned on. Inside the perturbation, the beam core is

more intense and smaller than any other parts of beams, while the halo ring around the core is smaller and weaker. Nevertheless, beam cores for all cases show a hollow distribution, which may be a sign of the existence of transverse space charge waves. The correlation between transverse and longitudinal waves can be a very interesting topic for future study.
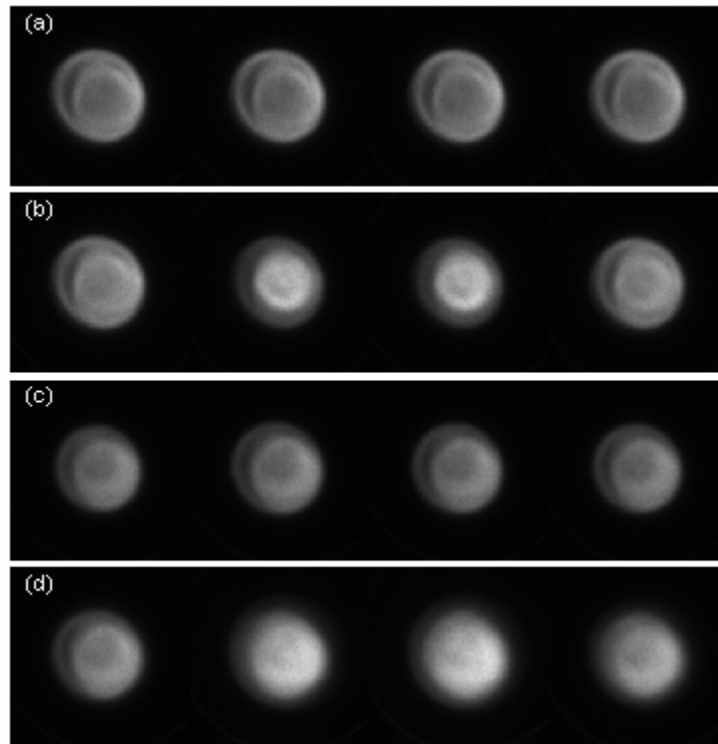


Figure 4.22: Comparison of sliced images of perturbed and unperturbed beams. (a) unperturbed 25 mA beam; (b) perturbed 25 mA beam; (c) unperturbed 40 mA beam; (d) perturbed 40mA beam.

In Figure 4.22 (c) and (d), we compare the 40 mA beams with and without a perturbation. Similar to the 25 mA beam, inside the perturbation of the 40 mA beam, the beam core is more intense and the halo becomes weaker. But, due to the positive

polarity of the perturbation, the beam core is slighter bigger than other parts of the beam. Hollow distributions of the beam cores exist for all the 8 photos even though the hollowness is not so obvious for those inside the perturbation.

Following a similar procedure as to the parabolic beam, we can also calculate the rms radius for the envelope of the 25 mA beam and 40 mA beam. Furthermore, the time resolved current density along the beam can be derived from the current and envelope information.
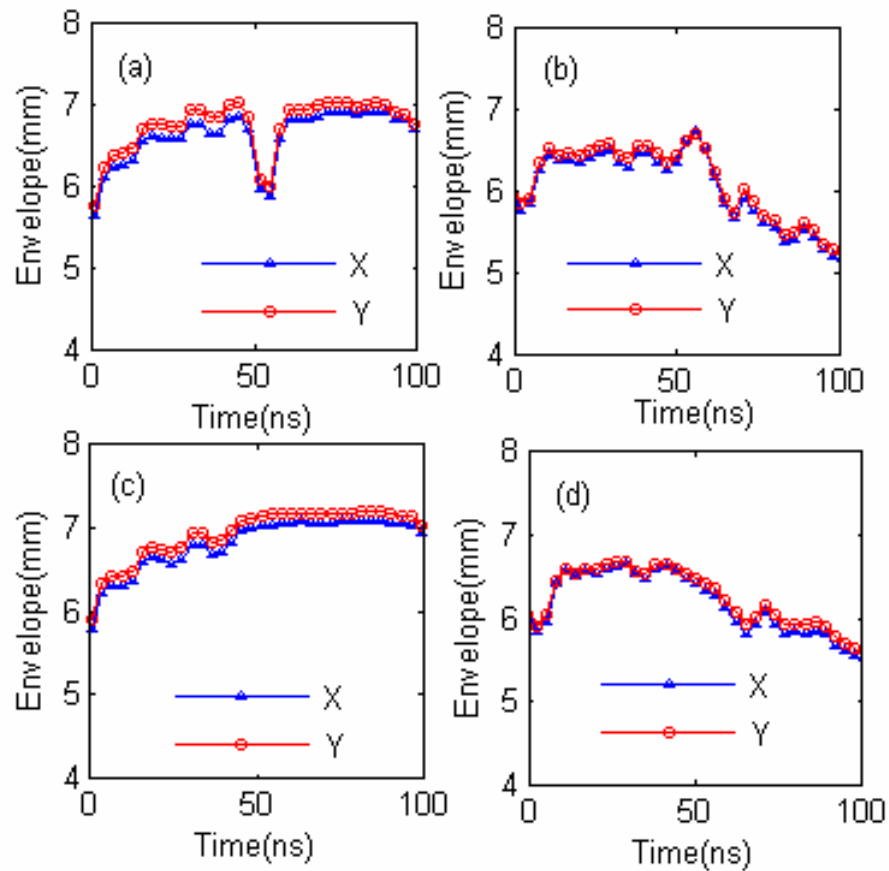


Figure 4.23: The rms radius of beam envelope for different beams. (a) 25mA perturbed beam; (b) 40 mA perturbed beam; (c) 25 mA unperturbed beam; (d) 40 mA unperturbed beam.

The rms radius of the envelope for the perturbed and unperturbed 25 mA beams calculated from the sliced images can be found in Figure 4.23(a) and Figure 4.23(c) respectively, which indicate smaller transverse beam radius inside the perturbation. Due to the positive perturbation of the 40 mA beam, the beam sizes increase slightly inside the perturbation as shown in the plot of the envelope along the perturbed beam in Figure 4.23(b) in comparison with the unperturbed beam envelope in Figure 4.23(d). Although the perturbation amplitude of the 40 mA beam is much higher than that of the 25 mA beam, the increase in beam size of the 40 mA beam is much smaller than the decrease in beam size of the 25 mA beam. There is no clear explanation for this observation now, but it may relate to the envelope oscillation causing by the two matching solenoids S1 and S2.

If we define a quantity $\tilde{J}_n = \dfrac{I}{XY}$, where I is the current, by normalizing $\tilde{J}_n$ along the beam pulse, we can derive the normalized current density as a function of time. In Figure 4.24, we plot the normalized beam current and current density for both the perturbed 25 mA beam and perturbed 40 mA beam. We can see for both cases, the current density increases inside the perturbation regardless of negative or positive current perturbation. This is consistent with the fact that both beams are actually identical inside the gun and the gun aperture only cuts down the current rather than change the density.
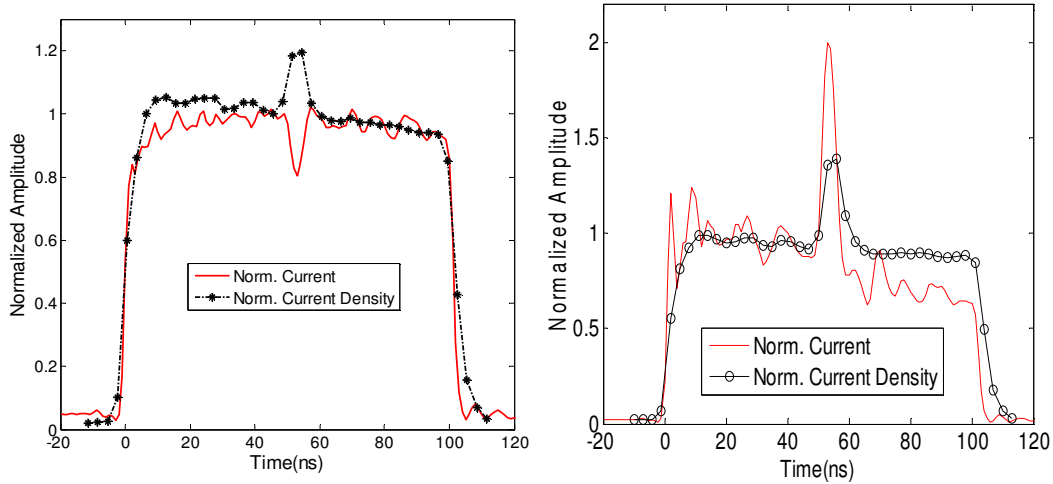
Figure 4.24: Normalized current density profiles and normalized current profiles of the perturbed 25 mA (left) and 40 mA (right) beams.

### 4.2.4 Correlation with the longitudinal energy profile

Fast imaging over the beam pulse provides us time resolved information of the transverse configuration space. With the energy analyzer in LC1, we can measure the longitudinal phase space at the same location of the fast phosphor screen. Also, comparing the energy profiles measured at LC1 and LC2 will add to our understanding of the evolution of the longitudinal dynamics of the parabolic beam and the space-charge waves of the two rectangular beams. In this section, we present these energy measurements results of the 23 mA parabolic beam, 25 mA perturbed rectangular beam, and the 40 mA perturbed rectangular beams.
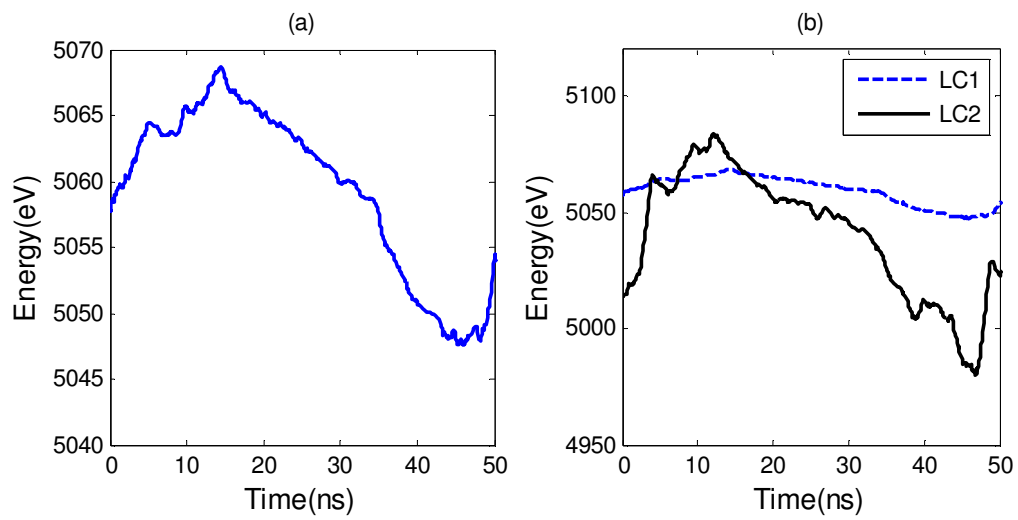
Figure 4.25: The longitudinal mean energy profiles of the parabolic beam measured at two chambers ((a): LC1; (b): LC1 and LC2).
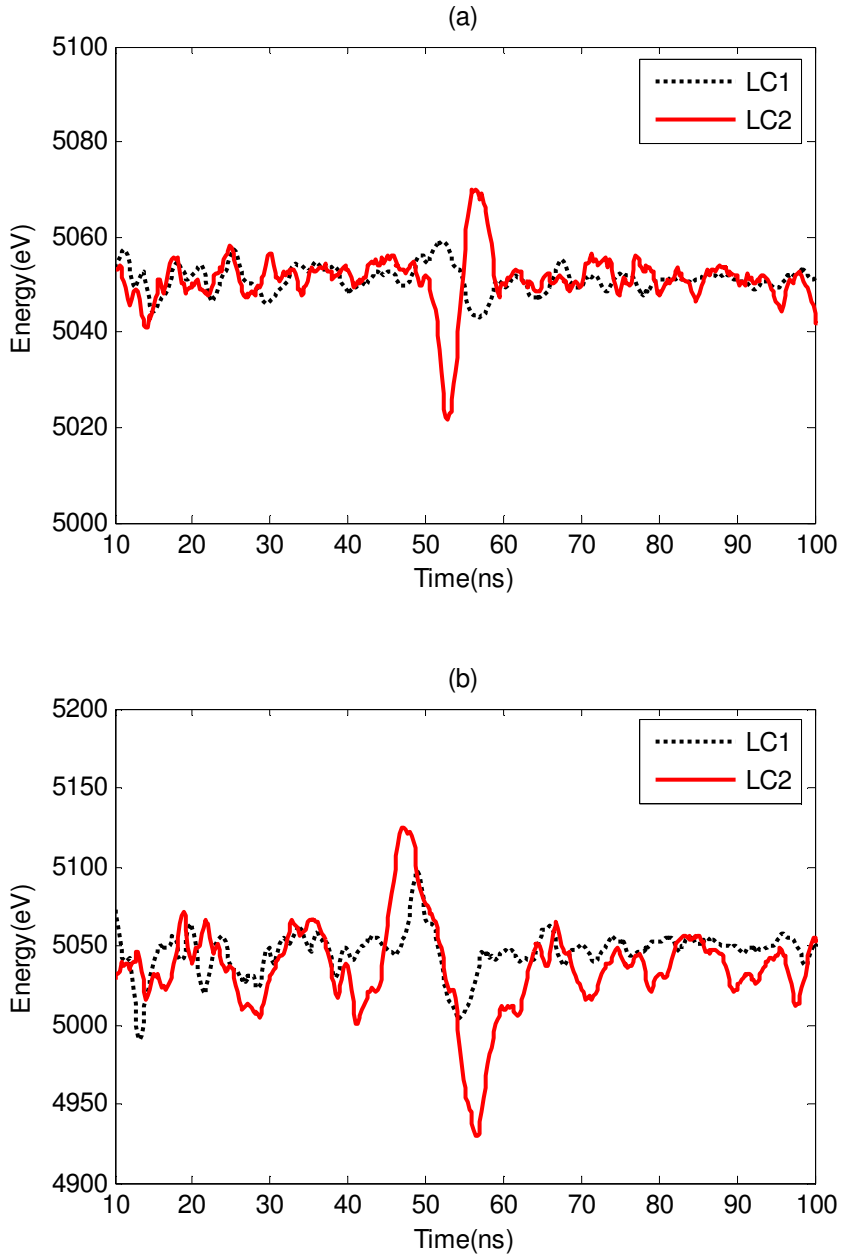
Figure 4.26: The longitudinal mean energy profiles of the two rectangular beams measured at LC1 (black dotted lines) and LC2 (red solid lines). ((a): 25 mA beam; (b): 40 mA beam).

The measurement results of mean energy profiles of the parabolic beam in LC1 and LC2 are shown in Figure 4.25. At both locations, the energy profiles exhibit very similar shapes of a roughly linear tilt at the center and two ear shapes structure at the head and tail. The tilted mean energy is due to the self electric field inside the imperfect parabolic beam. Equation (2.26) indicates that the self field is proportional to $g\frac{\partial \Lambda}{\partial z}$. If we assume that the g factor is a constant and longitudinal velocity variation is small, the distribution of line charge density $\Lambda$ has a parabolic shape too. Thus, the self electrical field is a linear function along the longitudinal direction of the beam. However, the g factor is not a constant along the beam due to the envelope oscillation, as indicated in Figure 4.14. Therefore, the shape of the mean energy profiles in Figure 4.25 may suggest that near the beam center, the value of the longitudinal self field is dominated by $\frac{\partial \Lambda}{\partial z}$, exhibiting a linear relationship with z, but at both the head and tail, it is dominated by the value of g, where the self field decrease with the increasing beam size.

The measurement results in Figure 4.26 are consistent with earlier measurements shown in Figure 3.19, but some discrepancy still exists. Due to the negative current perturbation of the 25 mA beam, the energy profile of space-charge waves should have a negative peak of fast wave and a positive peak of slow wave. However, in LC1, we observed a small energy modulation with two peaks having opposite polarities. It is possible that at LC1, the 25 mA beam still possesses the signature of the modulation in the gun pulse voltage.

## 4.2.5 Time resolved transverse phase space measurement

By illuminating an object from many different directions, the cross-sectional imaging of the object can be reconstructed from either transmission or reflection data. Such a technique that is referred as tomography has been widely used in medical imaging and many other non-medical applications. Recently, it has been employed as a technique to construct the transverse phase space using quadrupole magnets [30, 57, 58] and solenoid magnets [56]. The fast phosphor screen provides us the capability to constructed time-resolved transverse phase space. In this section, we present some preliminary results of time-resolved phase space measurement of the 23 mA parabolic beam using the tomography technique. For more details about the tomography technique, please see reference [59].
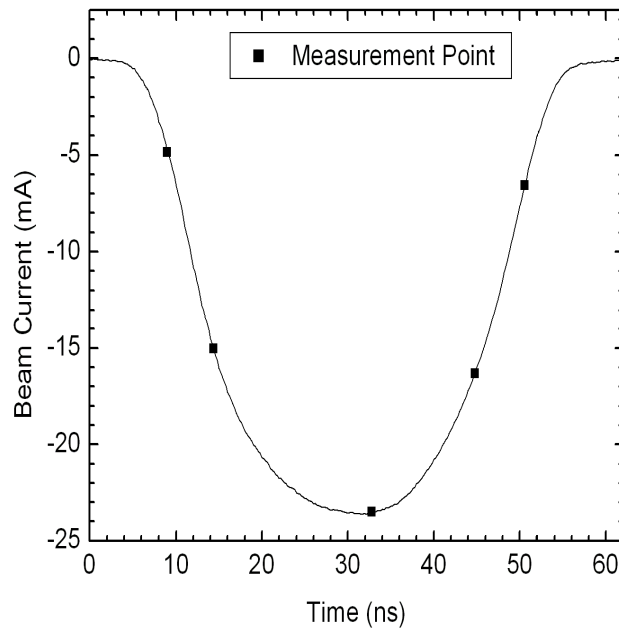


Figure 4.27: Illustration of positions where the transverse phase space are measured in the 23 mA parabolic beam [59].

During the experiment, we choose five different locations along the beam to construct the phase space as shown in Figure 4.27. The measurement results are shown in Figure 4.28 along with the transverse distribution of the beam, i.e. XY configuration space. For the parabolic beam, the beam current is symmetry as well as the transverse distribution. Consistent with the symmetry parabolic beam, both the configuration space and phase space are almost identical for longitudinal beam slices with similar average current. For the beam slice with more structures in configuration space, such as the slice between 33-36 ns, there are fewer structures in the phase space than those have more smooth distribution in configuration space.
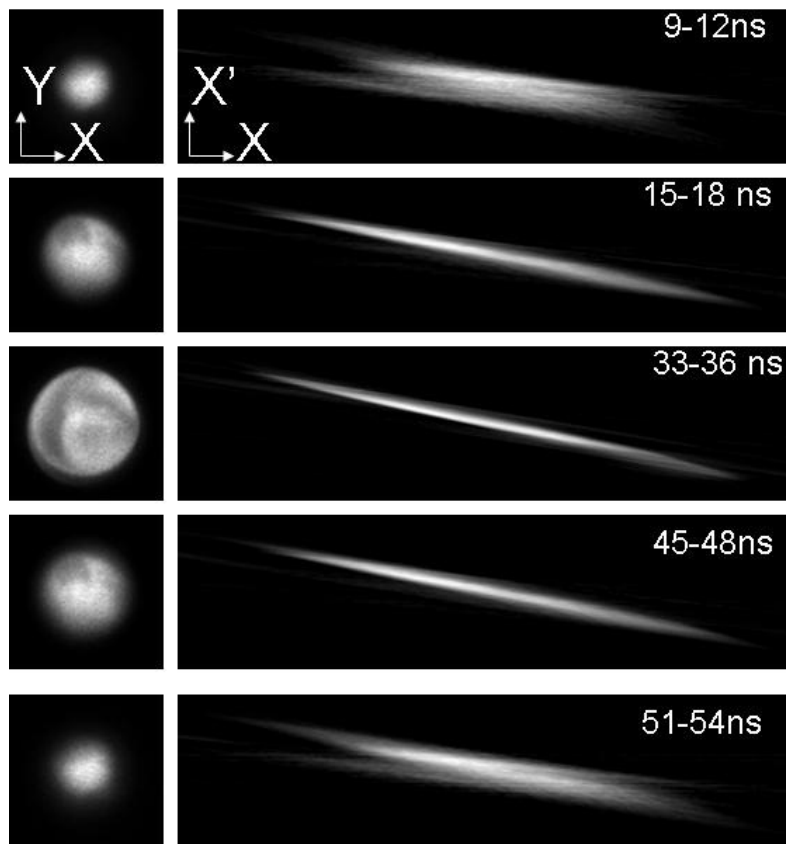


Figure 4.28: Time-resolved $XX'$ phase space of the 23 mA parabolic beam (left: configuration space; right: phase space) [59].

We can obtain the time dependent slope and emittance profile from the time-resolved transverse phase space. They will be useful for the simulation study of longitudinal beam dynamics in future. Furthermore, combining with the longitudinal energy profile measured by the energy analyzer at LC1 shown in Figure 4.25(a), we have constructed full 6-D phase space distributions, which can be beneficial to future 3-D simulation by providing detailed initial conditions.

## 4.3 Summary

In this chapter, we demonstrated two techniques for fast imaging of the longitudinal modulations in space-charge dominated beams. With OTR stations in UMER, we observed that the transverse distribution and beam size are affected by the longitudinal dynamics in space-charge dominated beams. However, even though the beam in UMER was extremely stable, a fact verified experimentally, the low light intensity still became a major limitation. Thus, an alternative diagnostic technique using a fast phosphor screen has been developed and fully validated in the LSE system. Progressive time resolved images have been taken for different beam profiles: a parabolic beam, two rectangular beams with and without perturbations. The results are very promising and encouraging in the sense that the time resolved images provide a lot of information which an integration image could not show. In addition, the fast phosphor screen and the high resolution energy analyzer enables us, for the first time, experimentally construct the 6-D phase space distribution of a space-charge dominated beam.

The sliced images are beneficial to the simulation studies of the space-charge waves in chapter 5 by providing detailed initial transverse envelope profiles. Also, at the same position of the fast phosphor screen, we have the high resolution energy analyzer, which can provide the time resolved energy profiles along the beam. Therefore, we can set up the WARP simulation starting from LC1 instead from the gun aperture, where the initial conditions of the beams are not very clear for us. In next chapter, we will present our efforts in WARP simulations using more realistic initial conditions measured from the experiments.

# Chapter 5 Simulation Study on Space-Charge Waves

Computer simulations are particularly useful for discovering and explaining the unknown physics encountered during the experiment. With proper modeling, simulations can also be used to direct the experimental study and predict new results.

In this chapter, we apply WARP simulations to investigate the physics that cannot be fully understood using 1-D theory. Sec 5.1 describes simulation of the 23mA parabolic beam. Then in Sec. 5.2, we study the evolution of space-charge waves in the 25 mA and 40 mA perturbed rectangular beam using the new WARP codes in lab frame. Finally, Sec 5.3 concludes with some general remarks.

## 5.1 Simulations of the Parabolic Beam

The 23 mA parabolic beam has been used to test the fast phosphor screen in the pervious chapter. In a similar manner, we start the simulation study with this beam by comparing the simulations results in both the beam and lab frame with the longitudinal energy profiles measured by the high resolution energy analyzers.

WARP [34] has the capability of simulating the beam in the beam frame or in the lab frame. In WARP beam frame simulation, we first load a 3-D distribution of particles conforming to the measured current waveform at B1. We then make assumption regarding other parameters such as the beam radius and slope to be constant. WARP then moves the beam center and all spatial grids for a distance equal to the length of the beam transport line. As a result, all the simulation data is acquired at different spatial locations but at the same time, unlike the experiment where data is collected at the same location as a function of time.

Lab frame simulations in WARP involve injecting particles as a function of time from one end of a fixed grid. We have full control over the injected particle density, energy, radius, and emittance at each time step, allowing us to completely match our input distribution to measured experimental data. Output data are similarly extracted as a function of time at a given location, exactly as the experiment. This promises better agreement between them.
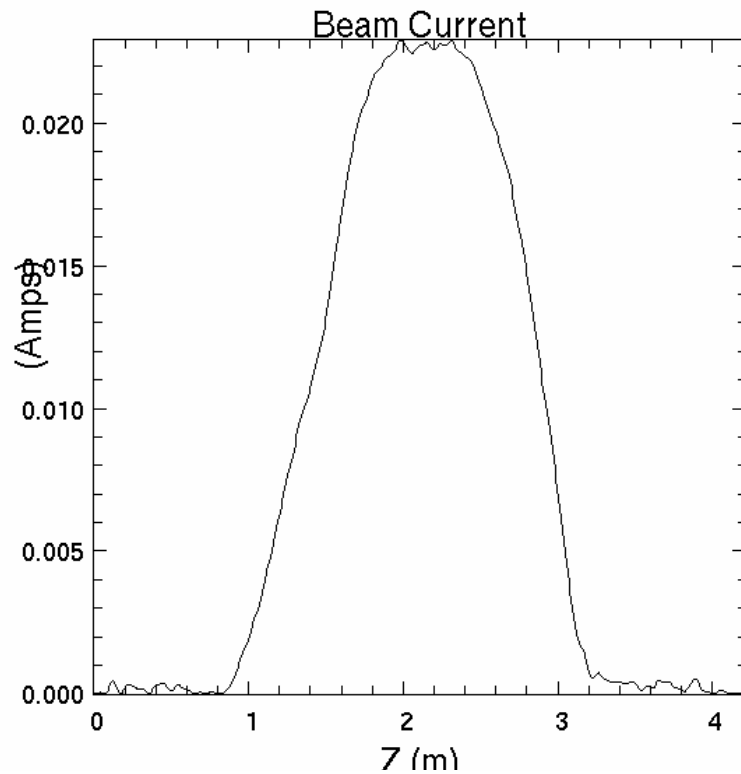


Figure 5.1: The initial condition for the beam current in the simulation. In the simulation, we use positrons instead of electrons; therefore, the current profile shows positive amplitude here.

First we simulated the transport of the parabolic beam in the LSE system using WARP-RZ code in beam frame. We assume uniform focusing to represent the long solenoid with focusing strength $\kappa = 70.5\,m^{-2}$. As shown in Figure 5.1, the current profile measured by B1 was imported into WARP as the initial condition of the beam current. Since the simulation is in the beam frame, we need transfer the measured current profile, a function of time, into the beam frame by multiplying the time axis by the main beam velocity. We use a semi Gaussian for the initial transverse distribution, which is uniform in space and Gaussian in velocity space, with a uniform temperature. We assume a constant initial radius of 3.5 mm, the matched radius of 14 mA beam inside the long solenoid, a zero slope, and a constant longitudinal kinetic energy of 5050 eV along the beam. Numerical settings for simulation are: the particle number is 200,000; time step for pushing particles is $2.36 \times 10^{-10}$ second; the number of cells in the x or y direction is 32; the number of cells in the z direction is 256; the grid spacing in x or y direction is $5.95 \times 10^{-4}$ m; the grid spacing in z direction is $8.24 \times 10^{-3}$ m. These numerical parameters have been tested to ensure adequate accuracy.

We took a snapshot of the mean energy profiles of the beam when the beam center was transported for 40.5 cm and 234.0cm, i.e. the distance from the aperture plate to front plates of two energy analyzers in LSE system. The simulation results for the longitudinal mean energy profiles at LC1 and LC2 are compared with those measured by energy analyzers in Figure 5.2. One should note that the vertical scales of Figure 5.2(a) and 5.2(b) are different.
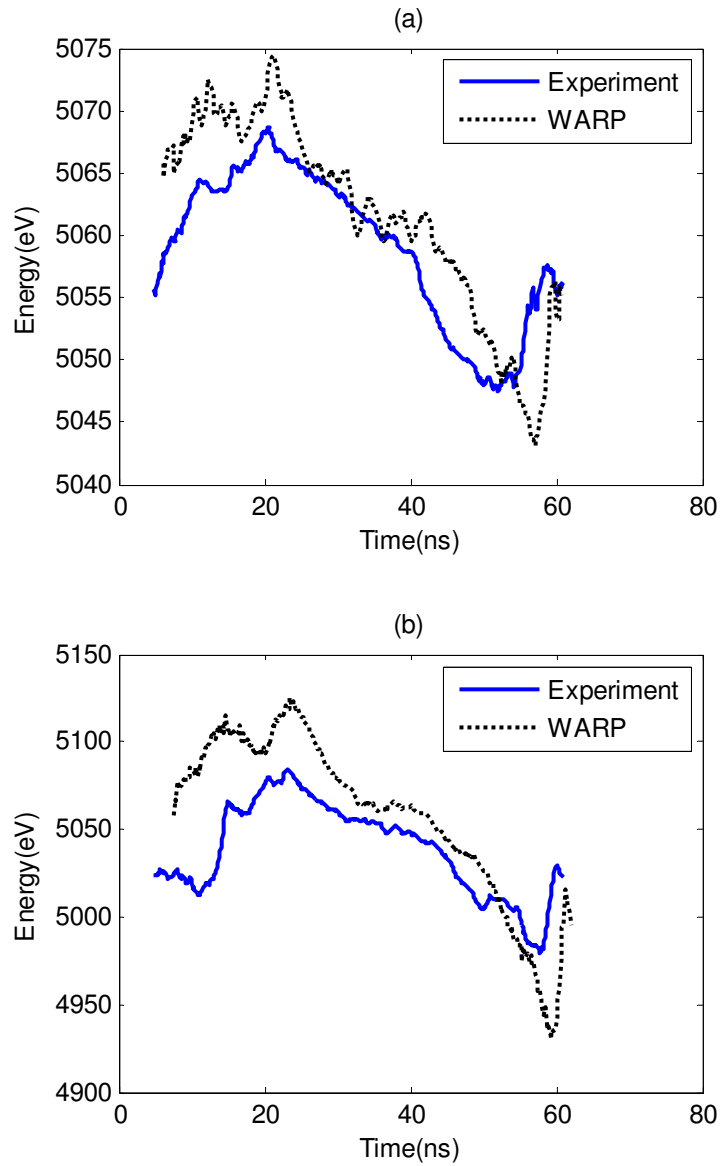
Figure 5.2: Comparison of mean energy profiles of the 23 mA parabolic beam between the WARP simulations in the beam frame (black dash lines) and the experimental results (blue solid lines). (a): at LC1; (b) at LC2.

In LC1, the simulation result has a good fit with the experimental measurement for the center of the beam, namely from 30 ns to 50ns, but a relatively large discrepancy for the beam head and tail. The simulation result shows higher energy for the head and lower energy for the end than those measured in the experiment. In addition, the energy profile from the simulation shows more oscillations than the experimental results On the other hand, there is bigger difference between the simulation and experimental results in LC2. The simulation result exhibit a larger slope for the beam center. Since the tilt of the mean energy profile is due to the longitudinal electric field, the differences in Figure 5.2 between the simulation and the experiment indicate that the longitudinal electric field calculated in WARP is different from the real field in the experiment. The discrepancy can be due to the following facts: First, in beam frame simulation, beam head travels longer distance than in experiment, while the tail travels shorter distance. Second, the beam frame simulation does not have adequate transverse information of the beam. Third, there is a discrepancy between the uniform focusing model in WARP and the solenoid channels in reality.

To address these issues, we set up a lab frame WARP-RZ simulations for the parabolic beam with individual solenoids that have the same strengths as those used in experiment. Here, we start the simulation from the front surface of the energy analyzer in LC1 instead of the gun aperture. Because we have both a fast phosphor screen and an energy analyzer at this plane, at each time step we inject a different energy and transverse radius. Like the beam frame simulation, we still use a semi Gaussian for the initial transverse distribution.
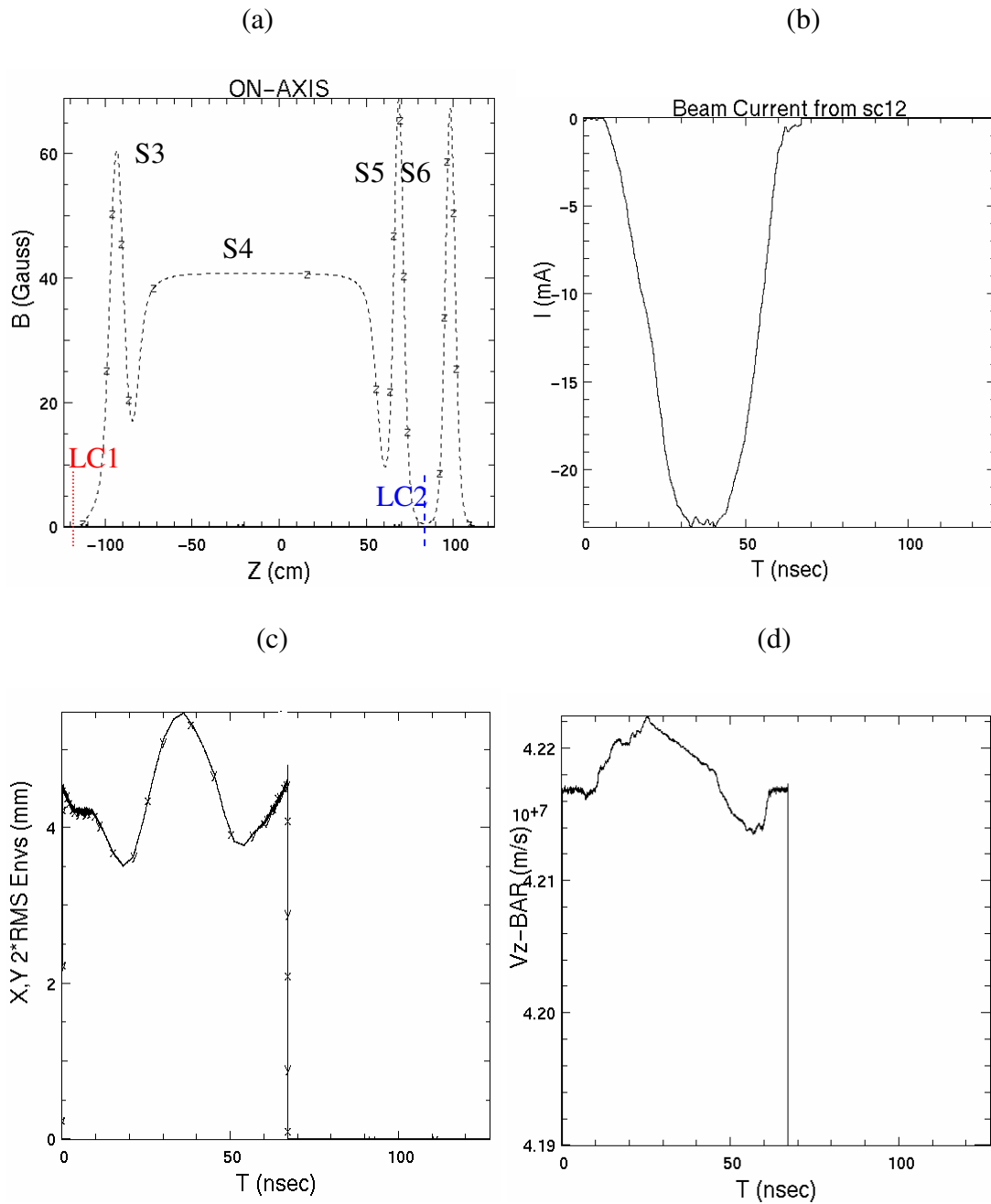
Figure 5.3: Lab frame simulation input parameters for the parabolic beam. (a): On-axis magnetic fields strengths of solenoids; (b) injected beam current profile; (c): beam envelope profile; (d): longitudinal mean velocity.

Each of the measured mean energy and current profiles has a time resolution of 0.2 ns, but the transverse envelope profile shown in Figure 4.13 has a resolution of 3 ns only. For the convenience of particle injections in WARP, we interpolate the measured data of envelope radius linearly so that a 0.2 ns resolution can be achieved. We assume zero slope and a constant emittance of 40 μm initially. The time step in the simulation is $2.09 \times 10^{-11}$ second, thus about every 10 steps, we change the current, energy and radius of the injected beam. In addition, we inject 40 particles per mA each step and about 1.5 million for the whole simulation. Since we start the simulation from LC1, only S3, S4, and S5 are used to set up the focusing channel. In order to minimize the boundary effects on the simulation result at the end of the transportation line, we transport the beam 31 cm beyond the front plate of the second energy analyzer before it hits the boundary. Thus, in order to focus the beam in this short distance, we placed a solenoid identical to S5 in the simulation. This solenoid, S6, will not affect the simulation results because it is placed 12 cm away from the energy analyzer in LC2, which is a relatively large distance compared to its effective length shown in Table 3.1. The on-axis magnetic fields strengths in WARP are shown in Figure 5.3 along with the current profile, mean energy profile, and envelope profile measured at the starting point as functions of time. Furthermore, the number of cells in the x or y direction is 32; the number of cells in the z direction is 2048; the grid spacing in x or y direction is $6.25 \times 10^{-4}$ m; the grid spacing in z direction is $1.10 \times 10^{-3}$ m.
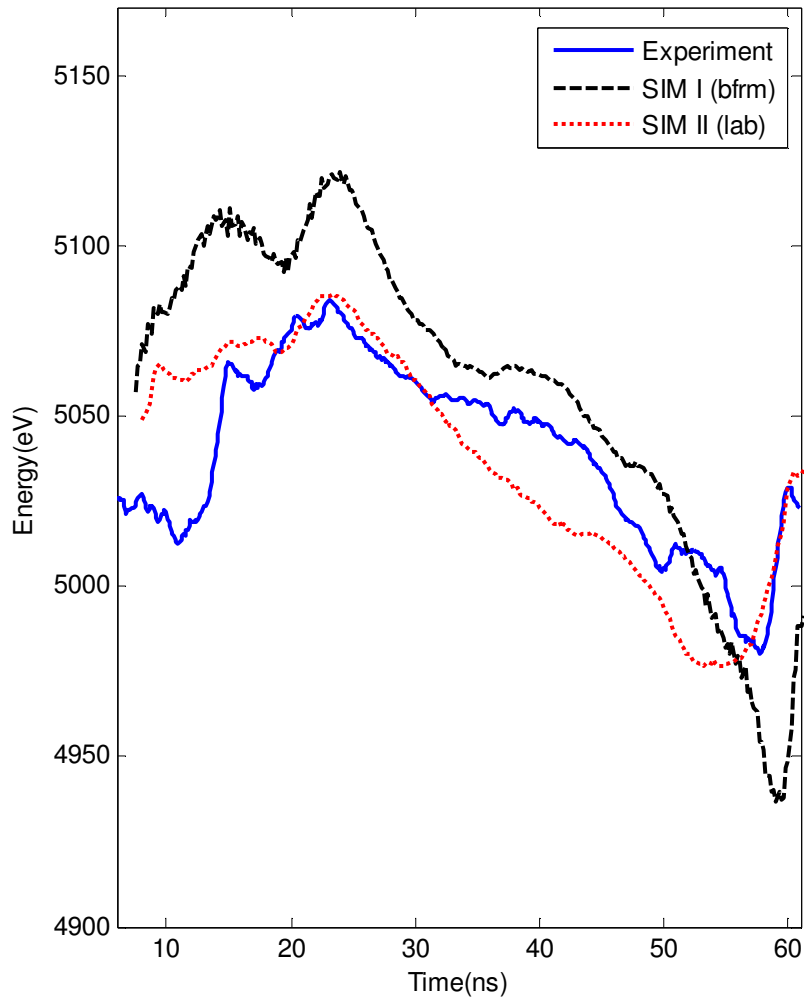
Figure 5.4: Comparison of WARP simulation results (beam frame: black dashed line; lab frame: red dotted line) and the experimental result (blue solid line) at LC2.
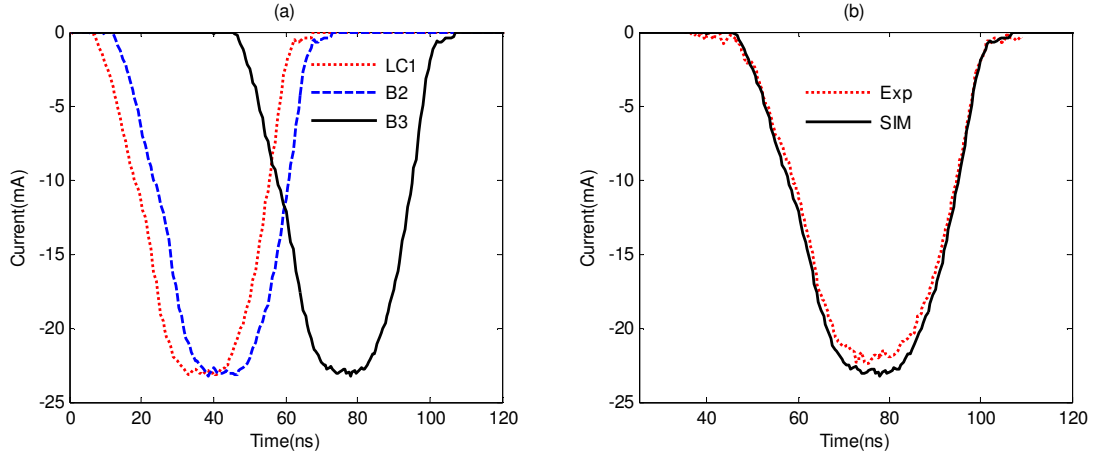
Figure 5.5: Current profiles of the parabolic beam obtained from WARP and experiment. (a): current profiles measured at LC1 (red dotted line), B2 (blue dashed line), and B3 (black solid line) in WARP, respectively; (b): comparison of current profiles measured by B3 obtained from WARP (black solid line) and experiment (red dotted line).

In Figure 5.4, we present mean energy profiles obtained from the experiment, and from WARP simulations in both the beam and lab frames. It clearly shows that using the simulation in the lab frame, we achieve much better agreement with the experimental measurement of the mean energy profile. However, some discrepancy still exists. For example, the measured energy profile at the beam center is not as linear as that predicted by the simulation. This suggests that the longitudinal electric fields calculated in the simulation are more linear than those acting on the beam in experiment. Since the longitudinal electric field $E_z$ is related to the derivative of line charge density, we should be able to find some clues in current profiles. Figure 5.5(a) indicates that the current profiles are almost identical at different locations from LC2 to B3 in the WARP simulation. The preservation of current profiles during the beam

transcript can lead to invariance of $E_z$. On the contrary, by comparing the current profiles at B3 obtained from the simulation and experiment in Figure 5.5(b), one can find some beam loss that occurred in experiment. As a result, the current profile has a different shape after the transport, especially the current modulation at the beam center. Also the longitudinal self electric field becomes more complicated due to the beam loss.
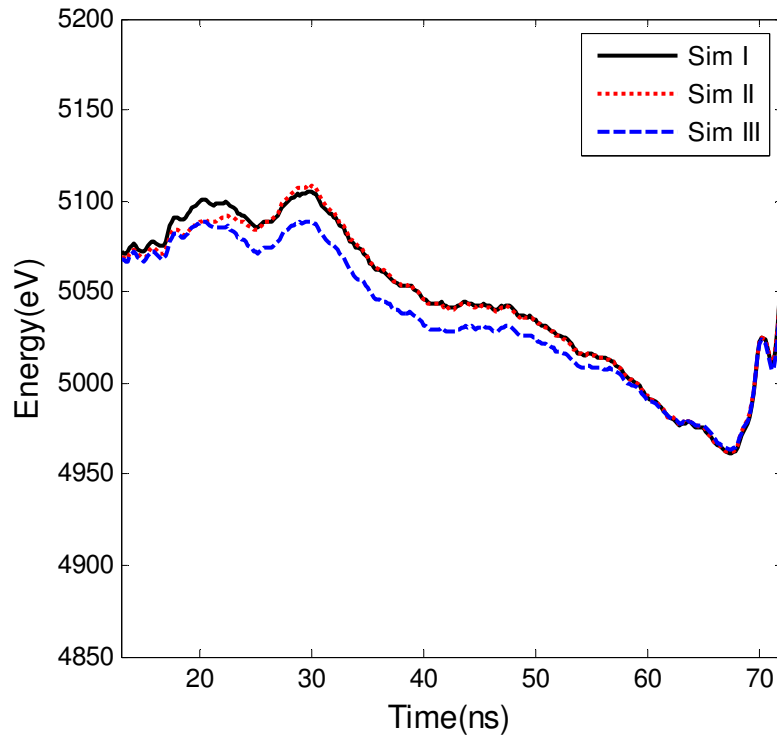


Figure 5.6: Simulations results of mean energy profiles in LC2 with different initial conditions for the parabolic beam. Sim I: inject measured current, envelope, and energy profiles (black solid line); Sim II: inject measured current, energy profiles and a constant beam radius of 5 mm (red dotted line); Sim III: inject measured current, envelope profiles and a constant beam energy of 5050 eV (blue dash line).

To study the sensitivity of the simulation results to different initial conditions, we performed two more simulations by changing the initial condition at injection. These include fixing the initial beam radius at 5 mm and injecting a beam with a constant energy of 5050 eV. We demonstrate all simulation results in Figure 5.6. The output energy profile does not change much when we inject a constant beam radius of 5 mm instead of the measured beam envelope profile, but it change significantly when we inject constant beam energy. When the initial energy is fixed at 5050 eV longitudinally, the peak value of the mean energy profile in LC2 is reduced by about 18 eV in WARP. On the other hand, the mean energy profile, measured at LC1 in experiment, has a peak value of about 5068 eV, as shown in Figure 4.24(a). These may indicate that the energy gain in longitudinal direction is not sensitive to the initial energy profile too. Furthermore, we also compare the current profiles measured at the location of B3 for different simulations. They are totally identical and consistent with the profile injected initially.

All the above observations can be explained by the following facts. In LC2, the ratio of the velocity modulation over the nominal velocity of the beam is less than 0.6%. It is still too small to affect the line charge density distribution and the longitudinal self electric field significantly. In addition, the beam pulse is more than 2.5 m long, leading to the slow variation of the line charge density. Thus the beam will not expand noticeably for a distance of 2.3 m.

## 5.2 Simulations of rectangular beams with perturbations

In this section, we apply the simulation technique using WARP in lab frame to the 25 mA and 40 mA perturbed rectangular beams, which have been discussed in chapter 4. As discussed in the previous section, the transport channel in WARP consists of 4 solenoids starting from LC1. The strengths of the solenoids are set according to those used in experiments. Since the perturbations for both beams are less than 10 ns wide and the longitudinal shapes of the unperturbed beams are rectangular, we inject only a part of the beam around the perturbation in order to improve the efficiency of computation. Longer beams of 60 ns have also been tested to ensure that the truncation does not affect the simulation results. As before, we compare the beam current profiles and mean energy profiles from simulations to experimental data and analytical results from 1-D calculation for both cases. We also present sensitivity studies to investigate effects of different initial conditions on the final results. Sec. 5.2.1 shows results for the 25 mA beam, and Sec. 5.2.2 shows those for the 40 mA beam.

### 5.2.1 Simulations of 25 mA beam

For the 25 mA perturbed beam, we inject part of the beam, 38 ns out of the full length of about 100 ns. The initial transverse beam size, longitudinal current and mean energy profiles are injected by importing the measured data shown in Figures 4.22(a), 4.20(a), and 4.25(a), respectively. We use the same numerical settings as those in the lab frame simulations of the parabolic beam. Figure 5.7 shows the initial transverse beam size, current and velocity profiles, and on-axis magnetic fields.

136
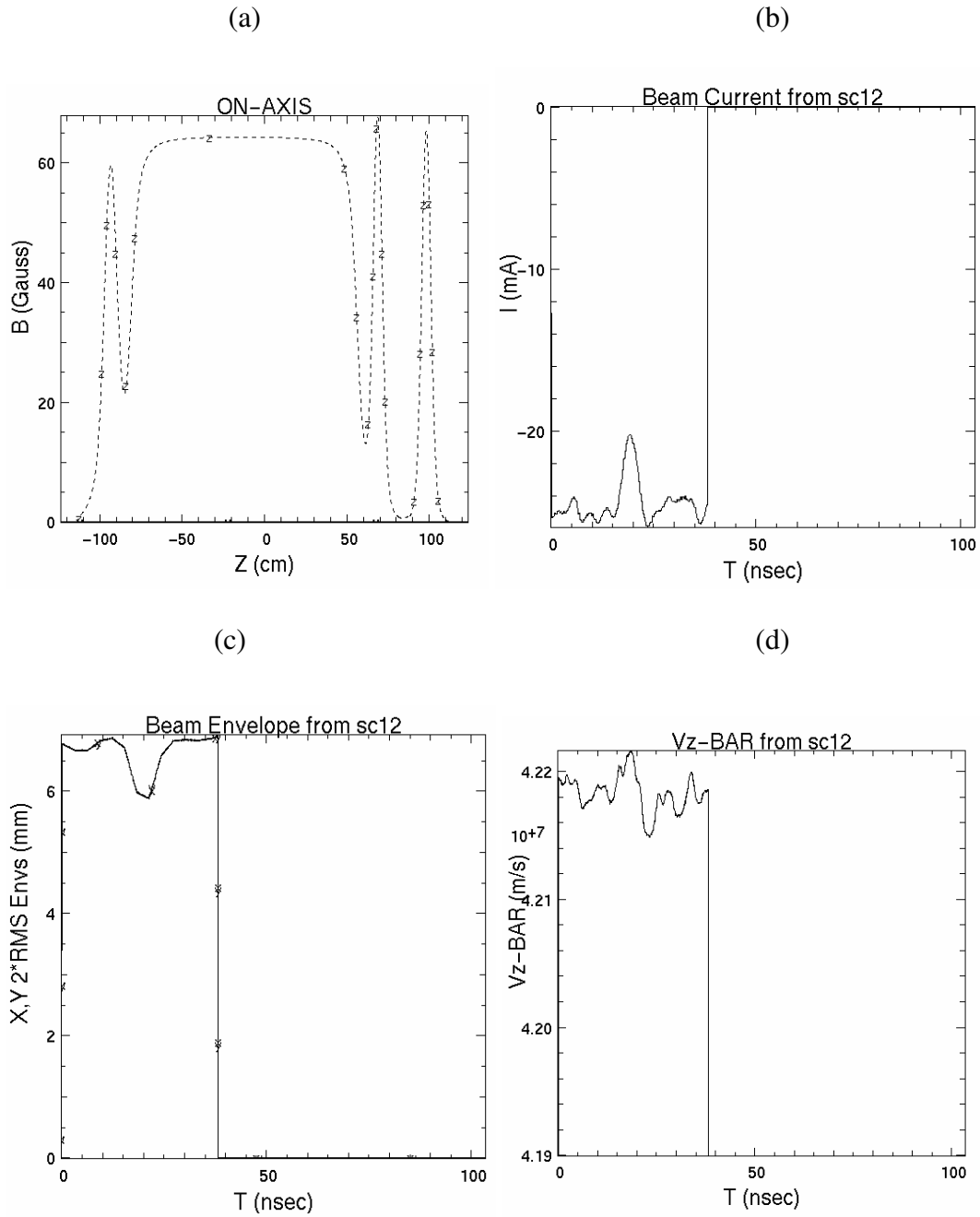
Figure 5.7: Initial conditions and solenoids settings for the 25 mA beam. (a): On-axis magnetic fields strengths of solenoids set up; (b) injected beam current; (c): the beam envelope; (d): the beam longitudinal mean velocity.
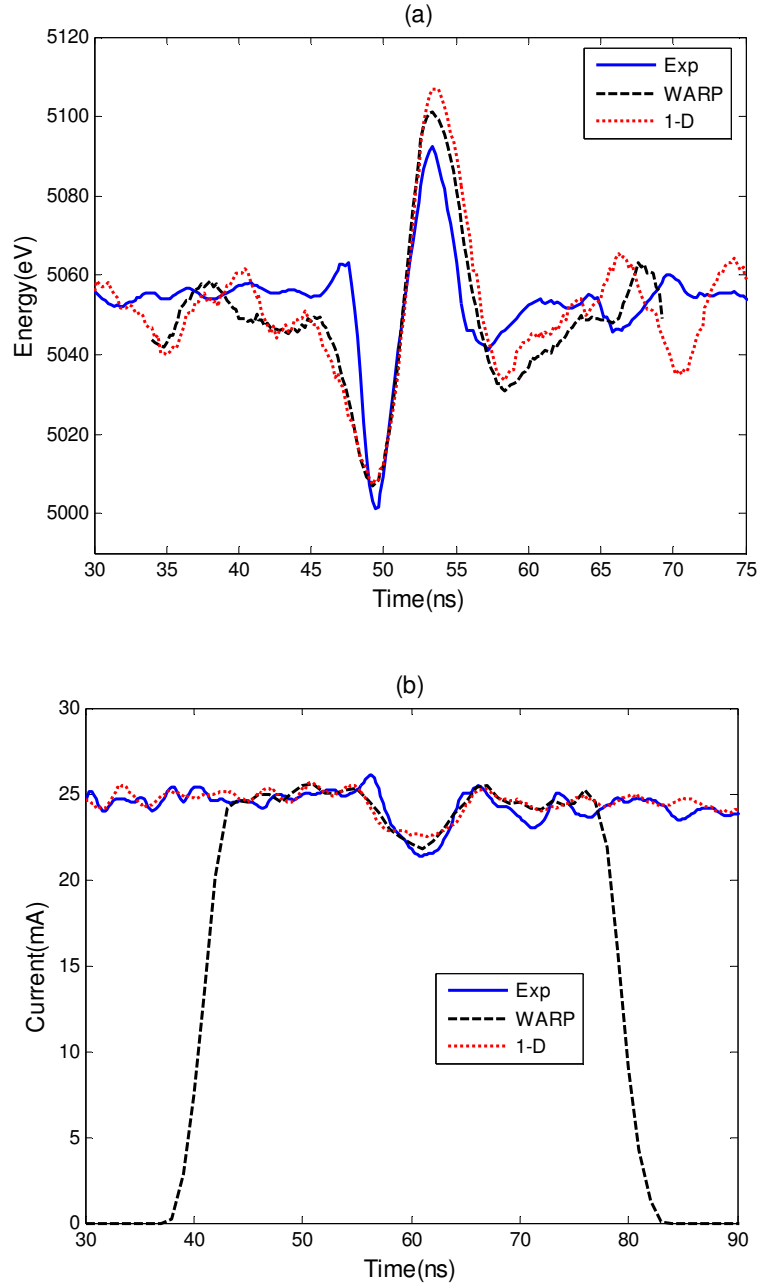
Figure 5.8: Comparison of results from the experiment (blue solid lines), WARP (black broken lines), and 1-D theory (red dotted lines) for the 25 mA beam. (a): mean energy profiles at LC2; (b) current profiles at B3. Current profiles have been flipped to show positive current values for the convenience of indicating negative perturbations.

In addition to the WARP simulation, we also try to predict the evolution of space-charge waves of this perturbed 25 mA beam using the 1-D theory. In the 1-D model, we assume the following beam parameters: a radius of 2.7 mm; a nominal beam energy of 5050 eV; an unperturbed main beam current of 25 mA; an initial current perturbation strength $\eta$ of 0.2; an initial energy perturbation of 10 eV. Hence, we can derive the sound speed $c_s = 1.87 \times 10^6 \, m/s$ and the $\alpha - factor$ $\alpha = -0.11$. In Figure 5.8, we present both mean energy profiles at LC2 and current profiles at B3 obtained from the experiment, WARP simulation, and 1-D cold fluid theory, respectively.

In energy profiles, the peak-to-peak amplitudes of the energy modulations are close for all cases, namely 90 eV, 94 eV, and 100 eV for the results from the experiment, WARP, and theory, respectively. The separation time between the two peaks of energy modulations are also consistent with the difference of the peak-to-peak amplitudes: the 1-D result has the largest separation and the experimental measurement shows the smallest. These suggest that in experiment the space-charge wave has a smaller sound speed than those predicted from both WARP and 1-D theory.

The current profile from the 1-D model exhibits the start of separation of fast and slow waves, but both results from WARP and experiment indicate a single negative peak in the current waveforms. Also, the amplitude of the experimental results is the largest among these three traces. As we have analyzed in Figure 3.17(a), when the two wave components are moving apart in the current profile, their sum will first exhibit a single peak with smaller amplitude and wider shape before developing

139

into two clear peaks. Thus, the comparison in Figure 5.8(b) leads to the same conclusion as that in Figure 5.8(a): the average sound speed $c_s$ in experiment is smaller than the theoretical prediction and numerical simulation. However, the result from the WARP simulation is closer to the experimental results than that from the 1-D model.
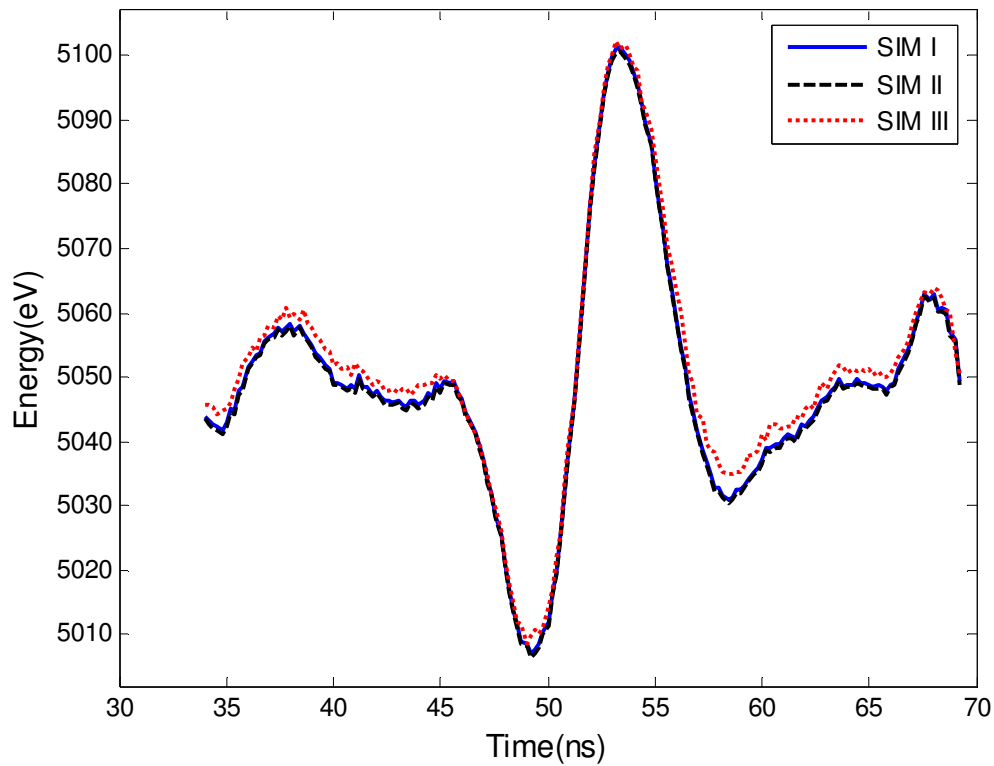


Figure 5.9: Simulation results of mean energy profiles in LC2 with different initial conditions for the 25mA beam. Sim I: inject measured current, envelope, and energy profiles (blue solid line); Sim II: inject measured current, envelope profiles and a constant beam energy of 5050 eV (black dash line); Sim III: inject measured current, energy profiles and a constant beam radius of 3.4 mm (red dotted line).

To test the sensitivity to initial conditions, we ran additional WARP simulations with different initial data. From the results shown in Figure 5.9, one can see that the longitudinal energy profiles are not affected by the variation of particle injection methods. As shown in Figure 4.25(a), the energy modulation in LC1 is relatively small, therefore there is almost no difference between the longitudinal energy profiles obtained from SIM I and SIM II. Furthermore, according to the 1-D theory, the g-factor depends on the average beam radius of the beam. On the other hand, the change of radius initially still produces a similar average beam radius to that of SIM I. Thus, we obtain similar results from SIM I and III. According to the above analysis, the physics in longitudinal space-charge waves governing the WARP simulations is still consistent with the 1-D cold fluid theory more or less. In other word, the longitudinal and transverse dynamics are still simply correlated through the g-factor. However, the WARP simulation is still a simplified model, a full 3-D simulation, which can include the details of the transverse distribution, may be required to study the longitudinal-transverse coupling.

## 5.2.2 Simulations of the 40 mA beam

We now turn to the 40 mA beam. In Figure 5.10, we illustrate the initial conditions and on-axis magnetic field distribution used in the WARP simulation. Here we only inject a beam 40 ns long instead of the whole pulse.
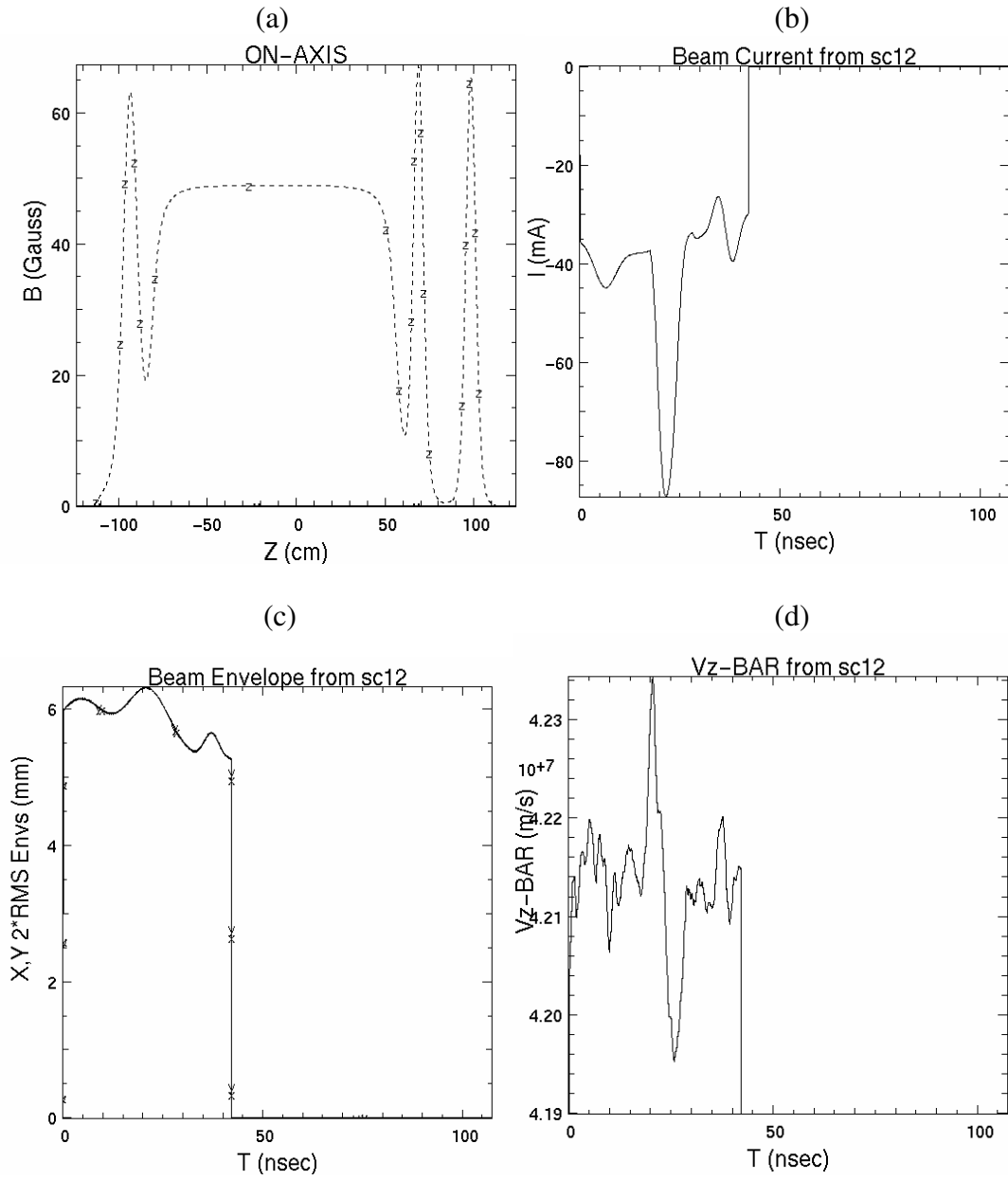
Figure 5.10: Initial conditions and solenoids settings for the 40 mA beam. (a): On-axis magnetic fields strengths of solenoids set up; (b) injected beam current; (c): beam envelope ; (d): longitudinal mean velocity.

In the 1-D model, the beam radius is 4.3 mm; the nominal beam energy is 5050 eV; the unperturbed main beam current is 40 mA; the initial current perturbation strength $\eta$ is 1.19; the initial energy perturbation is 10 eV. Hence, we can derive the sound speed $c_s = 2.07 \times 10^6 \, m/s$ and the $\alpha - factor$ $\alpha = 0.017$.

In Figure 5.11, as one may expect for the extremely nonlinear perturbation, very large discrepancies exist for the results from the experiment, WARP, and theory. As to the peak-to-peak amplitudes of energy modulations, the 1-D theory and WARP simulation predict a value of 630 eV and 541 eV, respectively, which are corresponding to 12.5% and 10.7% of the mean beam energy. However, in experiment, we obtain a much smaller energy modulation with the peak-to-peak amplitude of 309 eV. Also the shapes of the fast and slow waves are not preserved in the experiment. It seems like some mechanisms exists to damp the increase of energy modulation.

The comparison of current profiles shown in Figure 5.11(b) also exhibits much difference. The width of the current perturbation in experiment is close to that calculated from theory and simulation, but its height and shape are very different. These suggest that there is beam loss in the experiment. As we discussed earlier for the parabolic beam, this may be a reason for the discrepancy that observed in the energy profiles from the experiment, 1-D theory, and WARP simulation. To investigate the effect of the beam loss on the result of the longitudinal beam energy, we ran additional WARP simulations by applying virtual conducting tubes with different radii.
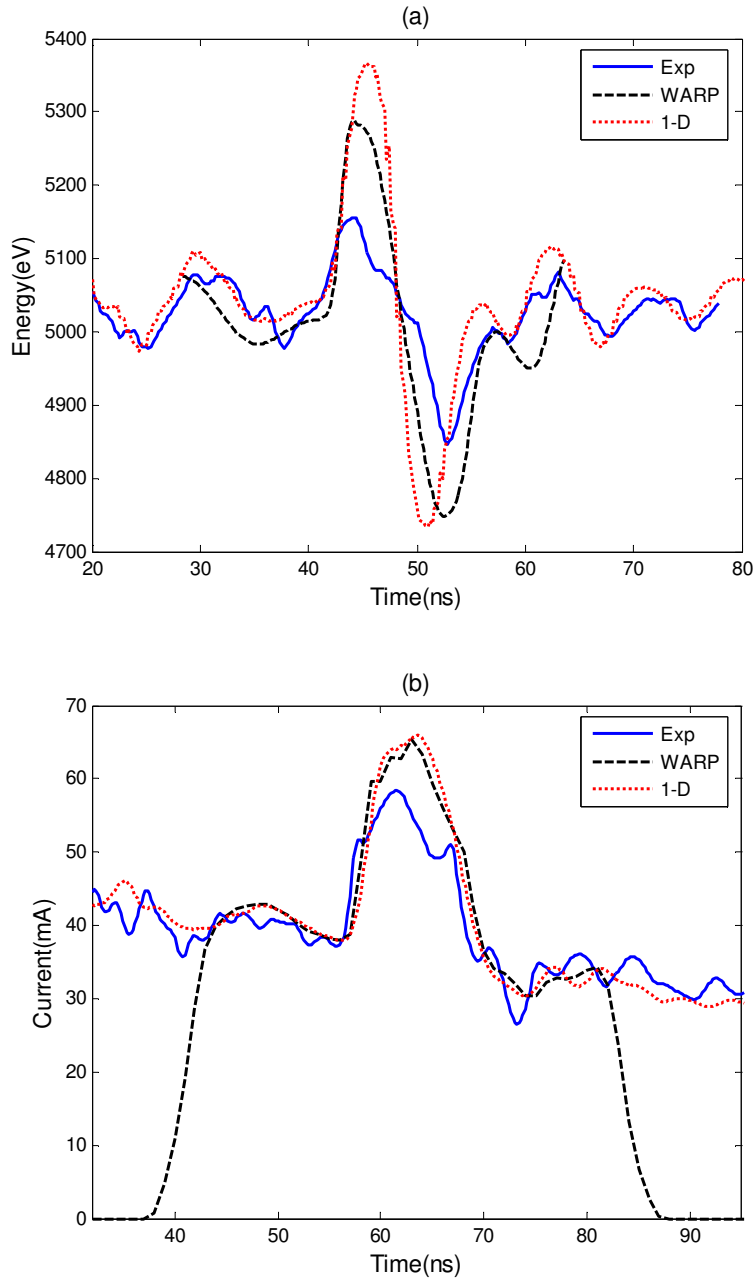
Figure 5.11: Comparison of results from the experiment (blue solid lines), WARP (black broken lines), and 1-D theory (red dotted lines) for the 40mA beam. (a): Mean energy profiles at LC2; (b) Current profiles at B3. Current profiles have been flipped to show positive current values for the convenience of indicating positive perturbations.
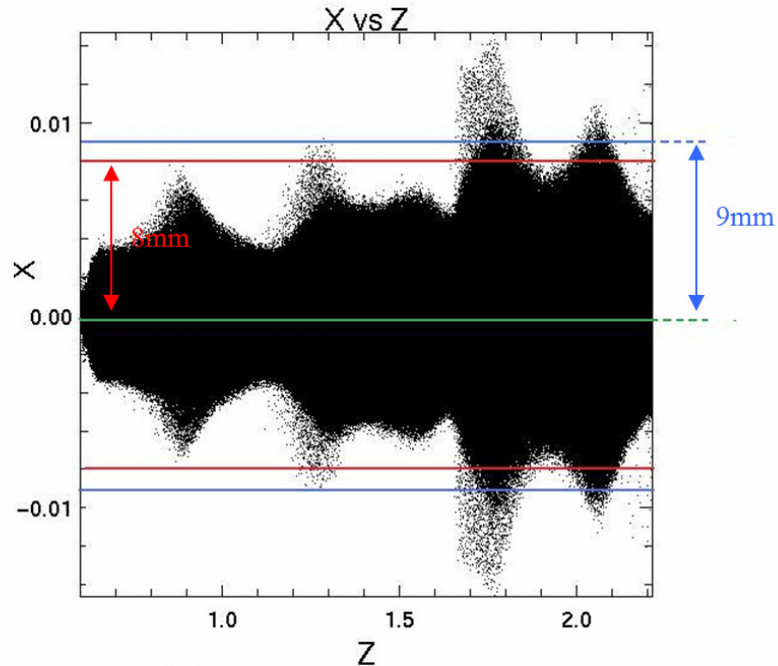
Figure 5.12: Illustration of applying two virtual conducting tubes in WARP code and the particle distribution in X-Z plane at t=57.2 ns. The units of both axes are meter. The perturbation is located from 1.22 m to 1.7 m.


In WARP, we are able to insert a virtual conducting tube concentric with the beam pipe. All particles that hit the wall of this tube will vanish. This tube is virtual in the sense that it does not affect the field solving during simulation. In other words, it is only used to catch particles wandering beyond a certain boundary, i.e. the wall radius. Figure 5.12 illustrates two different wall radii that were used in the simulation: 8 mm and 9 mm. As our simulation is in RZ geometry, the projection of the particle distribution in X-Z plane is equivalent to that in the R-Z plane. The simulation results of current and energy profiles are presented in Figure 5.13, where $r_w$ represents the radius of the virtual tube.
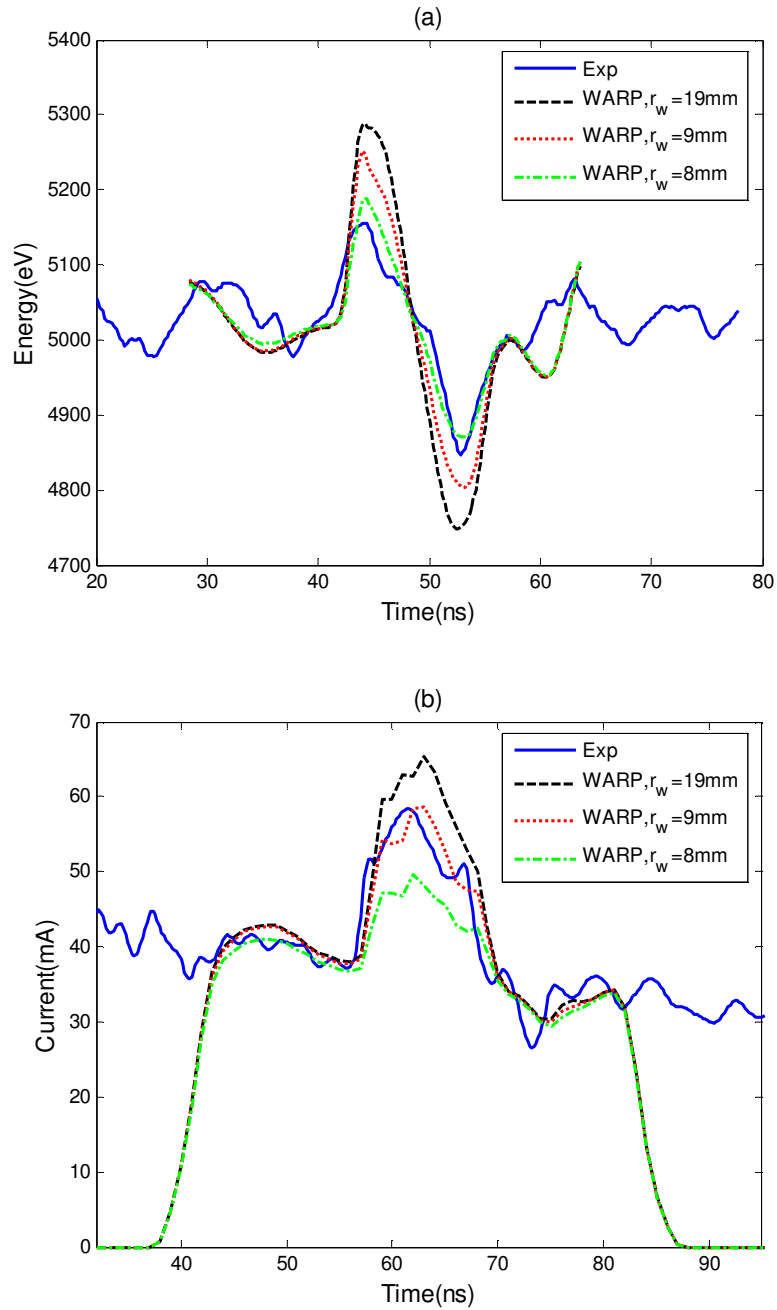
Figure 5.13: Comparison of results from the experiment (blue solid lines), WARP simulations with different radii of the virtual tube: 19 mm (black dashed lines), 9 mm (red dotted lines), and 8 mm (green dash dot lines). (a): Mean energy profiles at LC2; (b) Current profiles at B3. Current profiles have been flipped to show positive current values for the convenience of indicating positive perturbations.

146

When $r_w = 1.9$ cm, the virtual tube has the same radius as the beam pipe, thus the simulation result is the same as what we have presented earlier. The current profile becomes close to the experimental result when $r_w = 9$ mm. At the same time, although the energy profile in this case still has a significant larger modulation than the experimental result, it is much closer compared with the simulation without any beam loss. If the radius of the virtual tube is further cut down to 8 mm, we obtain a energy profile that is very similar to the experimental result. However, the current loss is more than the experiment in this case.

We believe that there are two possible reasons for why we cannot get the agreement with the current and energy profiles at the same time. First, in experiment, the beam loss may occur earlier than that in the simulation. Thus, for losing the same amount of particles, the longitudinal field is damped earlier in experiment. As a result, we obtain a smaller energy modulation from the experimental measurement. Second, in practical the beam loss may be caused by the mismatch or misalignment, which can offset the beam from the center of the pipe. As we discussed in chapter 2, the longitudinal self electric field is proportional to $g \dfrac{\partial \Lambda}{\partial z}$. When the beam is off center, the g-factor may become different and probably smaller because of the non-uniform field of image charges. To better understand the role of the g-factor here, more studies are required.

Finally, we also conducted the sensitivity study of this 40 mA beam. As shown in Figure 5.14, the WARP simulation results are not sensitive to the change of initial beam radius and energy. Due to the lack of a theoretical model for the evolution of nonlinear perturbations, it is difficult to judge if the beam loss is the only reason for the discrepancies shown in Figure 5.11(a). Other factors, such as the transient behavior of the energy analyzer and the longitudinal-transverse coupling, should also be investigated as future work.
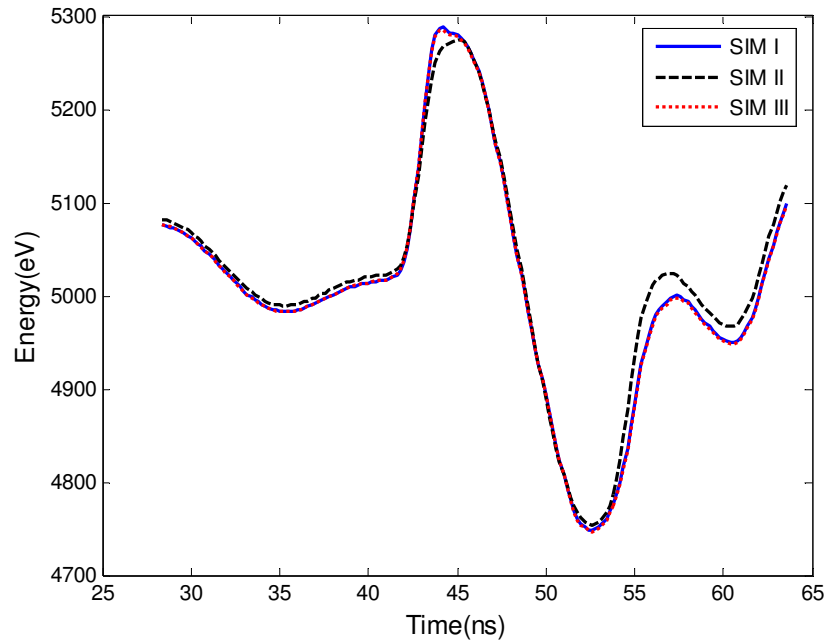


Figure 5.14: Simulations results of mean energy profiles at LC2 with different initial conditions for the 40mA beam. Sim I: inject measured current, envelope, and energy profiles (blue solid line); Sim II: inject measured current, envelope profiles and a constant beam energy of 5050 eV (black dash line); Sim III: inject measured current, energy profiles and a constant beam radius of 6 mm (red dotted line).

## 5.3 General remarks

In this chapter, we present a method to investigate the longitudinal space-charge waves using WARP simulations in lab frame. The parabolic beam is first used to benchmark the validity of this method. It shows that with the ability to set more details of the initial conditions in lab frame simulations, we can achieve better agreement with the experimental results than the beam frame simulations.

When this method is applied to the 25 mA perturbed beam, we still can get good agreement between simulation and those results from the experiment and 1-D theory. Thus, although the 20% negative perturbation in the beam cannot be treated as a small perturbation, it still evolves more or less according to the law defined by the 1-D linear theory. Yet, things become complicated when it comes to the 40 mA beam with an extremely large perturbation. We found that beam loss due to transverse mismatch or misalignment of the transport system could be a source of the discrepancy between experimental results and those from the simulation and 1-D theory. Further experiment in UMER, which has better alignment and a larger radius of beam pipe, will be useful to verify the studies here.

We did not observe any sign of transverse-longitudinal couplings from studies on sensitivity of output energy profiles to the initial conditions. This may be because of the short distance in our simulation or the inadequate simulation model. In all the beam frame simulations described above, we assume both the beam slope and emittance are constant. Using data provided from time-resolved tomography measurement, in future, one will be able to inject time dependent beam slope and

emittance. Furthermore, one can extend the model to a full 3-D simulation with complete measured 6-D phase space initially.

# Chapter 6  Conclusion

Section 6.1 summarizes new results which have been presented in this thesis, while section 6.2 addresses some unresolved issues and suggests some interesting topics for future studies.

## 6.1 Summary

As discussed in the introductory chapter, high resolution measurement of energy modulations, transverse-longitudinal correlations, and unexpected nonlinear phenomena occurring during the propagation of longitudinal space-charge waves have been major unsolved problems in study of the longitudinal dynamics of space-charge dominated beams. In this thesis, we have presented both experimental and numerical results to address these issues.

Using a high resolution energy analyzer installed in the LSE system, we have, for the first time, experimentally measured the detailed energy profiles of space-charge waves. The measured results show good agreement with both 1-D theoretical calculations and WARP simulations. However, there are discrepancies in the amplitudes of modulations for the nonlinear perturbations. To measure the evolution of space-charge waves in more detail, we upgraded the LSE system by inserting more diagnostics. The new system enabled us, for the first time, to obtain a complete set of experimental data for both current and energy profiles of the space-charge waves. By comparing the experimental results with analytical solutions from the theory, we have demonstrated that the 1-D cold fluid model is good for predicting general trends of the evolution of space-charge waves.  In addition, we also found that, in spite of its

small amplitude, the initial velocity modulation usually cannot be neglected for beams with small current perturbations.

Two different fast imaging tools, an OTR imager and a fast phosphor screen, have been developed to study the correlation between transverse and longitudinal dynamics. Using each of these two techniques, we imaged longitudinal slices of the beam as short as 3 ns. The experimental results provided us the first data of the transverse-longitudinal correlation. With the fast phosphor screen, we were able to take progressive 3-ns sliced images along the beam. By employing the tomography technique, we have constructed the time-resolved phase space with a resolution of 3 ns. Combining all this information with the longitudinal phase space measured by the energy analyzer, we have, for the first time, achieved the capability to map the time-resolved full 6-D phase space of a space-charge dominated beam.

We have demonstrated that the lab frame WARP simulation is a better model than the beam frame simulation. The results from the lab frame simulation show good agreement with experimental results for both the parabolic beam and the 25 mA rectangular beam with a 20% perturbation. For the beam with an extremely large perturbation, we observed a large discrepancy between the experimental results and those from the simulation and 1-D theory. Further simulation studies suggest that the beam loss due to mismatch or misalignment can contribute to inconsistent results between the experiment and simulation.

## 6.2 Suggestions for future work

As summarized above, even though we have substantially pushed the envelope in our understanding of the longitudinal space-charge waves, the new results presented here opened the door on many more unsolved problems. Based on the new findings and progress, we have the following suggestions for a continuation of this research:

First, much opportunity remains in the simulation of the nonlinear perturbation. For example, using the existing WARP lab frame simulation code, one can inject the beam slope and emittance profiles obtained from time-resolved tomography using a fast phosphor screen. Eventually, it is necessary to carry out a full 3-D beam frame simulation using the measured 6-D phase space distribution as initial conditions. They can help us simulate the mismatch of the nonlinear perturbation more accurately, and test sensitivity to misalignment. They may also provide some clues about the beam loss and its relationship with g-factor. Another interesting topic can be studied using simulation is the time resolution of the energy analyzer. Using a simulation technique developed for a gridded cathode electron gun, the energy analyzer can be studied in the same way [60]. With a better understanding of the transient behavior of the energy analyzer, we will be able to estimate the errors in measuring energy modulations more accurately.

Second, carrying out an experiment of nonlinear perturbation without any beam loss will be beneficial to completely understand the physics of the nonlinear perturbation. This experimental work can be done in LSE by using the movable phosphor screen to aid better alignment and matching. Furthermore, the 6-D phase

space distribution measured at LC1 can also be helpful to find the source of misalignment or mismatch. In addition, the experiment can also be done in UMER, which has better alignment and a bigger pipe radius.

Last but not least, it is important to measure the grid cathode pulse voltage with electron beam emission. As discussed earlier, the initial velocity modulation is generally not negligible for a small perturbation. The amplitude of the initial velocity perturbation depends on the grid-cathode pulse voltage. We have measured the signal of this pulse voltage without electron beam emission. However, when the beam is on, the input impedance between the grid and cathode will be different, hence, the real voltage that is applied between the grid-cathode gap may be different from what we measured before. One may be able to measure this voltage signal more accurately by connecting the grounding of an oscilloscope to the high voltage in the gun control circuit.

In summary, many new findings and results have been presented in thesis, however, more interesting and challenging work can be done in simulation studies and experimental work.

# Bibliography

[1] D. H. Dowell and P. G. O'Shea, Proceedings of the 1997 Particle Accelerator Conference, Vancouver, B.C. (IEEE, New York,1998), p.1891.

[2] A. Friedman, J. J. Barnard, D. P. Grote *et al.*, in Proceedings of the 2005 Particle Accelerator Conference, Knoxville, TN (IEEE, New York, 2005), p.339.

[3] R. F. Welton, M. P. Stockli, and S. N. Murray, Rev. Sci. Instrum. **75**, 1793 (2004).

[4] P. G. O'Shea and H. P. Freund, Science **292**, 1853 (2001).

[5] W. C. Hahn, Gen. Electr. Rev. **42**, 258 (1939).

[6] S. Ramo, Phys. Rev. **56**, 276 (1939).

[7] C. K. Birdsall and J. R. Whinnery, J. Appl. Phys. **24**, 314 (1953).

[8] A. H. W. Beck, Space-Charge Waves and Slow Electromagnetic Waves, Pergamon, New York (1958).

[9] A. W. Trivelpiece and R. W. Gould, J. of Appl. Phys. **30**, 1784 (1959).

[10] V. K. Neil and A. M. Sessler, Rev. Sci. Instrum. **36**,429 (1965).

[11] S. Humphries, Jr., J. Appl. Phys. **51**, 2338 (1980).

[12] J. Bisognano, I. Haber, L. Smith, and A. Sternlieb, IEEE Trans. NS-28(3) 2513 (1981).

[13] P. J. Channell, A. M. Sessler, and J. S. Wurtele, Appl. Phys. Lett. **39**,359 (1981).

[14] E.P. Lee, Proceedings of the 1981 Linac Conference, p.263, Santa Fe, NM (1981).

[15] I. Hofmann, Z. naturforsch. A **37**,939 (1982).

[16] D. A. Callahan, A. B. Langdon, A. Friedman, and I. Haber, J. Appl. Phys. **81**, 3398 (1997).

[17] D. H. Dowell, S. Joly, A. Loulergue, J. P. de Brion, and G. Haouat, Phys. Plasmas **4**, 3369 (1997).

[18] G. Stupakov and S. Heifets, Phys. Rev. ST Accel. Beams **5**, 054402 (2002).

[19] J. Neumann, D. Demske, R.B. Fiorito, P. G. O'Shea, G.L. Carr, H. Loos, B. Sheehy, and X. Wang, Proceedings of the 2003 IEEE Particle Accelerator Conference, Portland, OR, edited by J. Chew, P. Lucas and S. Webber, IEEE Cat. No. 03CH37423C, 1497 (2004).

[20] J. R. Harris, J. G. Neumann, K. Tian, and P. G. O'Shea, Phys. Rev. E **76**,026402 (2007).

[21] J. G. Wang, *et al.*, Phys. Rev. Lett. **71**, 1836 (1993).

[22] J.G.Wang, H.Suk, D.X. Wang, and M. Reiser, Phys. Rev. Lett. **72**, 2029 (1994).

[23] M. Reiser, *Theory and Design of Charged Particle Beams*, John Wiley & Sons, Inc, New York (1994).

[24] J. G. Wang, *et al.*, Phys. Rev. Lett. **74**, 3153 (1995).

[25] D. X. Wang, J. G. Wang, and M. Reiser, Phys. Rev. Lett. **73**, 66 (1994).

[26] H. Suk, Doctoral Dissertation, University of Maryland (1996).

[27] J. G. Wang, H. Suk, and M. Reiser, Phys. Rev. Lett. **79**, 1042 (1997)

[28] H. Suk, et al., J. Appl. Phys. **86**, 1699 (1999).

[29] Y. Zou, J. G. Wang, H. Suk, and M. Reiser, Phys. Rev. Lett. **84**, 5138 (2000)

[30] Y. Huo, Master Thesis, University of Maryland (2004).

[31] J. C. T. Thangaraj, *et al.*, Proceedings of the 2007 IEEE Particle Accelerator Conference, Albuquerque, NM, ed. C. Petit-Jean-Genaz, IEEE Cat. No. 07CH37866, 3570 (2007).

[32] K. Tian, Y. Zou, Y. Cui, I. Haber, R. A. Kishek, M. Reiser, and P. G. O'Shea, **9**, 014201 (2006).

[33] K. Tian, R. A. Kishek, P. G. O'Shea, R. B. Fiorito, D. W. Feldman, and M. Reiser, Phys. Plasmas **15**, 056707(2008).

[34] D. P. Grote, A. Friedman, I. Haber, S. Yu, Fusion Eng. Des **32-33**, 193 (1996).

[35] J. R. Harris, Doctoral Dissertation, University of Maryland (2005).

[36] Y. Zou, Y. Cui, M. Reiser, and P. G. O'Shea, Phys. Rev. Lett. **94**, 134801 (2005).

[37] Y. Cui, Doctoral Dissertation, University of Maryland (2004).

[38] K. Tian, Y. Cui, I. Haber, Y. Huo, *et al.*, Proceedings of the 2005 IEEE Particle Accelerator Conference, Knoxville, TN, ed. C. Horak, IEEE Cat. No. 05CH37623C, 3712 (2005).

[39] J. G. Wang *et al.*, IEEE Transactions on Electron Devices. **37**, 2622 (1990).

[40] Y. Cui, Y. Zou, A. Valfells, M. Reiser, I. Haber, R. A. Kishek, S. Bernal, and P. G. O'Shea, Rev. Sci. Instrm. **75**, 2736 (2004).

[41] Y. Zou, Y. Cui, I. Haber, M. Reiser, and P. G. O'Shea, Phys. Rev. ST Accel. Beams **6**, 112801 (2003).

[42] Y. Cui, Y. Zou, M. Reiser, R. A. Kishek, I. Haber, S. Bernal, and P. G. O'Shea, Nucl. Instrum. Methods Phys. Res. A, **544**, 527 (2004)

[43] B. L. Beaudoin, S. Bernal, I. Haber, R. A. Kishek, P. G. O'Shea, M. Reiser, J. C. T. Thangaraj, K. Tian, M. Walter, and C. Wu, Proceedings of the 2007 IEEE Particle Accelerator Conference, Albuquerque, NM, ed. C. Petit-Jean-Genaz, IEEE Cat. No. 07CH37866, 2322 (2007).

[44] J. R. Harris, J. G. Neumann, and P. G. O'Shea, J. Appl. Phys. **99**, 093306 (2006).

[45] J. R. Harris and P. G. O'Shea, IEEE Transactions on Electron Devices. **53**, 2824 (2006).

[46] P. G. O'Shea, M. Reiser, R. A. Kishek *et al.*, Nucl. Instrum. Methods Phys. Res. A **464**, 646 (2001).

[47] J. D. Jackson, *Classical Electrodynamics*, Hoboken, NJ, John Wiley & Sons Inc., (1999).

[48] I. M. Frank and V. L. Ginsburg, J. Phys. **9**, 353 (1945).

[49] P. Goldsmith and J. Jelley, Phil. Mag. **3**, 836 (1959).

[50] L. Wartski, Doctoral Thesis, Universite de Paris-Sud, Centre d'Orseay (1976).

[51] D. W. Rule and R. B. Fiorito, "The use of Transition Radiation as a Diagnostic for Intense Beams", Naval Surface Warfare Center TR84-134 (1984).

[52] C. A. Brau, *Modern Problems in Classical Electrodynamics*, New York, NY, Oxford University Press (2004).

[53] R. B. Fiorito, *et al.*, Physical Review Special Topics-Accelerators and Beams, **9**, 052802 (2006).

[54] R. B. Fiorito, B. L. Beaudoin, S. Casey, D. Feldman, P. G. O'Shea, and B. Quinn, in proceedings of the 2007 Particle Accelerator Conference, Albuquerque, NM, (IEEE, New York, 2007) p.4006.

[55] R. B. Fiorito and D.W. Rule, AIP Conf. Proc. **319**, 21 (1994).

[56] D. Stratakis, K. Tian, R.A. Kishek, I. Haber, M. Reiser, and P.G. O'Shea, Phys. of Plasmas **14**, 120703 (2007).

[57] H. Li, Doctoral Dissertation, University of Maryland, (2004).

[58] D. Stratakis, R. A. Kishek, H. Li, S. Bernal, M. Walter, B. Quinn, M. Reiser, and

P.G. O'Shea, **9**, 112801 (2006).

[59] D. Stratakis *et al.*, to be published, 2008

[60] I. Haber, private communication, 2008